

Microfluidic Energy Conversion Devices

THÈSE N° 7709 (2017)

PRÉSENTÉE LE 30 JUIN 2017

À LA FACULTÉ DES SCIENCES ET TECHNIQUES DE L'INGÉNIEUR

LABORATOIRE D'OPTIQUE

PROGRAMME DOCTORAL EN PHOTONIQUE

ÉCOLE POLYTECHNIQUE FÉDÉRALE DE LAUSANNE

POUR L'OBTENTION DU GRADE DE DOCTEUR ÈS SCIENCES

PAR

Seyyed Mohammad HOSSEINI HASHEMI

acceptée sur proposition du jury:

Prof. C. Moser, président du jury

Prof. D. Psaltis, directeur de thèse

Dr A. Delfino, rapporteur

Dr M. Despont, rapporteur

Prof. M. Paolone, rapporteur



ÉCOLE POLYTECHNIQUE
FÉDÉRALE DE LAUSANNE

Suisse
2017

Acknowledgements

During my PhD studies, I was privileged to work on the topics and ideas that most intrigued me, which was only possible because of the supportive and encouraging attitude of my thesis advisor, Professor Demetri Psaltis. I would like to thank him for accepting me as a group member and showing me how to approach a research topic and to move forward step by step. His patience and openness during these years was always heart-warming.

I was very fortunate to work with two brilliant scientists in the lab: Miguel Modestino and Jae-Woo Choi. Miguel's depth and breadth of knowledge in chemical engineering were a blessing for me. I not only learned how to do research with him, but also how to maintain motivation and momentum. His presence in various aspects of my PhD studies such as presentation coaching, editing the papers and documents, providing his perspective on the results, and training on the instruments was a great help. Jae-Woo's presence as a smart and dedicated scientist made it possible to overcome many difficulties at the beginning of my journey. I would also like to thank Carole Berthet, our lab's administrative assistant, for her caring personality and help with the accommodation when I first arrived in Lausanne.

Professor Chris Moser from LAPD and Sophia Haussener from LRESE and their team were kind enough to let me use some of their instruments and lab space. As the head of SHINE project, Chris was always a source of inspiration and generously offered his help on many occasions as, for instance, accepting to act as the jury president of my defense session. Special thanks also go to Professor Mario Paolone, Dr. Antonio Delfino, and Dr. Michel Despont for taking time to read this dissertation and act as the jury members. Former and present members of LO, LAPD, and SHINE project were all part of my life at EPFL and I grew a strong bond of friendship with them. The francophone members – G. Laporte, T. Lanvin, A. Goy, J. Cuennet, L. Descloux, S. Walpen, and A. Burnand – were very patient with my time to time requests for help with French. I appreciate D. Conkey's help with editing some of my English writing. Other people, including N. Stasio, M. Hasani, P. Hadikhani, Y. Pu, M. Romito, I. Papadopoulos, E. Kakkava, W. Song, M. Zielinsky, J. Lim, G. Panusa, X. Yang, F. Albertin, J. Staley, E. Chinello, C. Rodriguez, S. Temburne, M. Dumortier, V. Zagolla, D. Domine, J. Bailat, J. Schuettauf, accompanied me during this journey together with all of my other friends both inside and outside of EPFL.

Last but not least, my family members – my parents, my brother, and my beloved wife Asiyeh – definitely played an enormous role and my gratitude towards them cannot be framed in words.

SMHH

Lausanne, February 2017

Abstract

Renewable resources of energy are increasing their share in our energy portfolio thanks to the technological advancements and an increasing environmental awareness in society. Although the cost of power generation from these resources has been reduced to reasonable amounts during the past few years, the lack of economical and deployable storage mechanisms hinders their transformation into the dominant supplier of energy in the world. Storing the energy from renewables in the chemical bonds of a convenient fuel with high power density and a carbon neutral cycle of regeneration is an appealing answer to this challenge. Thanks to its unique properties, hydrogen is the main chemical of interest for this purpose.

This dissertation is a collection of several efforts in making this process more practical by providing several microreactors with novel functionalities. The potentials of microfluidics in the field of electrochemical energy conversion is first investigated and based on the obtained intuition, a membrane-less electrolyzer and fuel cell based on two-phase flows and a vapor fed hydrogen generator have been developed. Furthermore, a microfluidic chip which uses solar thermal energy for sample concentration is introduced. This chip can be coupled with the vapor-fed H_2 generator or membrane-less electrolyzer to provide them with the water produced from brine or contaminated sources. In a similar effort, a photothermal reactor is developed for water treatment whose output can be used to feed the membrane-less electrolyzer. The novel functionalities and advantages of each device are discussed and finally, new research lines are suggested for further development of a new class of Multiphase Flow Electrochemical Reactors (MFERs) in which the physics of multiphase flows will be employed to boost the performance while providing cost reduction in the final device.

Keywords

Microfluidics, Electrochemical reactor, Multiphase flow, Microreactor, Hydrogen energy, Renewable energy, Solar energy, Water treatment, Electrolysis, Fuel cell, Ion conductive membrane, Membrane-less.

Résumé

Les sources d'énergie renouvelables prennent une part croissante dans notre portfolio énergétique grâce au progrès technologique et à l'éveil d'une conscience environnementale dans la société. Bien que le coût de production de l'énergie à partir de ces sources ait été réduit à des montants raisonnables durant ces dernières années, le manque de moyens de stockage et de déploiement empêche les énergies renouvelables de devenir des sources dominantes dans le monde. Le stockage des énergies renouvelables sous forme de liaisons chimiques d'un combustible d'emploi commode, à haute densité énergétique et ayant un cycle carbone neutre, est une réponse séduisante au défi énergétique. En raison de ses propriétés uniques, l'hydrogène est l'élément chimique de choix pour cette application.

Cette thèse est l'aboutissement d'une série d'efforts dédiés à rendre ce procédé de conversion électrochimique plus pratique en développant plusieurs microréacteurs munis de nouvelles fonctionnalités. Le potentiel de la microfluidique dans le domaine de la conversion électrochimique d'énergie est d'abord étudié. En se basant sur l'intuition on a développé un électrolyseur sans membrane, une pile à combustible utilisant un flux à deux phases, et un générateur d'hydrogène alimenté à la vapeur. De plus, on a introduit une puce microfluidique utilisant l'énergie thermique solaire pour la concentration d'espèces biologiques et/ou chimiques en milieu aqueux. Cette puce peut être couplée avec le générateur d'hydrogène alimenté à la vapeur ou avec l'électrolyseur sans membrane afin d'alimenter ces derniers avec de l'eau potentiellement salée. Dans la même ligne d'idée, on a développé un réacteur photo-thermique pour le traitement des eaux dont la sortie peut être utilisée pour alimenter l'électrolyseur sans membrane. Les fonctionnalités nouvelles et les avantages de chacun de ces dispositifs sont discutés. Finalement, de nouvelles lignes de recherche sont suggérées pour le développement futur d'une nouvelle classe de Réacteurs Électrochimiques à Flux Multiphasés (REFM) dans lesquels la physique des flux multiphasés est employée pour améliorer les performances du dispositif tout en réduisant son coût.

Mots-clés

Microfluidique, Réacteur électrochimique, Flux multiphasé, Microréacteur, Énergie à l'hydrogène, Énergie renouvelable, Énergie solaire, Traitement de l'eau, Électrolyse, Pile à combustible, Membrane conductrice d'ions, Sans membrane.

Contents

ACKNOWLEDGEMENTS.....	III
ABSTRACT.....	V
RÉSUMÉ	VII
CHAPTER 1 INTRODUCTION	1
1.1 <i>STRUCTURE</i>	2
1.2 <i>CONTRIBUTIONS</i>	4
<i>BIBLIOGRAPHY</i>	5
CHAPTER 2 THE POTENTIAL FOR MICROFLUIDICS IN ELECTROCHEMICAL ENERGY SYSTEMS.....	7
2.1 <i>INTRODUCTION</i>	8
2.2 <i>WHY MICROSYSTEMS FOR ELECTROCHEMICAL ENERGY CONVERSION?</i>	9
2.3 <i>STATE-OF-THE-ART ELECTROCHEMICAL ENERGY CONVERSION MICROSYSTEMS ..</i>	12
2.4 <i>SCALABILITY AND MANUFACTURABILITY OF ENERGY MICROSYSTEMS</i>	18
2.5 <i>CONCLUSIONS AND PERSPECTIVE</i>	21
<i>BIBLIOGRAPHY</i>	23
CHAPTER 3 MASS TRANSPORT ASPECTS OF WATER ELECTROLYSIS.....	27
3.1 <i>INTRODUCTION</i>	28
3.2 <i>PROCESSES IN THE BOUNDARY LAYER</i>	28
3.3 <i>PROCESSES IN BULK LIQUID ELECTROLYTES</i>	36
3.4 <i>PROCESSES IN SOLID ELECTROLYTE MEMBRANES</i>	38
3.5 <i>CONCLUSIONS AND PERSPECTIVES</i>	40
<i>BIBLIOGRAPHY</i>	42
CHAPTER 4 A MICROPILLAR ARRAY FOR SAMPLE CONCENTRATION VIA IN-PLANE EVAPORATION.....	45

4.1	INTRODUCTION.....	46
4.2	DESIGN OPTIMIZATION	48
4.3	EXPERIMENTAL RESULTS.....	53
4.4	DISCUSSION	55
4.5	CONCLUSION	56
	BIBLIOGRAPHY.....	57
CHAPTER 5 SOLAR THERMAL HARVESTING FOR ENHANCED PHOTOCATALYTIC REACTIONS		61
5.1	INTRODUCTION.....	62
5.2	MOTIVATION	64
5.3	DEVICE FABRICATION.....	65
5.4	RESULTS AND DISCUSSION	67
5.5	CONCLUSION	70
	BIBLIOGRAPHY.....	71
CHAPTER 6 VAPOR-FED MICROFLUIDIC HYDROGEN GENERATOR.....		73
6.1	INTRODUCTION.....	74
6.2	METHODOLOGY	75
6.2.1	Device design.....	75
6.2.2	Model development.....	76
6.2.3	Device Fabrication.....	78
6.2.4	Electrochemical Characterization	81
6.2.5	Gas Composition Characterization	81
6.3	RESULTS AND DISCUSSION	81
6.3.1	Interplay between transport and electrochemical processes	81
6.3.2	Transient device behaviour.....	85
6.3.3	Gas transport across channels	87
6.3.4	Improving the reaction kinetics at the electrodes	90
6.4	CONCLUSIONS.....	91
	BIBLIOGRAPHY.....	93
CHAPTER 7 MEMBRANE-LESS ELECTROLYZER FOR HYDROGEN PRODUCTION ACROSS THE PH SCALE		97
7.1	INTRODUCTION.....	98
7.2	DEVICE FABRICATION	101
7.3	EXPERIMENTAL SETUP AND MEASUREMENTS.....	102
7.4	RESULTS AND DISCUSSIONS	103
7.5	CALCULATIONS.....	107
7.6	CONCLUSIONS.....	109

<i>BIBLIOGRAPHY</i>	110
CHAPTER 8 MEMBRANE-LESS MICRO FUEL CELL BASED ON TWO-PHASE FLOW	113
8.1 <i>INTRODUCTION</i>	114
8.2 <i>WORKING PRINCIPLE</i>	115
8.3 <i>ANALYTICAL AND NUMERICAL MODEL</i>	115
8.4 <i>EXPERIMENTAL SECTION</i>	118
8.4.1 <i>Device architecture and fabrication</i>	118
8.4.2 <i>Experimental set-up and characterization</i>	120
8.5 <i>RESULTS AND DISCUSSION</i>	121
8.6 <i>CONCLUSION</i>	125
<i>BIBLIOGRAPHY</i>	126
CHAPTER 9 CONCLUSION AND OUTLOOK	129
9.1 <i>INTRODUCTION</i>	130
9.2 <i>MULTIPHASE FLOW ELECTROCHEMICAL REACTORS (MFERS):</i>	130
9.3 <i>ALTERNATIVE ELECTROCHEMICAL REACTIONS</i>	135
9.3.1 <i>Chloralkali process</i>	135
9.3.2 <i>Carbon dioxide reduction</i>	136
9.4 <i>THROUGHPUT ENHANCEMENT</i>	136
<i>BIBLIOGRAPHY</i>	137
CURRICULUM VITAE	139

Chapter 1

Introduction

The design, implementation, and characterization of microfluidic reactors, mainly for electrochemical reactions, is presented in this dissertation. This chapter provides an overall view of the dissertation structure by briefly discussing the contents of each chapter and its relation to other chapters briefly. The second chapter is dedicated to identify the role and potentials of microfluidics in electrochemical reactors engineering, followed by a chapter with a concise summary of the transport phenomena involved in these reactors. The aim of the latter chapter is to provide intuition on the interplay of the important transport phenomena and their impact on the performance of the device. Chapters four through eight elaborate on four different microreactors and one microfluidic chip that could be used in conjunction with two of the discussed microreactors, providing them with the pure reactants. The final chapter discusses the main conclusions and outlook.

1.1 Structure

Electrochemical conversion and storage is the solution to provide constant energy despite the fluctuations of power provided by renewable resources. Some electrochemical devices such as batteries and supercapacitors are technologically mature and already in use for this purpose. The issue with widespread adoption of such devices is two-fold. First, they cannot address the problem for long periods of time. Batteries are a suitable solution for day to day variations in solar energy, but they cannot regulate the flow of energy on a seasonal basis. This is specifically critical for geographical settings with substantial difference of the solar flux in winter and summer. Second, the power density of these devices is not high enough to enable their large scale implementation around the world. This implies not only an increase in space demand for their manufacturing and installation, but potentially a lot of pressure on the supply chain of their constituent raw materials, such as lithium.

For long term storage of renewable energy, generation of high power density chemical fuels such as hydrogen is envisioned. This fuel can be stored and used at the point and time of demand. To make this method deployable at large scale, a reduction of the hydrogen's final cost is necessary. This can be achieved through design simplification and performance improvement of the electrochemical reactors for generation and consumption of hydrogen as a solar fuel, i.e. electrolyzers and fuel cells, which are the main topics of this dissertation. The main focus, presented herein, is to remove the ion conductive membrane from these devices and replace it by liquid flowing electrolytes. The challenges arising from this change are also discussed and addressed. Although the membrane-less electrochemical reactors working with single phase flows are not new^{1, 2}, the main contribution of this dissertation is to introduce multiphase flows into the simplified design of these devices.

This **first chapter** provides an overview of the following chapters, their relationship, and their contribution to the fulfillment of the dissertation's overall goal.

An investigation of the potential of microfluidics in electrochemical conversion systems is contained in **Chapter 2**. Microfluidics is a powerful tool that provides precise control over the flows inside microchannels. For instance, due to the laminar nature of microflows, manipulation of contained entities such as bubbles is achievable. These bubbles can be seen as carriers of the products or reactants in a chemical reaction. Furthermore, small and tunable ionic pathlengths in a microfluidic device is beneficial for alleviation of ionic transport losses. Finally, flow plates of some state of the art fuel conversion devices such as fuel cells,

already contain sub-millimeter channels, mainly to minimize the losses due to mass transport to and from the reaction sites.

Chapter 3 contains a short review of the transport phenomena in electrochemical reactors, considering water splitting as a relevant model reaction. The sources of losses are discussed in order to provide guidelines for the optimal design of microreactors presented in the later chapters.

Chapter 4 elaborates on the fabrication and performance of a solar powered microfluidic chip for sample concentration. The sample can be a biological liquid or brine. In the case of the brine, the device functions as a solar desalinators where the output deionized vapor or liquid water can be used as the feedstock for the vapor fed electrolyzer discussed in **Chapter 6** or the membrane-less hydrogen generator of **Chapter 7**.

Chapter 5 presents a photothermal reactor for water treatment that utilizes the non-UV part of sunlight to heat up the reaction chamber and the UV part to drive the photocatalytic decomposition of organic pollutants in water. This synergy boosts the reaction rate considerably. The same concept can be applied to solar fuel production. Water can be heated up using the portion of sunlight that is thermalized by the photoabsorber and, thus the overall efficiency of solar to hydrogen energy conversion increases. This process additionally improves the performance of the solar cell by cooling it down.

Chapter 6 discusses the design, modelling, and implementation of a vapor fed microelectrolyzer. This device takes in the humid ambient air and splits the water molecules into hydrogen and oxygen. Development of such devices is important for settings where liquid fresh water is scarce. In areas in which salty water is abundant, this device can be coupled with the microfluidic chip of **Chapter 4** to receive water vapor for proper functioning. Nevertheless, electrolysis of water in gaseous form is interesting since thermodynamically, splitting water vapor is less demanding than liquid water.

Chapter 7 explains how the fluidic forces in a microfluidic channel can be employed to separate the products of the water splitting reaction. Since the evolved gaseous bubbles do not mix, the need for integration of a solid membrane or separator is removed. Such a solid component has been replaced by liquid electrolytes with tunable pH values and higher ionic conductivities than their solid counterparts. These advantages facilitate the integration of a broader range of catalytic material and a potential efficiency gain due to lower ohmic losses. Furthermore, such a device can be realized at much lower fabrication and running cost, weight, and size due to the lack of an ion conductive membrane.

Chapter 8 is dedicated to a membrane-less microfluidic fuel cell that works based on two-phase flow principles. In principle, this fuel cell complements the electrolyzer of **Chapter 7** in the sense that it provides a platform for the reverse reaction to take place, i.e. going from chemical fuel to electricity. The novelty in this fuel cell lies in the fact that the oxidant and fuels flow over the surface of electrodes in gaseous forms without coalescing. This has been achieved by devising engineered topographies in the cell that define the surface forces and guide the bubbles in desired paths. This feature relaxes the mass transport limitations encountered in the single phase microfluidic fuel cells.

Chapter 9 is the conclusion of the results of the dissertation. Potential research and development threads are discussed for the future studies. Some of these threads are being pursued by the Optics Lab and promising initial results are presented.

1.2 Contributions

Some colleagues and collaborators must be credited for their contributions in different studies presented here. The roles of these people are discussed below:

Chapter 2 originates from a perspective paper³ led by our group's former post doc Miguel Modestino, and coauthored with University of Twente's David Fernandez Rivas and Han Gardeniers.

Chapter 3 reflects part of the review paper⁴ coauthored by Miguel Modestino and Sophia Haussener at EPFL.

Chapter 4 summarizes results of the first project⁵ I worked on as a PhD student. This project was led by Jae-Woo Choi, a former post doc of our lab.

Chapter 5 reports on a second project⁶ accomplished with the help of Jae-Woo Choi.

Chapter 6 is a study conducted⁷ by Miguel Modestino in collaboration with Mikael Dumortier, a former post doc at LRESE.

Chapter 7 is fulfilled⁸ with the help of Miguel Modestino.

Chapter 8 elaborates on a device⁹ that the EPFL's master student, Matthias Neuenschwander, partially worked on during a semester project. The study was finalized with the help of Pooria Hadikhani, a new PhD student at LO, and Miguel Modestino.

Bibliography

1. M. A. Goulet and E. Kjeang, *J Power Sources*, 2014, **260**, 186-196.
2. E. Kjeang, N. Djilali and D. Sinton, *J Power Sources*, 2009, **186**, 353-369.
3. M. A. Modestino, D. Fernandez Rivas, S. M. H. Hashemi, J. G. E. Gardeniers and D. Psaltis, *Energy & Environmental Science*, 2016.
4. M. A. Modestino, S. M. H. Hashemi and S. Haussener, *Energy & Environmental Science*, 2016, **9**, 1533-1551.
5. J. W. Choi, S. M. H. Hashemi, D. Erickson and D. Psaltis, *Biomicrofluidics*, 2014, **8**.
6. S. M. H. Hashemi, J. W. Choi and D. Psaltis, *Physical Chemistry Chemical Physics*, 2014, **16**, 5137-5141.
7. M. A. Modestino, M. Dumortier, S. M. H. Hashemi, S. Haussener, C. Moser and D. Psaltis, *Lab Chip*, 2015, **15**, 2287-2296.
8. S. M. H. Hashemi, M. A. Modestino and D. Psaltis, *Energy & Environmental Science*, 2015, **8**, 2003-2009.
9. S. Hashemi, M. Neuenschwander, P. Hadikhani, M. Modestino and D. Psaltis, *J Power Sources*, 2017, **348**, 212-218.

Chapter 2

The potential for microfluidics in electrochemical energy systems

Flow based electrochemical energy conversion devices have the potential to become a prominent energy storage technology in a world driven by renewable energy sources. The optimal design of these devices depends strongly on the tradeoffs between the losses associated with multiple transport processes: convection and diffusion of reactants and products, migration of ionic species, and electrical charge transport. In this chapter, we provide a balanced assesment of the compromise between these losses and demonstrate that for a broad range of electrochemical reactors, the use of microfluidics can enhance the energy conversion efficiency. Moreover, we propose proven scale-up strategies of microelectrochemical reactors which could pave the way to the large scale implementation of energy microfluidic systems.

2.1 Introduction

The ever-increasing drive towards the implementation of clean energy technologies and processes has propelled a strong interest towards the development of deployable energy conversion devices¹. These devices need to capture energy from renewable sources such as wind and sunlight, and convert it into usable and preferably storable forms. Historically, our society has learned that economies of scale drive energy technologies towards large dimensions: big ships for transportation and long pipelines to pump oil from reservoirs to large refineries, massive hydroelectrical dams and large nuclear power plants. In this line of thought one tends to forget that many important phenomena related to energy and mass transfer occur at very small scales. Furthermore, often the concept of scale gets confused with scalability. These considerations can result in the premature dismissal of promising energy technologies with *small* operating cells that may be intrinsically scalable. State-of-the-art electrochemical energy conversion devices (e.g. batteries, fuel cells, electrolyzers, flow batteries, among others) fall into this category; small operating units that can be parallelized to reach power conversion at the megawatt scale. The small size of the units encountered in these systems is inherent of the multiple mesoscale processes (from nanometers to hundreds of micrometers) that occur within them: redox reactions, transport of charge carriers to electrodes, and mass transport of ions, reactants and products to and from reaction sites (Figure 2.1)².

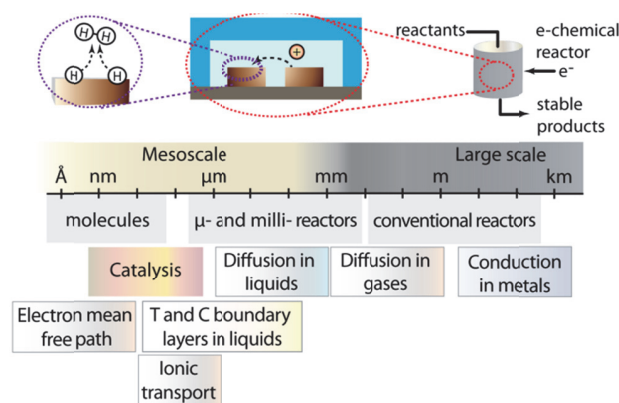


Figure 2.1 Diagram describing the multiple processes present in electrochemical energy conversion devices. From left to right, processes are presented in order of increased limiting scales. As observed, most of the processes lie within the mesoscale.

Within this chapter, we intend to provide a fair, yet not exhaustive assessment of *small* technologies and their potentials to impact *big* energy applications. Specifically, we will focus on microfluidic electrochemical energy conversion devices, and identify the conditions under which they can be implemented in a scalable way. While scaling traditional microfluidic devices is challenging, we will point

out reactor architectures that are different than lab scale microfluidic chips but can still harness the transport phenomena advantages of microfluidic regimes. Additionally, we identify opportunities where microsystems can be implemented at earlier stages for smaller and specialized energy applications.

2.2 Why microsystems for electrochemical energy conversion?

Is there really “space” for “small” technologies in the energy challenges faced by our society? What do microsystems have to offer that large-scale technologies have not already provided? We hope that at the end of this chapter our answers to these questions become evident, and we inspire readers to envision new ways in which devices with microstructures can be implemented, or can be used to improve the efficiency, and the potential economic viability of energy conversion devices. For consistency, this chapter will refer to microsystems as devices with at least one characteristic dimension in the micrometer scale. These devices could either operate in a continuous fluid flow regime (microfluidics), such as in the case of electrolyzers, fuel cells and flow batteries, or in a static regime such as batteries or supercapacitors.

The most significant consequence of going micro is the fact that by decreasing a characteristic length L (e.g. channel width, distance between electrodes, etc.), the concentration, temperature or other gradients are increased. Fluid flow in microchannels usually falls within a laminar regime that provides greater control over the flow. Additionally, short radial diffusion times result in a narrow residence-time distribution as well as an enhancement in heat and mass transfer, Peclet number ~ 0 . Moreover, microdevices have large surface-to-volume ratio (m^2/m^3), which makes them particularly interesting for processes dictated by surface phenomena³. These features allow the systems to reach thermal or surface reaction equilibrium much faster due to an increased mass and heat flux (over a given area L^2). Although the enhanced heat transfer of microfluidic reactors can accelerate the transformations that occur inside the device, it can also result in larger heat losses to the external environment. This can be used to the advantage of energy conversion devices that require active cooling, but can be detrimental to other systems that require additional energy inputs to operate at elevated temperatures (e.g. solid oxide fuel cells).

Many groups have reported on the uses of microfluidic reactor technology for chemical synthesis in academic research settings, and recently it has become more prominent in industrial processes^{4, 5}. Life-cycle analysis has hinted to significant ecological advantages of microreactors when compared to their macro-scale counterparts. The bulk of the interest in microfluidic systems has been centred on the production of high-value chemicals in the pharmaceutical and

fine chemistry industry. Only until recently, researchers have started exploring the space for microfluidic technologies in the energy field because of their potential to improve the conversion efficiency of devices, to better understand energy conversion processes and be implemented in niche applications that require energy systems with small footprints⁶.

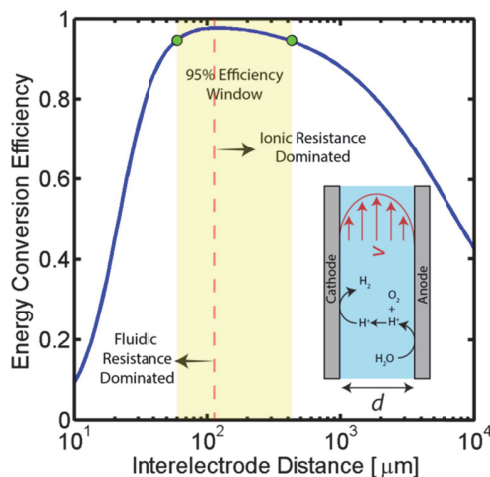


Figure 2.2. Trade-off between ionic and fluidic resistance as a function of distance between electrodes d , for a water electrolyzer operated at 10^4 A m^{-2} in a 1 M sulfuric acid electrolyte with an areal flow rate, Q , of $10^{-4} \text{ m}^2/\text{s}$. A maximum fractional device efficiency of 98% is achieved at $d=120 \text{ } \mu\text{m}$ (denoted by a red dashed line), and efficiencies above 95% are achievable in the window between 60 and 400 μm (highlighted in yellow). Lower separations lead to large fluidic resistances, while larger separations result in large losses from ionic transport.

To better demonstrate the power of scalable microsystems in electrochemical energy conversion, we will introduce a simple model electrosynthetic device as an example of a prototypical electrochemical energy conversion device (Figure 2.2). This model consists of a set of infinite parallel plate electrodes separated by a distance, d . In between the electrodes, a liquid electrolyte flows with a given areal flow rate, Q . An electrical potential is applied between the two infinite, parallel plates so that an electrochemical reaction can take place at the surface of the electrodes at a rate imposed by a constant current density, j . The thermodynamic equilibrium potential for the reaction is given by E^0 , and is imposed by the nature of the chemical transformation taking place. For simplicity, we will assume a fully developed (parabolic) flow of a Newtonian electrolytic fluid between the electrodes, a uniform electrolyte conductivity, σ , across the channel, no mass transport limitations at the surface of the electrodes, and that the volume fraction of products in the electrolyte is negligible. Within these conditions, the only two factors that depend on d and affect the energy conver-

sion efficiency are the ionic and fluid resistances. The power loss arising from ionic resistance, P_{ion} , over a reactor length, L , is given by,

$$P_{ion} = \frac{j^2 d L}{\sigma} \quad (1)$$

while the power loss due to fluidic resistance, P_{fluid} , depends on the electrolyte viscosity, μ , and is determined by,

$$P_{fluid} = \frac{12 \mu Q^2 L}{d^3} \quad (2)$$

These losses can be compared with the chemical energy stored in the products, $P_{storage}$,

$$P_{storage} = j E^0 \quad (3)$$

to obtain a fractional efficiency for the device,

$$\eta = \frac{P_{storage}}{P_{storage} + P_{ion} + P_{fluid}} \quad (4)$$

that excludes kinetic losses at the electrocatalyst.

As demonstrated in Figure 2.2 for a water splitting device, the maximum energy conversion efficiency is achieved when the separation between electrodes is in the microscale (120 μm in this example at a current density of 10^4 A m^{-2}). Moreover, for this example, an algebraic expression can be obtained that defines the optimal electrode separation for maximum energy conversion efficiency,

$$d_{opt} = \left(\frac{36 \mu \sigma Q^2}{j^2} \right)^{\frac{1}{4}} \quad (5)$$

or more conveniently as a function of average fluid velocity, v ,

$$d_{opt} = (36 \mu \sigma)^{\frac{1}{2}} \frac{v}{j} \quad (6)$$

where μ and σ are electrolyte properties, while v and j are operational parameters. This expression is independent of the nature of the electrochemical reaction taking place at the electrodes, and only depends on the electrolyte selection. To generalize our findings, we can explore the range of optimal electrode spacing as a function of operational parameters. For typical aqueous electrolytes the viscosity and conductivity are in the order of $\sim 10^{-3} \text{ Kg/m-s}$ and $\sim 10 \text{ S/m}$, respectively. Assuming practical ranges of average velocities and current densities, it can be demonstrated that within most operating conditions, optimized fluidic electrochemical devices should have electrode separations in the microscale, $< 500 \mu\text{m}$ (Figure 2.3). Equivalent analyses can be carried out for solar-fuel generators,

fuel cells and flow batteries, and similar scaling laws can be drawn from those devices. In all of these systems, the low conductivity of electrolytes drives the device design towards the microscale, even if fluidic losses are increased⁷.

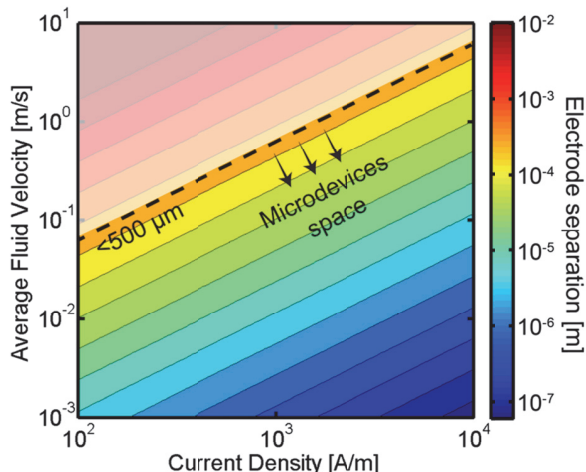


Figure 2.3. Optimal electrode separation as a function of current density and fluid velocity. Most of the operation conditions require a distance between electrodes in the microscale. As shown in the shadowed top left region of the image, those applications that require high flow speeds and low current densities have optimal interelectrode distances in the macroscale.

In addition to the efficiency improvements demonstrated above, microfluidic technologies offer several other benefits. Microfluidic energy conversion devices could lead to increases in power density thanks to the low amount of electrolytes required. Also, fluidic forces could be used to precisely direct species to the desired device locations, reducing losses due to mixing of reactants or products. Motivated by these performance gains, several groups have already started to exploit the multiple advantages that microsystems bring to the electrochemical energy conversion field. Below, we will briefly review the state of the art in electrochemical energy conversion microsystems and compare their performance with their large scale, conventional counterparts.

2.3 State-of-the-art electrochemical energy conversion microsystems

Microsystems have already found applications in a broad range of electrochemical energy conversion devices. Most notably, batteries are manufactured with an interelectrode spacing in the microscale. The small separation is desirable in order to avoid unwanted ohmic losses in the electrolyte and achieve a high energy density while still maintaining the electrodes separated avoiding short-circuiting the device. Moreover, the miniaturization of batteries driven by the extensive use of laptops, cell phones and other portable consumer electronics has

resulted in highly efficient and energy dense systems. Miniaturized flow-based electrochemical systems such as electrolyzers, fuel cells or flow batteries could also be implemented into electronic devices and potentially reach energy densities that surpass those of batteries. Furthermore, this class of energy devices could enjoy improvements in their efficiency, energy density, and materials utilization if they were designed with microscale features to facilitate the transport of reactants, products and ionic charge carriers. Additionally, the high surface area to volume ratio of microreactors is particularly useful in electrochemical systems, as the chemical transformations take place only at the surface of electrodes. In order to provide a broader context on flow-based electrochemical energy conversion microsystems the subsections below present an overview of the main advances and state of the art in the field of microfluidic fuel cells, flow batteries and electrolyzers.

Fuel Cells. Among the three device categories cited above, microscale fuel cells are the most studied and well-established systems. Their development has been particularly motivated by the need for high energy density power sources in portable devices. Integration of small hydrogen (H_2) fuel cells can address this issue due to the large mass energy density of H_2 ⁸. Additionally, fuel cells can be charged quickly, typically by changing a hydrogen cartridge or refilling the reservoir.

The two main types of fuel cells that have been implemented in the microfluidic regime are solid oxide fuel cells (SOFCs) that work at high temperatures, typically in the order of 100's °C, and proton exchange membrane fuel cells (PEMFCs) which generally operate at room temperature. The maximal theoretical efficiency of SOFCs is a strong function of their operating temperatures. For a SOFC using CO as a fuel, the theoretical energy conversion efficiency is 63% at 900°C and 81% at 350°C when entropic losses are accounted⁹. Unfortunately, operating at high temperatures requires long start-up and shutdown cycles, limiting their usability for portable applications. The maximal theoretical efficiency of PEMFCs accounting for entropic losses is 83% at 25°C. However the state of the art PEMFCs operate at efficiencies in the order of 60%. It is interesting to note that in traditional, large scale PEMFCs, the dimensions of the channels in the flow plates are typically manufactured in the submillimeter scale¹⁰ to mediate mass transport limitations. Furthermore, the thickness of the polymeric electrolyte membrane tends to be in the order of tens of micrometers, since a small ohmic drop is desirable between the two electrodes. Decreasing the thickness of flow plates is also important since these components account for more than 80% of the total weight and 30% of the total cost of fuel cells¹¹.

The most prominent reactants in conventional PEMFCs are hydrogen and oxygen. For portable applications, hydrogen needs to be compressed to high pressures or stored in the structure of solid materials with higher volumetric energy density such as metal hydrides¹². The challenges related to the storage of H₂ result in additional costs and design complexity, posing significant obstacles for the implementation of H₂ in portable devices. Due to this fact, parallel research lines have evolved to develop fuel cells that operate with alternative fuels. To this end, alternative liquid fuels have been implemented including: methanol, ethanol, 2-propanol, ethylene glycol (EG), dimethoxymethane (DMM), formic acid, hydrazine, hydrogen peroxide, and dimethyl ether (DME)¹³. Liquid oxidants such as hydrogen peroxide and nitric acid have also been used as alternatives to oxygen in the cathodic reaction. Another interesting example of micro fuel cells are laminar flow based systems that operate without membranes. These devices take advantage of the slow diffusion-dominated mixing between fuel and oxidant streams to minimize reactant crossover. A key requirement for these systems is to keep the residence time of the fluids inside the channels small – high Péclet numbers – so that diffusion is minimal compared to convective transport. This can simplify the device design, reduce the cost of materials and fabrication, and the weight of the device. On top of that, an improved performance is possible due to higher conductivity in liquid electrolytes compared to polymer membranes. Higher power densities are achieved if the flowrates of fuel and oxidant streams are increased. Under fast flow rates, mass-transport of the fuel is enhanced but at the same time a large fractions of the fuel can exit the device without reacting at the electrode. To circumvent these fuel utilization limitations, clever device architectures can be implemented to increase the active contact area between the electrodes and the reactants¹⁴, as well as engineered channel and electrode geometries that promote high fuel utilization, reaching levels above 90%, and deliver high power densities¹⁵. Moreover, elimination of the polymer electrolyte relaxes the challenges of using alternative chemistries in PEMFCs such as the high permeability of methanol and other liquid fuels in Nafion¹⁶. These types of micro fuel cells have been reviewed extensively^{15, 17-20} and some examples achieve power densities in the same order of magnitude as in state-of-the-art macroscale PEMFCs^{21, 22}. Table 2.1 highlights some examples of micro fuel cell systems and provides information regarding the design characteristics, maximum power density, as well as oxidant and fuel used in each study.

Lastly, it must be noted that new classes of micro fuel cells are emerging where the unique features of microfluidics enables their realization. Two examples will be mentioned here: paper based microfluidic fuel cells and optofluidic fuel cells.

Table 2.1 Selected examples of top-performing micro fuel-cell devices for various fuel and oxidant combinations

Reference	Fuel	Oxidant	Electrolyte	Inter-electrode Distance [μm]	Design Characteristics	Peak Power Density [mW/cm ²]	Maximum Current Density [mA/cm ²]	Maximum Open Circuit Voltage [V]
R.C. Sekol et al. ²³	H ₂	O ₂	Nafion 212	50.8	Merging flow field and current collector functionalities by micro/nanostructuring glassy metal	1080 at 0.25 V	294	0.94
S.J. Lee et al. ²⁴	H ₂	O ₂	Nafion 115	125	Planar stack with miniaturized fuel-cell units interconnected in series.	42 (4 cells in series)	210 (4 cells in series)	3.1 (4 cells in series)
S. A. Mousavi Shaeigh et al. ²⁵	H ₂ O ₂	H ₂ O ₂	0.1 M HCl	-	H ₂ O ₂ working as both fuel and oxidant over selective electrocatalysts	1.55 at 0.3 V	10	0.6
N. Da Mota et al. ²²	0.15 M NaBH ₄ in 3 M NaOH	0.5 M H ₈ N ₉ CeO ₁₈ in 1 M HNO ₃	3 M NaOH and 1 M HNO ₃ separated by a porous barrier	410	Staggered-herringbone structures on the electrodes to induce oxidant/fuel mixing in cathodic/anodic reaction and alleviate mass transport limitation	270 at 0.65 V	480	2.2
A.S. Hollinger et al. ²⁶	1 M Methanol	O ₂	1 M H ₂ SO ₄	306	Introduction of a nanoporous separator to the interface of fuel and electrolyte in order to limit the fuel diffusion area and increase the P _{max} by 45%.	70 at 0.2 V (80 °C)	660 (80 °C)	0.65 (80 °C)
R.S. Jayashree et al. ²⁷	1 M HCOOH	O ₂	0.5 M H ₂ SO ₄	1000-2000	Hydrodynamic focusing of the fuel to a thin stream on anode and reducing is crossover to the cathode while increasing fuel utilization	55 at 0.3 V	320	0.86
J. An et al. ²⁸	H ₂	air	Yttria-Stabilized Zirconia (YSZ)	0.06	3D nanostructuring of an ultrathin YSZ electrolyte and integration of highly active yttria doped ceria (YDC) at the cathode side to increase active area while decreasing ohmic and activation losses	1300 at 0.32 V (450 °C)	7200 (450 °C)	1.08 (450 °C)
V. Galvan et al. ²⁹	5 M HCOOK	30% H ₂ O ₂	5 M HCOOK and 30% H ₂ O ₂	-	Capillary flow of fuel and oxidant through paper makes the fabrication cheap and easy.	2.53	11.5	1.1
L. Li et al. ³⁰	Thin methylene blue solution	O ₂	0.5 M NaOH	200	Photooxidization of organic pollutants and generating power while treating the water.	0.45	1.05	1.04

The paper based microfluidic FCs aim at developing inexpensive and disposable power sources. They take advantage of the capillary flows in flow plates made of paper to bring in the fuel and oxidant over the surface of electrodes from dedicated reservoirs. This technique eliminates the need for peripheral equipment such as pumps and can result in significant cost reductions thanks to the simplicity of the fabrication methods and the use of inexpensive materials.³¹⁻³³ Some of these devices are able to deliver energy for long periods of time and, therefore, are appropriate for low power consumer electronics^{29, 34}.

Optofluidics is a field that integrates microfluidics with optics and that has found potential applications in the energy domain⁴. Recently, optofluidic approaches have been implemented to generate electricity through the photocatalytic oxidation of organic pollutants in water^{30, 35}. The high surface to volume ratio at microscales and the possibility of fabricating transparent microfluidic devices together with controlling light/fluid interactions makes optofluidics a powerful tool for solar-based energy conversion.

Flow Batteries. Flow batteries are rechargeable fuel cells which operate by placing two redox active chemical species dissolved in two liquid streams separated by an electrolyte (usually a membrane). These chemical species can be reduced or oxidized during charging or discharging cycles. Fuels and oxidant liquids are flown into the device from two separate reservoirs during discharge to generate electricity, and by reversing the process the oxidized fuel and reduced oxidant can be restored to their initial state during charge cycles. Only a few examples of micro flow batteries have been reported, and they predominantly focus on the elimination of ion-conducting membranes by implementing the aforementioned laminar flow technique. Notable approaches involve the co-laminar flow of solutions containing vanadium redox couples through porous electrodes, with demonstrated power densities as high as 330 mW/cm^2 ^{36, 37}. More recently, a hydrogen bromine laminar flow battery was demonstrated³⁸. This device achieved a remarkable power density of 795 mW/cm^2 , approaching the performance of state-of-the-art H_2 fuel cells.

Electrolyzers. Unlike fuel cells, literature reports on micro electrolyzers are limited, presumably due to the low throughput of such devices, which makes them less attractive for commercial utilization. Despite the fact that microelectrolyzers will find limited usability in large-scale hydrogen production, applications that require lower production rates are often overlooked. A relevant example is the implementation of water splitting units in solar fuel devices, where typical current densities in the light-absorber are in the order of 10 mA/cm^2 whereas electrolyzers' catalyst layers can support current densities up to several A/cm^2 ^{2, 39, 40}. This implies that a relatively large photovoltaic device can be combined

with miniaturized electrolyzers for optimum cost and performance⁴¹. Additionally, controlling transport phenomena at the microscale can bring efficiency improvements, eventually leading to benefits for large-scale electrolyzers.

Table 2.2 Selected examples of microelectrolyzers

Reference	Cathode	Anode	Electrolyte	Interelectrode Distance [μm]	Design Characteristics	Maximum Current Density [mA/cm^2]
M.A. Modestino et al. ⁴²	Pt	Pt	Nafion 117 and 0.5 M H_2SO_4	163.5	In plane electrodes with Nafion membrane as the top wall of microchannels allowing for photoelectrodes integration	175 at 2.5 V
S. M. H. Hashemi et al. ⁴³	Pt or NiFe	Pt or NiFe	1 M H_2SO_4 or 1 M K_2CO_3 or 1 M Na_3PO_4 buffer	175	Versatility in selection of electrolyte and catalysts due to the flow based gas separation mechanism	300 at 2.5 V
M.A. Modestino et al. ⁴⁴	Pt	Pt	Spin casted Nafion thin film	150	Vapor fed microelectrolyzer with double spiral microchannels for design simplicity	Less than 10 at 3 V
M.E. Oruc et al. ⁴⁰	Pt	Pt	0.5 M H_2SO_4	-	Microelectrolyzer absorbing the heat from the attached PV and therefore increasing the overall efficiency of PVTE system	10 at 1.82 V (80 °C)

The first microfluidic electrolyzer was demonstrated in 2013 providing a current density of over $100 \text{ mA}/\text{cm}^2$ at 2.5 V⁴². Within the framework of this dissertation, electrolyzers that can operate under vapor-feeds⁴⁵ and without membranes⁴³ have been enabled thanks to the control of transport processes in the microscale. The vapor fed device takes advantage of small diffusion and ionic path lengths in microfluidics to split the water content of ambient air. In the membrane-less device, the gas separation task is achieved by exploiting fluidic forces to guide the product gases to independent collection ports. Furthermore, by eliminating the need of a membrane, the ohmic resistance in the electrolyte is reduced and current densities as high as $300 \text{ mA}/\text{cm}^2$ at 2.5 V can be achieved. Recent work in this domain also includes the analysis⁴⁶ and implementation⁴⁷ of a micro electrolyzer integrated with solar cells. In this system, synergistic effects can be achieved by cooling the photovoltaic components while at the same time enhancing the efficiency of the electrolysis process^{39, 48}. A summary of the characteristics of previously reported microelectrolyzers is listed in Table 2.2. It is also worth noting that in addition to water electrolysis, there are several examples of microsystems that use alternative pathways for the generation of hydrogen. These include metal hydride microreactors⁴⁹⁻⁵¹ and methanol steam reforming microreactors^{52, 53}.

2.4 Scalability and manufacturability of energy microsystems

The previous sections described multiple advantages of flow-based energy microsystems, but their implementation into real-world application would ultimately depend on their scalability and our ability to manufacture them in cost-effective ways. In microsystems engineering, the most frequent way to scale the throughput is by internal numbering-up, which involves the incorporation of parallel arrangements of single microstructured units (e.g channels, electrodes)⁵⁴. In this way, the advantages achieved by microstructuring units can be maintained in higher throughput systems. It must be noted that numbering-up strategies are challenging and alternatives should be sought when possible. Parallelization of microdevices requires complex fluidic interconnections and manifold-ing. Also, if classical microfluidic chips are used as building blocks, the majority of the volume of the device would act as a dead volume and not participate in the chemical transformations of interest. This is in contrast with common approaches used for the scale-up of homogeneous chemical reactions that involve the volumetric scaling of reactors. In the case of electrochemical energy conversion devices, the scale-up strategy will depend on the number of processes that require transport length-scales in the micro domain. If all of the processes with a microscale dimensionality requirement occur in parallel directions, then the system can be scaled by increasing area. An areal scale-up strategy would involve the implementation of macroscopic plate electrodes separated by a micro scale distance. By doing so, classical manufacturing techniques could be implemented, simplifying the overall scale-up process. If at least two processes require transport path lengths in the microscale, and their directions are orthogonal, then the only option to scale-up the device throughput is to parallelize the units (numbering up). Figure 2.4 shows a representation of the different scaling strategies described above. When determining the dimensionality of the transport process involved in energy conversion microsystems it is useful to define the characteristic path length for the species or charge carriers involved. In electrochemical devices, usually the transport processes that dominate the performance of the system are the transport of charge carriers – electrons, holes and ionic species – and the transport of neutral species – reactants and products. The characteristic length scale for transport of charged species, l_{ion} or l_e for ions or electrons respectively, is determined by Ohms law,

$$l_{ion/e^-} = \frac{\Delta V_{ohm} \sigma}{j_{op}} \quad (7)$$

based on the operating current density of the device, j_{op} , the allowable voltage drop, ΔV_{ohm} , and the conductivity of the transport media (i.e. electronic conductors or electrolytes). In the case of neutral species transport, the characteris-

tic length scale, l_{neu} , depends on the species diffusivity, D , and its characteristic concentration in the reactor, c_0 ,

$$l_{neu} = \frac{Dc_0nF}{j_{op}} \quad (8)$$

where F is Faraday's constant and n is the stoichiometric number of electrons involved in the electrode reaction. Based on characteristic transport properties of metallic electrodes, electrolytes and neutral species involved in the redox reactions, one can estimate the range of the characteristic length required for operations under different current density regimes (Table 2.3). The estimation of these length scale requirements can aid in the design of electrochemical reactors and the decision on their scaling strategy. For example, for the devices summarized in Section 2.3, if only the ion transport processes are required to occur in the microscale (1D), an areal scale-up strategy can be implemented.

Table 2.3. Characteristic length scales for transport processes involved in electrochemical energy conversion devices

<i>Charged Species[‡]</i>			
Species	Characteristic Conductivity (σ)	Current Density (j_{op})	Length Scale (l_e or l_{ion})
Electrons in metallic electrodes	$10^5 - 10^7 \text{ S m}^{-1}$	Low ($100-10^3 \text{ A m}^{-2}$)	$10-10^4 \text{ m}$
		High ($10^4 - 10^5 \text{ A m}^{-2}$)	$0.1-100 \text{ m}$
Ions in electrolytes	$0.1-10 \text{ S m}^{-1}$	Low ($10-10^3 \text{ A m}^{-2}$)	$10-10^4 \text{ }\mu\text{m}$
		High ($10^4 - 10^5 \text{ A m}^{-2}$)	$0.1-100 \text{ }\mu\text{m}$

[‡]The allowable voltage drop, ΔV_{ohm} , as assumed to be 0.1 V.

<i>Neutral Species</i>			
Species	Characteristic Properties	Current Density (j_{op})	Length Scale (l_{neu})
Low Solubility Species	$c_0 \sim 1 \text{ mol m}^{-3}$ $D \sim 10^{-9} \text{ m}^2 \text{ s}^{-1}$	Low ($100-10^3 \text{ A m}^{-2}$)	$0.1-1 \text{ }\mu\text{m}$
		High ($10^4 - 10^5 \text{ A m}^{-2}$)	$1-10 \text{ nm}$
High Solubility Species	$c_0 \sim 10^3 \text{ mol m}^{-3}$ $D \sim 10^{-9} \text{ m}^2 \text{ s}^{-1}$	Low ($10-10^3 \text{ A m}^{-2}$)	$100-10^3 \text{ }\mu\text{m}$
		High ($10^4 - 10^5 \text{ A m}^{-2}$)	$1-10 \text{ }\mu\text{m}$

Once a scale-up strategy has been identified, the next step is to assess the manufacturability of the scalable system. Areal scaling of electrochemical reactors is usually preferred whenever allowable. Under this strategy a large suite of common fabrication techniques can be implemented to achieve the desired structure. Classical machining can be used to manufacture parts where parallel planar electrodes are separated by 100's μm . Reactor manufacturing methods include

laminate or sheet construction techniques which have been used extensively to perform gas-liquid reactions and processes with film plates⁵⁵, e.g. methane steam reforming⁵⁶. This fabrication method offers flexibility in design and can accommodate multiple reactor units within a single component. Different layers of a laminate structure can be easily machined to define internal passages and channel structures. Also, as the limiting dimension in laminated reactors is defined by the thickness of the layers, interelectrode spacings in the microscale can be easily accessed. These fabrication techniques open the possibility for producing large throughput reactors at relatively low cost. Another successful scale-up example involves the redesign of a sonochemical microreactor for the controlled generation of chemically active bubbles. While the initial concept and proof-of-principle demonstrations were developed in a silicon-based device⁵⁷, large-scale reactors were redesigned using inexpensive polymeric materials in order to improve its commercialization potential⁵⁸.

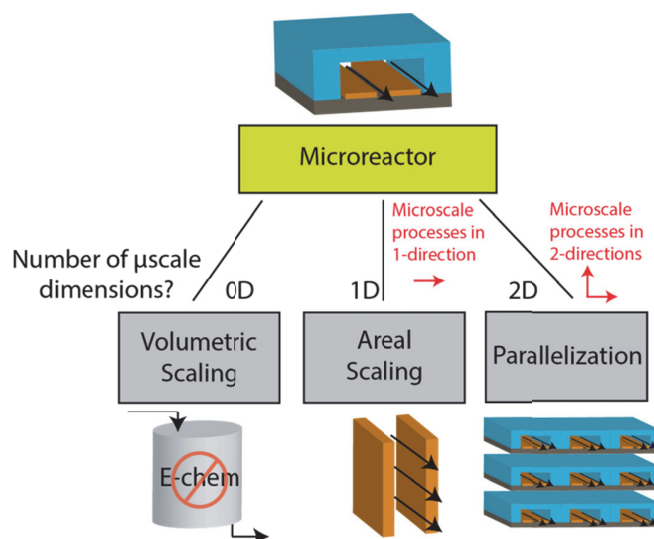


Figure 2.4 Scaling strategies for increasing the throughput of microfluidic reactors. Volumetric scaling is often used for homogeneous chemical processes where the dimensionality of the reactor does not affect the reactions (0D). Areal scaling can be applied if all the limiting transport processes that require microscale path lengths can be carried out in one dimension (1D). A parallelization strategy of microdevices is needed when the system involves more than one dimension in the microscale ($\geq 2D$).

The use of inexpensive elastomers (e.g. PDMS) that boosted other microfluidics applications over the last decades cannot be directly used in the context of energy applications, unless new functionalized and resistant materials are integrated. Chemical compatibility and gas permeability of polymers are constraints for the long-term temperature and pressure cycling requirements of energy conversion devices. To that end, silicon and glass have suitable characteristics and have

been exploited on energy related lab-on-a-chip applications where microfluidics have been proved to be powerful tools to gain important insights in the energy conversion processes present in large-scale reactors⁶. Microreactors that require parallelization to achieve higher throughput face more difficult challenges for their fabrication. They also can present operational difficulties when the evolution of a different phase (e.g. solid or gas) occurs inside the microchannels (e.g. H₂ and O₂ evolved at the surface of electrodes). The presence of multiphase flows within reactors can cause blockage of fluidic channels, decrease in electrolyte conductivity, additional pressure drops, a reduction of the electrode active area, among other problems. Strategies to mitigate these issues will need to be incorporated in the reactor design phase. Parallelization strategies also require cost-intensive manufacturing techniques. Specifically, material costs tend to be low, yet the costs of the facilities where the fabrication takes place are high. For example, microreactors based on semiconductor technologies are processed only in cleanroom environments. Also, it is not straightforward to make arbitrary reactor shapes using classical Si processing techniques, and fabrication of early stage prototypes tend to be time-intensive. Alternatively, the recent advent of additive manufacturing (AM) technologies has resulted in a change in paradigm for the fabrication of customizable prototypes⁵⁹. The flexibility in materials used together with reduced time for developing functional prototypes, provides a powerful tool that can result in faster technical solutions not achievable with other fabrication techniques. The resolution of features achievable depends strongly on the specific material and technology used. Resolution in the order of 100's μm are commonly achieved⁶⁰. Sub-classification of 3D micro additive manufacturing has been proposed as scalable additive manufacturing, 3D direct writing, and hybrid processes; details can be found in recent literature with key processes and resolutions attainable⁶¹⁻⁶³.

It is important to point out that in many flow-based electrochemical conversion devices, the capital cost of each device tends to be significantly lower than the cost of the fuel (in fuel cells) or electricity (in electrolyzers and flow batteries) required for their operation over their lifetime^{41, 64, 65}. Given this situation, the savings from efficiency improvements in microscale devices only need to outweigh the increased capital cost requirement.

2.5 Conclusions and perspective

Energy systems have stringent efficiency, scalability and cost-effectiveness requirements. As the world pressingly moves towards clean energy sources, the need to incorporate electrochemical energy conversion devices into the electricity grid will certainly increase, as well as the need to develop ever more efficient and cost-competitive systems that can reach large scale energy storage and pro-

duction. This chapter aspires to provide a balanced analysis of the potential advantages of developing flow-based electrochemical energy conversion microdevices. We have explored three basic questions: (1) Can microsystems bring efficiency improvements? (2) Can they be scaled? And if so, (3) can they be economically viable? The answer to the first question is most definitively positive. By developing electrochemical reactors in the microscale, the transport path lengths can be reduced so that ionic transport losses and mass transport limitations for reactants and products can be minimized. On the other hand, by reducing the size of channels the fluidic resistance of devices increases, resulting in additional energy losses. Earlier in this chapter we demonstrated that the trade-off between these two effects points towards a maximum efficiency of devices when their interelectrode distance is between a few 10's to a few 100's of μm . These efficiency advantages have been an important motivation for the demonstration of the microfluidic energy conversion devices described in Section 2.3. This brings us to the second question: in order to harvest the advantages of microsystems we must be able to scale them up. Section 2.4 described the scale-up strategy based on the dimensionality of the limiting transport processes involved in the device. It is clear that within a large range of operating conditions of interest, both the transport of ions and reactants/products can become limiting if their transport path lengths are not restricted to the micro-domain. If the direction of these two transport processes can be accommodated in the axis normal to the plane of the electrodes, then devices can be easily scaled in a two dimensional way (i.e. large planar electrodes can be placed parallel to each other and be separated by an electrolyte flow). Under these conditions, inexpensive manufacturing processes can be implemented and have the potential to lead to cost-effective large-scale microfluidic reactors. If parallelization of microfluidic channels is required, the fabrication methods are expected to be more complex and the reactors' economic viability limited. To that end, new fabrication techniques such as high-resolution additive manufacturing have the potential to change this paradigm and lead to scalable and cost-effective energy microsystems.

Microsystems will certainly continue to occupy an important space in the energy field in years to come. Energy storage and conversion devices will become more prominent as renewable energy technologies continue to penetrate the energy markets. To that end, achieving higher efficiency in energy conversion systems will become critical, and the advantages provided by microfluidic energy devices will play a significant role. At the same time, while these advantages are demonstrated at the laboratory scale, industry will be encouraged to incorporate and develop innovative manufacturing techniques to harvest the improvements that microfluidic energy technologies can bring.

Bibliography

1. S. Chu and A. Majumdar, *Nature*, 2012, **488**, 294-303.
2. M. A. Modestino, S. M. H. Hashemi and S. Haussener, *Energy & Environmental Science*, 2016, **9**, 1533-1551.
3. O. Brand, G. K. Fedder, C. Hierold, J. G. Korvink, O. Tabata and N. Kockmann, *Micro process engineering*, John Wiley & Sons, 2013.
4. D. Erickson, D. Sinton and D. Psaltis, *Nat Photonics*, 2011, **5**, 583-590.
5. K. S. Elvira, X. C. i Solvas and R. C. Wootton, *Nature chemistry*, 2013, **5**, 905-915.
6. D. Sinton, *Lab on a Chip*, 2014, **14**, 3127-3134.
7. J. Newman, *Journal of The Electrochemical Society*, 2013, **160**, F309-F311.
8. P. P. Edwards, V. L. Kuznetsov, W. I. F. David and N. P. Brandon, *Energy Policy*, 2008, **36**, 4356-4362.
9. E. D. Wachsman and K. T. Lee, *Science*, 2011, **334**, 935-939.
10. L. F. Peng, X. M. Lai, P. Y. Yi, J. M. Mai and J. Ni, *Journal of Fuel Cell Science and Technology*, 2011, **8**.
11. X. G. Li and M. Sabir, *International Journal of Hydrogen Energy*, 2005, **30**, 359-371.
12. M. B. Ley, L. H. Jepsen, Y.-S. Lee, Y. W. Cho, J. M. Bellosta von Colbe, M. Dornheim, M. Rokni, J. O. Jensen, M. Sloth, Y. Filinchuk, J. E. Jørgensen, F. Besenbacher and T. R. Jensen, *Materials Today*, 2014, **17**, 122-128.
13. W. Qian, D. P. Wilkinson, J. Shen, H. Wang and J. Zhang, *Journal of Power Sources*, 2006, **154**, 202-213.
14. A. Bazylak, D. Sinton and N. Djilali, *Journal of Power Sources*, 2005, **143**, 57-66.
15. E. Kjeang, N. Djilali and D. Sinton, *J Power Sources*, 2009, **186**, 353-369.
16. J. D. Morse, *International Journal of Energy Research*, 2007, **31**, 576-602.
17. S. A. M. Shaegh, N. T. Nguyen and S. H. Chan, *International Journal of Hydrogen Energy*, 2011, **36**, 5675-5694.
18. M. N. Nasharudin, S. K. Kamarudin, U. A. Hasran and M. S. Masdar, *International Journal of Hydrogen Energy*, 2014, **39**, 1039-1055.
19. M. A. Goulet and E. Kjeang, *J Power Sources*, 2014, **260**, 186-196.
20. M. Safdar, J. Janis and S. Sanchez, *Lab Chip*, 2016, **16**, 2754-2758.
21. R. S. Jayashree, M. Mitchell, D. Natarajan, L. J. Markoski and P. J. A. Kenis, *Langmuir*, 2007, **23**, 6871-6874.

22. N. D. Mota, D. A. Finkelstein, J. D. Kirtland, C. A. Rodriguez, A. D. Stroock and H. D. Abruña, *Journal of the American Chemical Society*, 2012, **134**, 6076-6079.
23. R. C. Sekol, G. Kumar, M. Carmo, F. Gittleson, N. Hardesty-Dyck, S. Mukherjee, J. Schroers and A. D. Taylor, *Small*, 2013, **9**, 2081-2085.
24. S. J. Lee, A. Chang-Chien, S. W. Cha, R. O'Hayre, Y. I. Park, Y. Saito and F. B. Prinz, *J Power Sources*, 2002, **112**, 410-418.
25. S. A. M. Shaegh, N. T. Nguyen, S. M. M. Ehteshami and S. H. Chan, *Energy & Environmental Science*, 2012, **5**, 8225-8228.
26. A. S. Hollinger, R. J. Maloney, R. S. Jayashree, D. Natarajan, L. J. Markoski and P. J. A. Kenis, *J Power Sources*, 2010, **195**, 3523-3528.
27. R. S. Jayashree, L. Gancs, E. R. Choban, A. Primak, D. Natarajan, L. J. Markoski and P. J. A. Kenis, *Journal of the American Chemical Society*, 2005, **127**, 16758-16759.
28. J. An, Y. B. Kim, J. Park, T. M. Gur and F. B. Prinz, *Nano Letters*, 2013, **13**, 4551-4555.
29. V. Galvan, K. Domalaon, C. Tang, S. Sotez, A. Mendez, M. Jalali-Heravi, K. Purohit, L. Pham, J. Haan and F. A. Gomez, *Electrophoresis*, 2016, **37**, 504-510.
30. L. Li, G. Y. Wang, R. Chen, X. Zhu, H. Wang, Q. Liao and Y. X. Yu, *Lab on a Chip*, 2014, **14**, 3368-3375.
31. J. P. Esquivel, F. J. Del Campo, J. L. G. de la Fuente, S. Rojas and N. Sabate, *Energy & Environmental Science*, 2014, **7**, 1744-1749.
32. K. H. Purohit, S. Emrani, S. Rodriguez, S. S. Liaw, L. Pham, V. Galvan, K. Domalaon, F. A. Gomez and J. L. Haan, *Journal of Power Sources*, 2016, **318**, 163-169.
33. T. S. Copenhagen, K. H. Purohit, K. Domalaon, L. Pham, B. J. Burgess, N. Manorohtkul, V. Galvan, S. Sotez, F. A. Gomez and J. L. Haan, *Electrophoresis*, 2015, **36**, 1825-1829.
34. M. J. González-Guerrero, F. J. del Campo, J. P. Esquivel, F. Giroud, S. D. Minter and N. Sabaté, *Journal of Power Sources*, 2016, **326**, 410-416.
35. H. Zhang, H. Z. Wang, M. K. H. Leung, H. Xu, L. Zhang and J. Xuan, *Chemical Engineering Journal*, 2016, **283**, 1455-1464.
36. J. W. Lee, M. A. Goulet and E. Kjeang, *Lab Chip*, 2013, **13**, 2504-2507.
37. E. Kjeang, R. Michel, D. A. Harrington, N. Djilali and D. Sinton, *Journal of the American Chemical Society*, 2008, **130**, 4000-4006.
38. W. A. Braff, M. Z. Bazant and C. R. Buie, *Nature Communications*, 2013, **4**.

39. M. A. Modestino and S. Haussener, *Annual Review of Chemical and Biomolecular Engineering*, 2015, **6**, 13-34.
40. M. E. Oruc, A. V. Desai, R. G. Nuzzo and P. J. Kenis, *Journal of Power Sources*, 2016, **307**, 122-128.
41. C. A. Rodriguez, M. A. Modestino, D. Psaltis and C. Moser, *Energy & Environmental Science*, 2014, **7**, 3828-3835.
42. M. A. Modestino, C. A. Diaz-Botia, S. Haussener, R. Gomez-Sjoberg, J. W. Ager and R. A. Segalman, *Physical Chemistry Chemical Physics*, 2013, **15**, 7050-7054.
43. S. M. H. Hashemi, M. A. Modestino and D. Psaltis, *Energy & Environmental Science*, 2015, **8**, 2003-2009.
44. M. A. Modestino, M. Dumortier, M. Hashemi, S. Haussener, C. Moser and D. Psaltis, *Lab on a Chip*, 2015, **15**, 2287-2296.
45. M. A. Modestino, M. Dumortier, S. M. H. Hashemi, S. Haussener, C. Moser and D. Psaltis, *Lab Chip*, 2015, **15**, 2287-2296.
46. M. E. Oruc, A. V. Desai, P. J. A. Kenis and R. G. Nuzzo, *Appl Energ*, 2016, **164**, 294-302.
47. M. E. Oruc, A. V. Desai, R. G. Nuzzo and P. J. A. Kenis, *Journal of Power Sources*, 2016, **307**, 122-128.
48. S. Tembhurne, M. Dumortier and S. Haussener, *15th International Heat Transfer Conference, Kyoto, Japan*, 2014.
49. D. Gervasio, S. Tasic and F. Zenhausern, *J Power Sources*, 2005, **149**, 15-21.
50. S. Moghaddam, E. Pengwang, R. I. Masel and M. A. Shannon, *J Power Sources*, 2008, **185**, 445-450.
51. L. Zhu, K. Y. Lin, R. D. Morgan, V. V. Swaminathan, H. S. Kim, B. Gurau, D. Kim, B. Bae, R. I. Masel and M. A. Shannon, *J Power Sources*, 2008, **185**, 1305-1310.
52. P. Reuse, A. Renken, K. Haas-Santo, O. Görke and K. Schubert, *Chemical Engineering Journal*, 2004, **101**, 133-141.
53. A. V. Pattekar and M. V. Kothare, *Journal of Microelectromechanical Systems*, 2004, **13**, 7-18.
54. T. Dietrich, *Microchemical engineering in practice*, John Wiley & Sons, 2011.
55. A. Lawal and D. Qian, US, 2008.
56. W. D. Bennett, P. M. Martin, D. W. Matson, G. L. Roberts, D. C. Stewart, A. Y. Tonkovich, J. L. Zilka, S. C. Schmitt and T. M. Werner, Google Patents, US, 2002.

57. D. Fernandez Rivas, A. Prosperetti, A. G. Zijlstra, D. Lohse and H. J. G. E. Gardeniers, *Angewandte Chemie International Edition*, 2010, **49**, 9699-9701.
58. B. Verhaagen, Y. Liu, A. G. Pérez, E. Castro-Hernandez and D. Fernandez Rivas, *ChemistrySelect*, 2016, **1**, 136-139.
59. G. Chisholm, P. J. Kitson, N. D. Kirkaldy, L. G. Bloor and L. Cronin, *Energy & Environmental Science*, 2014, **7**, 3026-3032.
60. M. Vaezi, H. Seitz and S. Yang, *The International Journal of Advanced Manufacturing Technology*, 2013, **67**, 1721-1754.
61. A. K. Au, N. Bhattacharjee, L. F. Horowitz, T. C. Chang and A. Folch, *Lab on a Chip*, 2015, **15**, 1934-1941.
62. N. Bhattacharjee, A. Urrios, S. Kang and A. Folch, *Lab on a Chip*, 2016, **16**, 1720-1742.
63. A. K. Au, W. Huynh, L. F. Horowitz and A. Folch, *Angewandte Chemie International Edition*, 2016, **55**, 3862-3881.
64. N. Independent Review Panel, ed. U. S. D. o. E. H. Program, 2009.
65. B. D. James and J. A. Kalinoski, in *Status Presentation for Independent Review of the 2008 Cost Estimates*, Directed Technologies Inc, 2008.

Chapter 3

Mass transport aspects of water electrolysis

The transition to a world driven by clean and renewable energy sources would rely on our ability to develop and implement energy storage technologies. To this end, high efficiency electrochemical energy conversion devices will play a key role as they have the potential to buffer the fluctuation inherent to renewable energy generation from solar and wind resources. The performance of these devices depends on the balance of complex processes that range from the atomic scale all the way up to the macroscale. While molecular processes drive the electrochemical transformations that determine the energy storage potential of the devices, transport phenomena are responsible for the limitations that prevent devices to operate at the maximum possible efficiencies. Therefore, electrochemical cells and reactors need to be designed in suitable dimensions to facilitate the transport of reactants, products, and charged intermediates to and from the electrochemical reaction sites.

3.1 Introduction

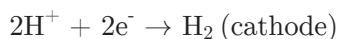
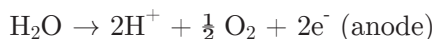
In this chapter, the transport phenomena inside electrochemical reactors are briefly reviewed to better understand the sources of the losses and, as a result, identify the potential pathways for development of deployable devices. Water splitting is selected as a model reaction. In addition to relevance to the dissertation topic, there are two main reasons that make water electrolysis an appropriate model system: (a) industrial relevance of the process, (b) most of the industrial electrochemical processes involve a hydrogen evolution or oxygen evolution reaction over one of their electrodes.

The electrochemical reactions happen at the interface between either a semiconductor or a catalyst and the electrolyte. In the electrolyte region close to this interface, transport processes of reactants, ions and products will take place within a mass transport boundary layer. Mass transport of all species will also occur within the bulk electrolyte which can be either a liquid electrolyte or a solid-state ion-conducting membrane.

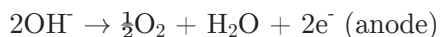
3.2 Processes in the boundary layer

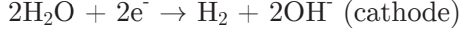
The boundary layer is defined as the region of the electrochemical cell in close proximity to the catalytic surfaces where important concentration or velocity gradients can evolve. The boundary layer is bounded by the hydrogen or oxygen evolutions reactions sites (HER and OER respectively) and the bulk electrolyte. Within this section we will briefly describe the factors that define the electrocatalytic rates observed at the surface of the electrodes, the formation and structure of the electrical double layer at the interface between the semiconductor or catalyst (metal or insulator) and the electrolyte, and how the reaction kinetics will affect the characteristics of the boundary layers of systems operated under liquid or solid-state electrolytes. Figure 3.1 shows a diagram of all the processes involved in this region

Electrode reactions. For electrolysis apparatus, the half-reactions that take place on the surface of the semiconductor or the heterogeneous electrocatalyst can be written as:



in acidic electrolytes, or





under basic conditions. For metal-electrolyte and approximatively also semiconductor-electrolyte interfaces, a generalized Butler-Volmer expression can closely describe the rate of each of these reactions,

$$j = j_0 \left[\left(\frac{c_{\text{red},\text{surf}}}{c_{\text{red},\text{bulk}}} \right)^{\gamma_1} \exp\left(\frac{\alpha_a F \eta}{RT}\right) - \left(\frac{c_{\text{ox},\text{surf}}}{c_{\text{ox},\text{bulk}}} \right)^{\gamma_2} \exp\left(-\frac{\alpha_c F \eta}{RT}\right) \right] \hat{n} \quad (1)$$

where j is the current density (positive for anodic currents) in the direction, \hat{n} , normal to the electrode surface. j_0 is the exchange current density, α_a and α_c are the apparent transfer coefficients for the anodic and cathodic reactions, and η is the electrode surface overpotential¹. c_{surf} and c_{bulk} correspond to the surface and bulk concentration of species involved in the cathodic reaction (red) or the anodic reaction (ox). The contribution of these concentration terms are determined by the exponents γ_1 and γ_2 .

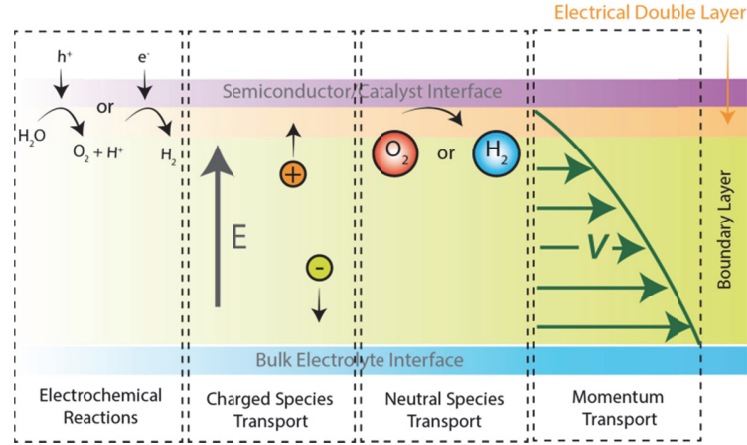


Figure 3.1. Diagram of processes involved in the boundary layer. Electrochemical reactions take place at the interface with the catalyst or semiconductor, neutral and charged species migrate and diffuse across the boundary layer, and a velocity gradient evolves from the interface.

The parameters that define the current levels (j_0 and a) are strongly dependent on material properties, surface treatments, and solution composition. Commercial water splitting systems that operate under acidic environments often implement electrocatalysts based on Platinum (Pt) and Iridium oxide (IrO_x) for the HER and OER respectively, while their alkaline counterparts use Nickel based catalysts. Significant research efforts have been devoted to develop novel catalysts with the aim of improving the efficiency of the state-of-the-art materials, or to identify earth-abundant substitutes to the Pt or IrO_x -based catalysts. Multiple reports in the literature have covered the developments of this field²⁻⁷, and some efforts have been devoted to benchmark the performance of materials under comparable operating conditions^{8, 9}. These efforts are of great value to the

development of hydrogen generators, as the unifying metrics measured for various electrocatalyst systems can directly aid in the design of practical devices.

The electrical double layer. The electrical double layer describes two charged regions in close vicinity of the electrode surface, usually in a dimensional-scale of several nanometers (Figure 3.2). Assuming ideally polarizable electrodes, the layers evolve as a result of specific adsorption of solvent molecules or ions species on the electrode with resulting bond formation, and electrostatic attraction due to an applied potential in the electrode. These two effects result in a polarized layer close to the surface with a thickness in the range of Angstroms (typical radius of adsorbed ions). This layer is composed of the adsorbed molecules and ions (also called inner Helmholtz layer), and solvated ions with the counter-charge of the surface (building the outer Helmholtz layer). Next to the Helmholtz layer there is a layer composed of solvated anions and cations, with the net electrical charge equals to the sum of the surface charge of the electrode and the charge of the Helmholtz layer. This outer layer, also called diffuse layer, is loosely attracted to the charge interface as a result of long-range forces (electrostatic forces) and exhibits an extended dimension. The thickness of the diffuse layer is a function of the electrolyte properties only, namely its bulk concentration, its relative permittivity, ion charges, and temperature. The Debye length can be used to estimate the thickness of the diffuse layer, which is usually in a range of several nm. This is in contrast to the liquid electrolyte boundary layer resulting from the no-slip boundary condition and the corresponding fluid flow distribution (discussed in the next section), which is electrically neutral and spans a significantly larger area, usually in the range of micrometers to millimeters.

Historically, the electrical double layer has been described by Helmholtz, reformulated by Gouy-Chapman, combined by Stern, and further detailed by Graham^{10, 11}. The Helmholtz and the diffuse layers can be represented as two capacitors in series. For large electrolyte concentrations, the total capacitance is dominated by the capacitance in the Helmholtz layer and so is the potential drop over the double layer. These conditions can be used in experimental investigations in order to simplify the interpretation of the data.

In contrast to metal electrodes, the carrier density in semiconductor is much smaller, resulting in a distribution of the surface charge over a finite depth, i.e. the space charge layer. The electrical double layer is affected by this space charge layer and eventually the potential drop over the interface is influenced by the three layers in series: the space charge layer in the semiconductor, the Helmholtz layer, and the diffuse layer. The potential drop distribution across the three layers is dependent on the materials and operating conditions.

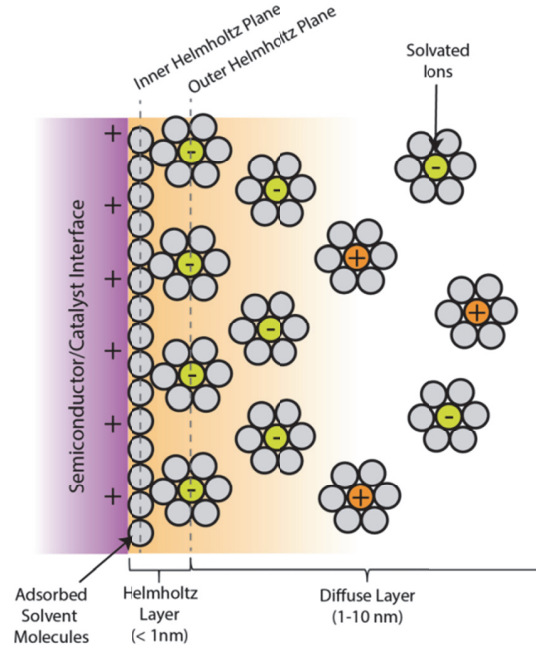


Figure 3.2. Schematic representation of the electrical double layer. The positive (+) and negative (-) species represent solvated ions which compose the Helmholtz layer as well as the diffuse layer.

The double layer affects phenomena such as charge transport in small scale structures (nano- to micron-scale)¹², and electrophoretic or electroosmotic effects¹³. The electrical double layer can also be used to probe the nanorheology of the solvent and ion system at the charged surface¹⁴. In (photo)electrochemical applications, the double layer affects the amount of current used in the electrochemical reaction as it acts as a capacitor in parallel with the surface reaction¹:

$$\mathbf{j} \cdot \hat{\mathbf{n}} = f(\eta, c_i) + C \frac{d\eta}{dt} \quad (2)$$

where f is the function describing the electrode kinetics, C is the capacity of the double layer, and c_i the species concentration in the bulk. The actual current used for the charging and discharging of the double layer depends heavily on the applied potential, the frequency or alternation of the current (e.g. resulting from transient solar irradiation), the interface characteristics (electrode material, surface roughness), and the electrolyte composition. Additionally, the microscopic architecture of the double layer affects the details of the charge transfer to the surface and the elementary steps of the electrode kinetics. A semi-empirical correction to eq. 2 consist of adapting the concentration from the bulk concentration to the concentration at the interface between the Helmholtz and diffuse layer, and reducing the overpotential by the potential drop in the Helmholtz layer¹.

Novel insights on the structure of and charge transport within the double layer and its effect on charge transport to and from the surfaces and its influence on the surface kinetics have been provided by the utilization of detailed molecular dynamics simulations¹⁵.

Liquid electrolyte boundary layers. While the electrical double layer describes the first few nanometers of the interface between the electrolyte and the reaction sites, there is a much larger region in close proximity with this interface where the properties of the electrolyte (i.e. momentum and composition) are not uniform – the mass transport boundary layer. Its thickness (δ_c) can be best estimated using dimensionless numbers such as the Sherwood number, $Sh = k\delta_c/D$, which relates the mass transfer coefficient (k) for species' transport from the bulk to the surface or vice versa with their diffusion coefficient (D). The Sherwood number is usually given as a function of Reynolds number, $Re = xu_0\rho/\mu$, and Schmidt number, $Sc = \mu/(\rho D)$, where x is a characteristic system dimension, u_0 the average linear velocity of the fluid, ρ its density and μ its kinematic viscosity. The actual functional dependence will vary according to the flow field and the configuration. For the simple case of a laminar flow parallel to a flat plate, the estimation of the mass transport coefficient and the typical boundary layer thickness along the plane direction x is given by¹⁶,

$$\frac{\delta_c}{x} = 4.64 \times Re^{-1/2} Sc^{-1/3} \quad (3)$$

For different flow geometries similar expressions can be derived, but the exponents modifying the Re and Sc numbers will vary, as well as the proportionality constant¹⁷.

In electrochemical water splitting devices, the boundary layer will determine the extent of the mass transport limitations and ultimately the device performance. These limitations are best mitigated when devices are operated under strong acidic or basic electrolytes. Under these conditions, the transport of intermediate species (H^+ or OH^-) is not limiting, the electrode reactions occur at a higher rate, and the formation of ionic concentration gradients are minimized. Despite these advantages, only a few electrocatalytic or photoelectrocatalytic materials are stable under these highly corrosive electrolytes. Operating water splitting devices at moderate pH conditions in buffered electrolytes or supporting electrolytes can enhance the materials' stability to a limited extent. When buffered liquid electrolytes are used, the transport of charged species becomes complex. During operation, H^+ ions are produced in the surface of the anode while they are consumed at the cathode. This leads to the formation of a depletion zone at the vicinity of the cathode and an accumulation one in the anode. As the concentration of H^+ or OH^- ions is low in the buffered electrolyte, a pH gradient

will evolve from the surface of the electrodes and a large portion of the current in the system will be carried by supporting ions. This in turn will result in the formation of further concentration gradients of supporting ions at the surface of electrodes, building up adverse potentials in the cell. These phenomena can significantly affect the cell current density at a given potential by imposing concentration polarization (CP) losses¹⁸. The extent of these losses can be assessed by balancing all the ionic transport processes occurring in the electrochemical cell (i.e. migration, diffusion and convection):

$$\mathbf{j} = -F^2 \nabla \phi \sum_i z_i^2 u_i c_i - F \sum_i z_i D_i \nabla c_i + F \mathbf{u} \sum_i z_i c_i \quad (4)$$

where F , z_i , u_i , c_i , D_i , and, u are the Faraday's constant, species charge, mobility, concentration, diffusivity and electrolyte's velocity profile, respectively. The last (convection) term in the expression can be set to zero due to the electroneutrality condition. This expression is valid for dilute electrolytes, and it can take more complex forms in concentrated solutions. It is often convenient to define the conductivity of the electrolyte, κ , as,

$$\kappa = F^2 \sum_i z_i^2 u_i c_i \quad (5)$$

and the potential losses in the systems as,

$$\nabla \phi = -\frac{j}{\kappa} - \frac{F}{\kappa} \sum_i z_i D_i \nabla c_i \quad (6)$$

where the second term, the diffusion potential, directly describes the CP losses in the cell. As significant concentration gradients form at the surface of the electrodes, larger potentials will be required to achieve a given current density. It is also important to clarify that κ is not necessarily uniform through the electrochemical cell, and that the gradients formed will lead to variations in conductivity across the electrolyte. At the limit, if ions are depleted in a particular region of the cell, the conductivity will tend to zero. Thus, for the device to operate at practical current densities (i.e. $> 10 \text{ mA cm}^{-2}$), the concentration difference across the boundary layer should remain small. Analytical expressions for concentration profiles and resultant losses have been provided in a theoretical study¹⁹. Another consequence of the large difference between the H^+ or OH^- concentration at the surface of electrodes and the bulk electrolyte is the appearance of a highly corrosive medium in contact with the surface of the electrode materials. This is specifically important since in many cases buffered electrolytes are used to provide higher levels of flexibility over the catalyst selection.

Due to the problems referred above, several groups have started to implement techniques to probe the ionic concentrations and subsequent losses at the surface of electrodes²⁰. Scanning electrochemical microscopy (SECM)²¹ is a well stab-

lished and versatile method capable of providing three dimensional pH maps close to the electrodes with submicron resolution^{22, 23}. It can also help to elucidate transient and steady state hydrogen evolution rates²⁴. Apart from SECM, non-intrusive confocal fluorescent microscopy methods with pH sensitive dyes can be used to probe the pH variations in three dimensions close to the catalyst²⁵. Additionally, some efforts have focussed on mitigating the CP losses around the boundary layer by implementing device engineering solutions. Recently, some studies have proposed the use of fast flow rates (forced convection) of liquid electrolytes in microfluidic channels to minimize the adverse effects of ion concentrations²⁶. By increasing the convective transport near the electrodes, the size of the boundary layer can be reduced and the transport of ionic species enhanced. Under these conditions, the concentration gradients near the electrodes can be significantly reduced. A recent study has also shown that bubble-induced mixing near the surface of the electrodes can reduce the transport losses to less than 25 mV at 10 mA cm⁻². In the contrary, a stagnant cell had limiting currents below 3 mA cm⁻²¹⁸.

Although the convective mixing due to the growth and movement of bubbles can be beneficial for the minimization of concentration losses, the presence of bubbles can have detrimental effects for a solar-hydrogen device. The bubbles can increase the reaction kinetic losses if they are not released rapidly from the catalyst surface. Moreover, in integrated photoelectrochemical (PEC) devices, they can affect the light absorption in the semiconductor by inducing undesirable scattering and reflections. Few methods have been employed to relax these adverse effects. In an early example²⁷, 0.01 M of the surfactant Triton X-100 was added to the electrolyte in order to reduce the size of bubbles and encourage faster detachments. In a fully integrated PEC device²⁸, a louvered architecture has been implemented to address the bubble related challenges. The photoanode and photocathode are placed at tilt angles with respect to two horizontal axes, so that the evolved gases could move towards devised outlets after sufficient growth. Apart from these notable examples, most of the demonstrated solar-hydrogen devices place electrodes vertically in an electrolyte and do not investigate the limitations that bubble transport imposes on these systems²⁹⁻³⁹. In these cases, the devices rely on the upward movement of bubbles due to buoyant forces towards collection sites. In a deployable integrated solar-fuel generator, this configuration will pose significant challenges, as the photoabsorber will need to be placed normal to solar irradiation direction. Moving forward, electrochemical system designs that can mitigate the transport challenges described above can have a strong impact in the development of solar-hydrogen devices.

Solid electrolyte boundary layers. When devices are operated with pure water or vapor, solid-state ion conductors are required to allow for ion-transport between the electrodes^{40, 41}. Under these circumstances the interfacial layer of the ionomer that covers the catalyst surface plays a very important role in defining the overall device performance. Mainly, this ionomer layer needs to allow for fast water, gas and ion transport between the surfaces of the catalyst into the bulk region of the device. These interfacial processes are critical in the catalyst layers of membrane electrode assemblies in water electrolyzers. In these systems, pure water is fed into the surface of catalysts layers, which are composed of blends of carbon particles (providing electrical conductivity), catalyst nanoparticles and ionomers such as Nafion (Figure 3.3). Within the catalyst layers, water diffuses through the ionomer film onto the catalyst surface where the water oxidation or proton reduction reactions take place. Then protons migrate across thin ionomer films into the bulk membrane, while the evolved gases diffuse through the ionomer layer towards collection ports^{42, 43}. The overall morphology of the catalyst layer plays a key role, as mesoscale porosity is desired to alleviate mass transport limitations. Within state-of-the-art catalyst layers water and gases can readily flow across the porous structure, while they diffuse slowly through the ionomer films covering the catalyst particles. These ionomer films usually have thicknesses in the order of 10 nm which facilitates fast transport of species. In an effort to further improve the current throughput in catalyst layers, some research groups have started to develop high-surface area catalyst layers by templating electrocatalysts into microwire arrays^{44, 45}. These rationally designed structures have led to catalyst layers that can operate stably at current densities of several A cm^{-2} .

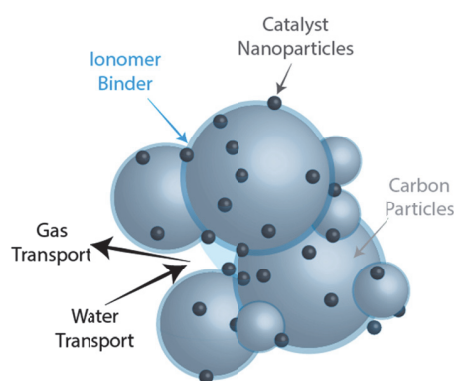


Figure 3.3. Schematic representation of state-of-the-art catalyst layer describing the blend between conducting carbon particles, catalytic nanoparticles and ionomer binder. Water diffuses fast through the porous structure and into the ionomer thin-film towards the catalyst particles. The evolved gases will then diffuse through the ionomer films and transport out of the catalyst layer towards collection ports.

3.3 Processes in bulk liquid electrolytes

The bulk liquid electrolyte is defined as the region of the device far from the electrode surface where the concentration of species can be considered to be approximately uniform. The bulk electrolyte is bounded by the boundary layers of the anode and/or cathode, and possibly a solid-electrolyte membrane. In a hydrogen generator, this region can be simple or compound. In a compound electrolyte, the ionic transport takes place in a combination of a separator and a supporting liquid electrolyte^{46, 47}. In general, the transport of species through the bulk electrolyte needs to satisfy two conditions: (i) deliver the product gases to independent collection ports with minimum levels of cross-contamination and (ii) provide a low-resistance pathway for ionic transport across the electrodes (Figure 3.4). To satisfy the first conditions, devices are designed so that H_2 fuel is supersaturated in the electrolyte and collected in the gas phase at independent ports. Membranes are commonly proposed to avoid undesirable levels of crossover. To reduce the ionic resistance of the system, the design of the device should minimize the interelectrode distance and incorporate electrolytes with high conductivities. Strong acid or base electrolytes have high conductivities and their use avoid the formation of large concentration gradients.

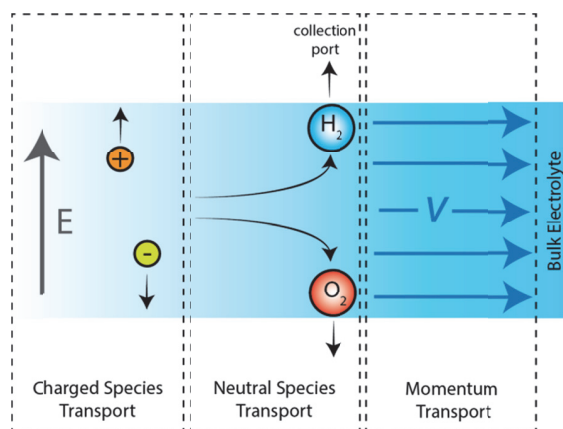


Figure 3.4. Diagram of processes involved in the bulk electrolyte. Ions migrate between electrodes, products are transported towards collections sites by convection and diffusion, and convective flows can be used to mitigate transport limitations.

As mentioned in the previous section, some materials stability constraints can be mitigated to some extent by operating devices under moderate pH buffered electrolytes. As the concentration of OH^- and/or H^+ is low in buffered electrolytes, a significant fraction of the current in the system will be carried by supporting ions. When supporting electrolytes are used in membrane-separated systems, the bulk electrolyte in either side of the membrane can reach significantly different compositions, leading to CP losses as the ones observed in the electrode

boundary layer. Several methods have been developed to address this challenge. Potentiometric measurements of buffered electrolytes in cells constructed with anion and cation exchange membranes suggest that the use of large volumes of electrolytes per unit electrode area can prevent depletion of the buffer capacity⁴⁸. This method however, increases the size of the system which can hinder large scale deployment. Employing circulatory convective streams between the HER and OER compartments is another solution that can relax the concentration gradients problem without the need for utilization of large volumes of electrolytes⁴⁹. The drawback is that by introducing recirculating streams, product crossover is also enhanced which affects the purity of the hydrogen fuel produced. This constrains the range of recirculating flowrates that can be implemented before the concentration of O₂ in the fuel stream reaches levels above the flammability limit. Another promising solution involves the employment of microfluidic approaches to reduce the volume of electrolyte, avoid the formation of large concentration gradients, and reduce the pathlengths for ion transport; overall reducing the cell overpotential. This is achieved by operating devices under electrolyte streams at high flow rates so that the boundary layer thickness is minimized. Although previous studies have shown effective, safe and robust production of oxygen-free hydrogen streams^{26,46}, employing these principles in large-scale prototypes has yet to be demonstrated.

To better understand the transport processes that occur in the bulk electrolyte it is useful to describe the physical processes using the governing transport equations. Below, we describe these equations for conservation and transport of chemical species coupled to the Navier-Stokes equations through a convective term⁵⁰.

The steady state mass conservation equation for charged or neutral species is given by,

$$-\nabla \cdot \mathbf{N}_i + r_i = 0 \quad (7)$$

Here \mathbf{N}_i is the molar flux vector and r_i is a bulk reaction source term. Similar to eq. 4, the molar flux is given by,

$$\mathbf{N}_i = -z_i u_{i,e} F \nabla \phi_l - D_{i,e} \nabla c_i + \mathbf{u} c_i \quad (8)$$

where z_i , $u_{i,e}$, F , ϕ_l , $D_{i,e}$, c_i , and \mathbf{u} are the species valence, effective mobility, Faraday's constant, potential of the liquid phase, species effective diffusivity, concentration, and liquid velocity, respectively. The effective diffusivity and mobility of charged species can be related by Nernst-Einstein equation: $u_{i,e} = D_{i,e}/(RT)$. The velocity profile can be obtained through the steady mass and

momentum conservation (i.e. Navier-Stokes) equations for Newtonian and incompressible fluids,

$$\nabla \cdot \mathbf{u} = 0 \quad (9)$$

$$(\mathbf{u} \cdot \nabla) \mathbf{u} = -\frac{1}{\rho} \nabla p + \nu \nabla^2 \mathbf{u} \quad (10)$$

where ρ , p , and ν are density, pressure, and kinematic viscosity, respectively. If a porous separator is used in the device, eq. 10 can be modified for the porous region following a Darcy's model for porous medium,

$$\left(\frac{\langle \mathbf{u} \rangle}{\epsilon} \cdot \nabla \right) \frac{\langle \mathbf{u} \rangle}{\epsilon} = -\frac{1}{\rho} \nabla p + \frac{\nu}{\epsilon} \nabla^2 \langle \mathbf{u} \rangle - \frac{\nu}{K} \langle \mathbf{u} \rangle \quad (11)$$

where ϵ and K are porosity and permeability of the fluid through the separator. In this case, $\langle \mathbf{u} \rangle$ is the superficial velocity vector: an equivalent velocity field that allows for the treatment of the flow as if it was confined to a one-phase media. The last term on the right side is added to account for viscous losses in the porous separator, relevant for low velocity flows. In the case of a uniform liquid electrolyte, this equation reduces to eq. 10 as porosity tends to unity, permeability to infinity, and superficial velocity is replaced by the actual fluid velocity, \mathbf{u} . In all equations presented above, isotropic properties such as diffusivity, porosity, and permeability are assumed. By solving this set of equations, all important operational parameters can be estimated: overpotentials, product crossover, concentration, and velocity profiles⁵⁰.

3.4 Processes in solid electrolyte membranes

The safe operation of water splitting devices requires that the produced gas streams have compositions below the flammability limit ($<4\%$ v/v of O_2 in H_2)^{51, 52}. Despite some notable exceptions, the co-evolution of H_2 and O_2 in a common electrolyte will usually lead to unsustainable levels of gas crossover⁵³⁻⁵⁵. To counteract this issue, membranes can be included in between reaction sites so that ionic conduction can be maintained between the hydrogen evolution side and the oxygen evolution side, while at the same time gas permeation can be averted (Figure 3.5). These tasks are similar to those imposed in membranes used in fuel cell applications, although the ionic conduction and gas barrier requirements may differ. In general, the current density across the membrane depends on the material's conductivity, κ_{mem} , membrane thickness, L , and the ohmic potential drop across the membrane, $\nabla \phi_{mem}$,

$$\mathbf{j}_{mem} = \kappa_{mem} \nabla \phi_{mem} \quad (12)$$

The gas crossover can be expressed in terms of a current equivalent loss, j_{XO} , which depends on the gas permeability for H_2 or O_2 , ψ_{H_2} and ψ_{O_2} respectively, and the difference in partial pressures, p_{H_2/O_2} , between each side of the membrane,

$$j_{XO,H_2} = -n_{H_2} F \psi_{H_2} \nabla p_{H_2} \quad (13)$$

$$j_{XO,O_2} = n_{O_2} F \psi_{O_2} \nabla p_{O_2} \quad (14)$$

The values of j_{XO} can be used to estimate the losses in the electrodes arising from parasitic H_2 oxidation or O_2 reduction at the anode and cathode respectively, as it describes the current losses if all of the gas that back diffuses across the membrane is consumed at the electrodes. Furthermore, the ohmic and gas crossover energy losses can be derived as,

$$E_{ohm} = \frac{j^2 L}{\kappa} \quad (15)$$

$$E_{XO} = \sum_{i=H_2,O_2} |\psi_i \nabla p_i n_i F| E^0 \quad (16)$$

with E^0 being the standard potential for the water splitting reaction. These expressions describe the trade-off between the membrane ionic conduction and gas crossover encountered in membrane design. Moreover, they explicitly describe the factors that define the optimal membrane thickness, L_{op} , which results into minimal energy losses.

$$L_{op} = \left(\frac{F E^0}{j^2} \kappa \sum_{i=H_2,O_2} |\psi_i \Delta p_i n_i| \right)^{\frac{1}{2}} \quad (17)$$

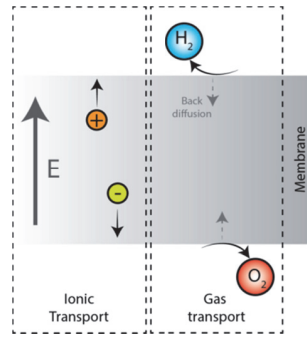


Figure 3.5. Diagram of processes involved in the membrane. The balance between ion and gas transport directly affects the overall device performance.

This expression can allow for an optimal membrane design given a set of device operating conditions. Also, this suggests that improved membrane materials should be designed so that the product between κ_{mem} and ψ is minimized.

3.5 Conclusions and Perspectives

Throughout this chapter, three critical regions were identified which interact with each other and ultimately define the device performance: the boundary layer, the bulk electrolyte, and the membrane. The boundary layer region is often overlooked, but a closer attention should be given to it as it generally defines the performance limitation of the devices. The transport processes within this region are dominated by diffusion of reactive or ionic species into and from the catalytic surface. Depending on the electrolyte composition this region can lead to diffusion limited current densities, especially if the device is operated under buffered electrolytes at moderate pH conditions. Whenever possible, devices should be operated under strong acidic or basic electrolytes. This would alleviate transport limitations and the formation of large concentration gradients in the boundary layer, as well as to accelerate the catalysis processes in the electrodes due to the increased concentration of reactive intermediates (H^+ or OH^-). On the other hand, it is well accepted that a large number of semiconductor or catalyst materials are not stable under these corrosive environments. In those cases, it is highly desirable to develop approaches where near-neutral buffered solutions are implemented as the electrolyte. These approaches should mitigate the formation of pH gradients around the surface the electrodes. Flow based systems are a promising alternative in these cases, as the introduced convection can be used to reduce the size of the diffusion boundary layer, and in this way accelerate the transport of H^+ or OH^- species. Research in this area can provide insights into the transport of multi-ion buffered electrochemical systems and could lead to the development of processes to operate solar-hydrogen generators under near-neutral conditions at high current densities. Some modelling efforts have started to analyze buffered systems under a set of limited conditions (i.e. passive systems, or flow systems at low Re numbers), providing important insights into the performance limits of devices operated at near-neutral pH¹⁸. Experimental and theoretical investigations that expand upon this area and are geared towards describing solutions to the pre-existing problems of buffered electrolyte systems could positively impact the solar-fuels field by enabling material systems that are only stable under mild pH conditions.

Critical transport processes in the bulk electrolyte involve the transport of ionic species between electrodes and gases from the evolution sites to collection ports. To avoid significant ionic resistance losses, the design of reactor architectures should minimize the ionic path-length. This is particularly important for devices that operate at high current densities ($> 100 \text{ mA cm}^{-2}$) as the potential losses in the electrolyte can account for 100's mV. It is also important to keep in mind, that flow systems, such as the ones implemented in commercial fuel cell or electrolysis units, can alleviate the mass transport limitations of devices and aid in

the collection of the fuel streams while mitigating gas crossover. To this end, stagnant cells or those where low flow rates are implemented will suffer from large gas back diffusion, and will most certainly require the implementation of membranes to avoid unallowable levels of oxygen contamination in the hydrogen fuel stream.

Bibliography

1. J. Newman and K. Thomas-Alyea, *Electrochemical Systems*, Wiley & Sons, 2004.
2. M. G. Walter, E. L. Warren, J. R. McKone, S. W. Boettcher, Q. Mi, E. A. Santori and N. S. Lewis, *Chemical reviews*, 2010, **110**, 6446-6473.
3. M. Gong and H. Dai, *Nano Research*, 2015, **8**, 23-39.
4. F. Safizadeh, E. Ghali and G. Houlachi, *International Journal of Hydrogen Energy*, 2015, **40**, 256-274.
5. M. Hamdani, R. N. Singh and P. Chartier, *International Journal of Electrochemical Science*, 2010, **5**, 556-577.
6. J. Lee, B. Jeong and J. D. Ocon, *Current Applied Physics*, 2013, **13**, 309-321.
7. J. Kibsgaard, C. Tsai, K. Chan, J. D. Benck, J. K. Norskov, F. Abild-Pedersen and T. F. Jaramillo, *Energy & Environmental Science*, 2015.
8. C. C. L. McCrory, S. Jung, J. C. Peters and T. F. Jaramillo, *Journal of the American Chemical Society*, 2013, **135**, 16977-16987.
9. C. C. McCrory, S. Jung, I. M. Ferrer, S. M. Chatman, J. C. Peters and T. F. Jaramillo, *Journal of the American Chemical Society*, 2015, **137**, 4347-4357.
10. Bockris, Conway and Yeager, *The double layer*, New York, 1980.
11. B. B. Damaskin and O. A. Petrii, *Journal of Solid State Electrochemistry*, 2011, **15**, 1317-1334.
12. D. A. Walker, B. Kowalczyk, M. O. de la Cruz and B. A. Grzybowski, *Nanoscale*, 2011, **3**, 1316-1344.
13. I. Llorente, S. Fajardo and J. M. Bastidas, *Journal of Solid State Electrochemistry*, 2014, **18**, 293-307.
14. L. Joly, C. Ybert, E. Trizac and L. Bocquet, *Physical Review Letters*, 2004, **93**, 257805.
15. C. D. Taylor and M. Neurock, *Current Opinion in Solid State and Materials Science*, 2005, **9**, 49-65.
16. Cussler, *Diffusion: Mass Transfer in Fluid Systems*, Cambridge, UK, 2003.
17. W. Deen, *Analysis of Transport Phenomena*, Oxford University Press, New York, 1998.
18. M. R. Singh, K. Papadantonakis, C. Xiang and N. S. Lewis, *Energy & Environmental Science*, 2015, **8**, 2760-2767.
19. N. Papageorgiou, M. Gratzel and P. P. Infelta, *Solar Energy Materials and Solar Cells*, 1996, **44**, 405-438.

20. D. V. Esposito, J. B. Baxter, J. John, N. Lewis, T. P. Moffat, T. Ogitsu, G. D. O'Neil, T. A. Pham, A. A. Talin, J. M. Velazquez and B. Wood, *Energy & Environmental Science*, 2015.
21. A. J. Bard and M. V. Mirkin, *Scanning electrochemical microscopy*, CRC Press, 2012.
22. B. R. Horrocks, M. V. Mirkin, D. T. Pierce, A. J. Bard, G. Nagy and K. Toth, *Analytical Chemistry*, 1993, **65**, 1213-1224.
23. M. Etienne, P. Dierkes, T. Erichsen, W. Schuhmann and I. Fritsch, *Electroanalysis*, 2007, **19**, 318-323.
24. Y. F. Yang and G. Denuault, *Journal of the Chemical Society-Faraday Transactions*, 1996, **92**, 3791-3798.
25. A. J. Leenheer and H. A. Atwater, *Journal of the Electrochemical Society*, 2012, **159**, H752-H757.
26. S. M. H. Hashemi, M. A. Modestino and D. Psaltis, *Energy & Environmental Science*, 2015, **8**, 2003-2009.
27. O. Khaselev and J. A. Turner, *Science*, 1998, **280**, 425-427.
28. K. Walczak, Y. K. Chen, C. Karp, J. W. Beeman, M. Shaner, J. Spurgeon, I. D. Sharp, X. Amashukeli, W. West, J. Jin, N. S. Lewis and C. X. Xiang, *Chemsuschem*, 2015, **8**, 544-551.
29. M. R. Shaner, J. R. McKone, H. B. Gray and N. S. Lewis, *Energy & Environmental Science*, 2015.
30. S. A. Bonke, M. Wiechen, D. R. MacFarlane and L. Spiccia, *Energy & Environmental Science*, 2015, **8**, 2791-2796.
31. C. Y. Lin, Y. H. Lai, D. Mersch and E. Reisner, *Chemical Science*, 2012, **3**, 3482-3487.
32. P. Bornoz, F. F. Abdi, S. D. Tilley, B. Dam, R. van de Krol, M. Graetzel and K. Sivula, *Journal of Physical Chemistry C*, 2014, **118**, 16959-16966.
33. J. S. Luo, J. H. Im, M. T. Mayer, M. Schreier, M. K. Nazeeruddin, N. G. Park, S. D. Tilley, H. J. Fan and M. Gratzel, *Science*, 2014, **345**, 1593-1596.
34. S. Y. Reece, J. A. Hamel, K. Sung, T. D. Jarvi, A. J. Esswein, J. J. H. Pijpers and D. G. Nocera, *Science*, 2011, **334**, 645-648.
35. C. R. Cox, J. Z. Lee, D. G. Nocera and T. Buonassisi, *Proceedings of the National Academy of Sciences of the United States of America*, 2014, **111**, 14057-14061.
36. J. H. Park, S. Kim and A. J. Bard, *Nano Letters*, 2006, **6**, 24-28.
37. C. Liu, J. Y. Tang, H. M. Chen, B. Liu and P. D. Yang, *Nano Letters*, 2013, **13**, 2989-2992.

38. J. Brillet, J. H. Yum, M. Cornuz, T. Hisatomi, R. Solarska, J. Augustynski, M. Graetzel and K. Sivula, *Nature Photonics*, 2012, **6**, 823-827.
39. F. F. Abdi, L. H. Han, A. H. M. Smets, M. Zeman, B. Dam and R. van de Krol, *Nature Communications*, 2013, **4**.
40. M. A. Modestino, M. Dumortier, M. Hashemi, S. Haussener, C. Moser and D. Psaltis, *Lab on a Chip*, 2015, **15**, 2287-2296.
41. J. M. Spurgeon and N. S. Lewis, *Energy & Environmental Science*, 2011, **4**, 2993-2998.
42. M. Carmo, D. L. Fritz, J. Mergel and D. Stolten, *International Journal of Hydrogen Energy*, 2013, **38**, 4901-4934.
43. T. Soboleva, K. Malek, Z. Xie, T. Navessin and S. Holdcroft, *Acs Applied Materials & Interfaces*, 2011, **3**, 1827-1837.
44. M. K. Debe, *ECS Transactions*, 2012, **45**, 47-68.
45. M. K. Debe, S. M. Maier-Hendricks, G. Vernstrom, J. Willey, M. Hamden, C. K. Mittelsteadt, C. Capuano, K. E. Ayers and E. Anderson, *ECS Meeting Abstracts*, 2011, **MA2011-02**, 694.
46. M. A. Modestino, C. A. Diaz-Botia, S. Haussener, R. Gomez-Sjoberg, J. W. Ager and R. A. Segalman, *Physical Chemistry Chemical Physics*, 2013, **15**, 7050-7054.
47. A. Dukic and M. Firak, *International Journal of Hydrogen Energy*, 2011, **36**, 7799-7806.
48. E. A. Hernandez-Pagan, N. M. Vargas-Barbosa, T. H. Wang, Y. X. Zhao, E. S. Smotkin and T. E. Mallouk, *Energy & Environmental Science*, 2012, **5**, 7582-7589.
49. M. A. Modestino, K. A. Walczak, A. Berger, C. M. Evans, S. Haussener, C. Koval, J. S. Newman, J. W. Ager and R. A. Segalman, *Energy & Environmental Science*, 2014, **7**, 297-301.
50. S. Haussener, C. X. Xiang, J. M. Spurgeon, S. Ardo, N. S. Lewis and A. Z. Weber, *Energy & Environmental Science*, 2012, **5**, 9922-9935.
51. H. F. Coward and Jones, *Limits of flammability of gases and vapors*, Bureau of Mines, Washington, DC, 1952.
52. H. Le, S. Nayak and M. S. Mannan, *Industrial & Engineering Chemistry Research*, 2012, **51**, 9396-9402.
53. J. Jin, K. Walczak, M. R. Singh, C. Karp, N. S. Lewis and C. Xiang, *Energy & Environmental Science*, 2014, **7**, 3371-3380.
54. A. Berger, M. Modestino and K. Walczak, 2013.
55. S. Haussener, C. Xiang, J. M. Spurgeon, S. Ardo, N. S. Lewis and A. Z. Weber, *Energy & Environmental Science*, 2012, **5**, 9922-9922.

Chapter 4

A micropillar array for sample concentration via in-plane evaporation

*We present a method to perform sample concentration within a lab-on-a-chip using a microfluidic structure which controls the liquid-gas interface through a micropillar array fabricated in PDMS between microfluidic channels. The microstructure confines the liquid flow and a thermal gradient is used to drive evaporation at the liquid-gas-interface. The evaporation occurs in-plane to the microfluidic device, allowing for precise control of the ambient environment. This method is demonstrated with a sample containing 1 μm , 100 nm fluorescent beads, and STYO-9 labelled *E. coli* bacteria. Over 100 seconds, the fluorescent beads and bacteria are concentrated by a factor of 10.*

4.1 Introduction

Sample concentration is a critical operation ubiquitous in lab-on-a-chip application due to the small volume of fluids and small concentration of samples¹. A variety of methods to concentrate samples have been developed using pressure driven flow via syringe pumps², electrophoresis³, dielectrophoretic⁴, centrifugal forces⁵, magnetophoresis⁶, optoelectronic⁷, capillary flow⁸, ion concentration polarization⁹ and evaporation-induced flow¹⁰. For evaporation-induced sample concentration, the fluidic flow is generally constant and the technique is applicable to any biological or chemical samples¹⁰. In this chapter, we focus on sample concentration via evaporation using a PDMS micropillar array adopting a technique developed for silicon microfluidic channels¹¹. We apply this technique to aqueous samples containing bacteria and fluorescent agents.

Membrane-based liquid-gas separation is a well-studied topic and has been reviewed extensively^{12,13,14,15}. These separations are used for adsorption, where gaseous phase is introduced into the liquids; stripping, where volatile components are removed from the liquid phase into the gas phase; and distillation, where miscible fluid mixtures are separated through vapor pressure and/or thermal differences. In this chapter, we focus on sample concentration as it applies to the lab-on-a-chip community where the samples are aqueous and the liquid flow is continuous.

Evaporation based microfluidic methods have been previously developed to perform sample concentration¹⁶⁻²⁷. These methods rely on controlling the evaporation at the outlet, replacing the vaporized liquid via capillary effects and sucking liquid through the microfluidic channel at pre-determined rates¹⁶. This evaporation rate can be actively controlled using pressure¹⁷ or temperature¹⁸. It can be used to manipulate blood¹⁹, bacteria²⁰, DNA²¹ and viruses²² or generate chemical gradients to perform chemotaxis experiments²³. Additionally, structures within microfluidic channels²⁴, open surface microchannel grooves²⁵, open-surface microtraps²⁶ and super-hydrophobic nano-structures²⁷ can be used to concentrate compounds at selective locations. Most of these methods rely on evaporation into an ambient atmosphere at the outlet of the microfluidic channel. Concentrating compounds via structures within microfluidic channels²⁴ can be highly advantageous since the fluids inside the channels can be rapidly modified.

Since evaporation is proportional to the surface area and also to the difference between the saturation and actual water vapor pressures near the surface of the liquid, we maintain a low water vapor pressure by having a thermal gradient between the water surface and the area where condensation takes place. In previous demonstrations, evaporation takes place from a large droplet at the outlet

of the microfluidic channel, with a heat sink placed at some distance away from the chip. Miniaturizing this system, such that evaporation occurs inside the microfluidic channel, can result in a dramatic decrease of the total vaporized rate if the total area remains about the same without changing the thermal gradient²⁸. Therefore, a goal of the microfluidic method is to increase both the: 1) surface area to volume ratio and 2) vapor pressure differentials via thermal gradients. These two components are an accepted advantage of microfluidics over traditional methods in energy applications²⁹, chemical synthesis³⁰, microreactors³¹, biosensors³², and medical diagnostics³³.

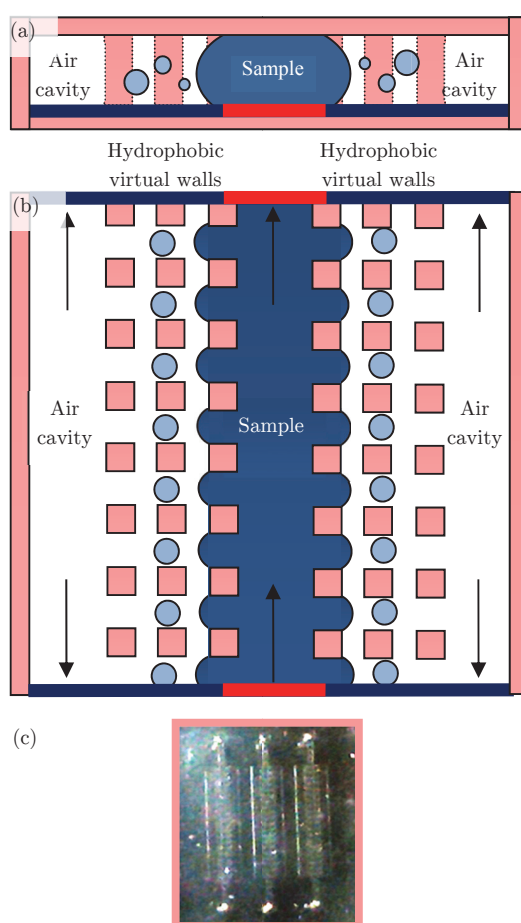


Figure 4.1. (a,b) Side-view and top-down diagram of liquid repellent structure. In the microfluidic chip, there is flowing sample which contains bacteria, particles and chemicals to be concentrated. The liquid repellent structure, between the sample channel and the air cavity, allows water vapor through but not liquid water. The air cavity fills up with vapor. The vapor can condense in the cavity or escapes to the outlet ports. (c) A picture of a 1 cm by 1 cm device, on a black background, with 3 parallel structures is shown.

The issue of generating a microstructure to separate liquid and gaseous phase within microfluidics is tackled by a variety of debubbling mechanisms. Unwant-

ed gas bubbles in microfluidic channels can be removed from continuous flow by open microfluidics³⁴ and various microstructures such as hydrophobic venting holes³⁵, pneumatic bubble traps³⁶, integrated bubble traps³⁷, membrane based debubblers³⁸, electrochemical debubblers³⁹ and in-plane debubblers⁴⁰.

Improved performance is obtained via external pressure and thermal integration⁴¹. Alternatively, these bubbles can be used as a means to valve fluidic flow⁴². We were inspired by micropillar liquid-gas separations¹¹, hydrophobic venting holes, and microfluidic debubblers to design a polymer-based microfluidic structure with micropillars, as shown in Figure 4.1.

4.2 Design Optimization

The microfluidic chip was made using polydimethylsiloxane (PDMS, Sylgard). PDMS was mixed at a ratio of 10:1 base and curing agent. This was poured onto a SU-8 mold for the PDMS fluidics layer, made using photolithography on a Si wafer. A flat PDMS layer was made using an empty Si wafer. After punching inlet and outlet ports into the PDMS fluidics layers, the two pieces of PDMS are brought together. It has an inlet sample microfluidic channel with a width of 800 μm . There are 100 μm by 100 μm openings in between posts of 100 μm by 100 μm (width and length). These posts form a part of the liquid repellent structure, which separates liquid water from vapor water. The air cavity is 500 μm wide. The total structure is approximately 2800 μm wide. The two microfluidic channels are driven by gravity pressure from water tanks.

First, we simulate the microfluidic chip containing the liquid repellent structure in COMSOL to optimize parameters. A 3-dimensional version of the chip as shown in Figure 4.1 is modelled in COMSOL. Fluid flows into the sample microfluidic channel. The sample is heated to 30°C. The fluid velocity in the sample microfluidic channel is dependent on the amount of vaporized water. The amount of vaporized water is determined by the difference of the saturated vapor pressure and the actual vapor pressure near the hot body of water. Proportional to this difference, heat in the form of the enthalpy of vaporization is removed from the sample-liquid repellent structure interface. When a heat sink condenses the water vapor, the vapor pressure decreases, heat is released in the form of enthalpy of condensation, and additional evaporation from the hot body of water can occur. To model the amount of water which is evaporating from the sample interface and condensing on the air cavity, we use the mass transfer equation as described by Plesset⁴³. Two bodies of water at different temperatures will have a mass flow of water which vaporizes from the hot body of water and condenses on the cold body of water, assuming salinity is equivalent. The equation is

$$J = \alpha \rho_0^e \sqrt{\frac{RT_0}{2\pi M}} \frac{1 - (\rho_V^e / \rho_0^e)(T_V / T_0)}{1 + \sqrt{T_V / T_0}}$$

where J is the mass flow rate, α is the evaporation coefficient, M is the molecular mass of the water, T_0 is the temperature at warmer interface, T_1 is the temperature at cooler interface, ρ_i^e is the saturation vapor density at T_i (i is either 0 or 1), and R is the universal gas constant.

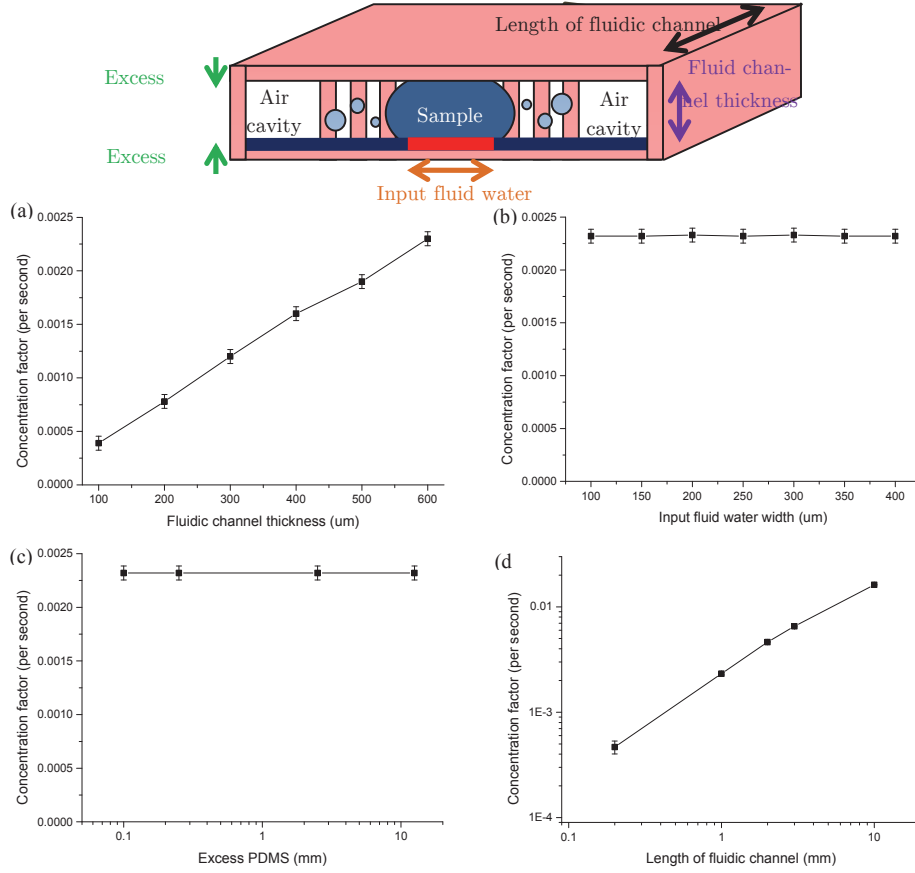


Figure 4.2. Optimizing parameters on the liquid repellent structure on a chip. Four parameters were optimized in COMSOL simulations: (a) fluidic channel thickness, (b) input fluidic water width, (c) excess PDMS and (d) length of fluidic channels. Thicker fluidic channels achieve higher total output, in an almost linear manner. However, thicker fluidic channels are difficult to fabricate as photolithography is generally limited to a 5:1 height to width ratio. There is indifference to the water width and excess PDMS thickness. Excess PDMS leads to higher material cost. Lastly, longer fluid channel lengths are preferred to shorter ones. Shorter lengths require more precise fluidic flow rates in experiments, otherwise, much of the energy is lost in the waste stream. Simulation error bars are due to meshing sensitivity.

In the simulations, we take the temperature along the sidewall of the sample microfluidic channel and the sidewall of the air cavity. After averaging in

height, we take the temperature and plug into the equation for a differential length-scale of $0.1 - 1 \mu m$, which is the smallest size of the simulation mesh. This energy is removed from the sample microfluidic channel and added to the sidewall of the air cavity. At steady-state, we sum up the total amount of water added per second in the air cavity. This is the amount of clean water generated or distillate output.

There are four parameters of the microfluidic chip which are varied in the simulation: microfluidic cavity depth, excess PDMS as insulator, microfluidic channel width and microfluidic channel length. As shown in Figure 4.2, the structure is indifferent to channel widths and excess PDMS. Optimal parameters were obtained for thicker cavities and longer channel lengths. Thicker excess PDMS leads to additional cost and longer channel lengths lead to more difficulty maintaining a proper hydrodynamic resistance ratio. Cavity and microfluidic channel thickness is limited by SU-8 mold fabrication and PDMS soft lithography to $400 \mu m$. There is no optimized value for the post dimension and it can be selected to meet the fabrication method's requirements such as photoresist's maximum deliverable aspect ratio. Distances between the posts are more important than the posts themselves since they decide the hydraulic resistance in the cross-flow direction. This resistance is directly proportional to the maximum allowable liquid backpressure. Therefore, the void dimension can be selected to tune the maximum achievable velocity of liquid in the sample channel.

With the optimal parameters determined by simulations for fluid channel thickness, fluid channel width, length of fluid channel and excess PDMS, we select a good system design for the liquid repellent structure and experimentally verify its stability and capability. In order to predict the maximum pressure flow that can be contained in the central channel, we use a similar method as in ref. [11] except, in our case, the material in the microfluidic channel is PDMS rather than silicon. Manipulating the height of the water tank allows us to modify the inlet pressure. We take images of the radius of curvature of the water-air interface at the sample microfluidic channel, as shown in Figure 4.3. The radius of curvature at the interface is determined by the Laplace-Young equation

$$\Delta P = \gamma \left(\frac{1}{R_x} + \frac{1}{R_y} \right)$$

where γ is surface tension, R_x and R_y are the radii of curvature and ΔP is the pressure difference between liquid and vapor phase. From the images, we obtain R_x . We can infer R_y from R_x . At a water tank height of $0 mm$, the radii of curvature R_x and R_y is ∞ since the pressure inside and outside the water is the same. As the water tank is raised in height, the radii of curvature decreases

since the pressure inside the water is higher than in the ambient air. When the water tank is increased to a maximum of 80 mm , the radius of curvature $R_x < 40\text{ }\mu\text{m}$ and the sample enters into the liquid repellent structure.

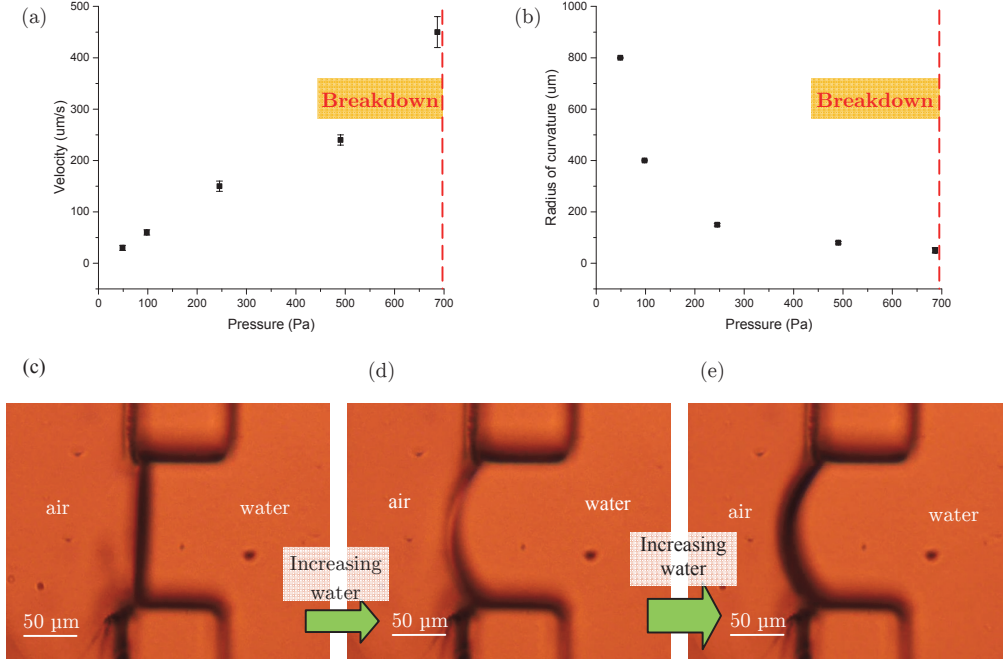


Figure 4.3. Graphs (a,b) and images (c,d,e) of water velocity and radius of curvature at the water-air interface as the water tank is changed in height experimentally. As the height is increased, the fluid flow velocity increases and the radii of curvature decreases. At some height, the liquid repellent structure does not prevent liquid water from entering into it, a condition we term, breakdown. We note that breakdown occurs at 80 mm of height for the water tank. Stable fluid flow is achieved for fluid velocity of $550\text{ }\mu\text{m/second}$ and a radius of curvature at $R_x \sim 40\text{ }\mu\text{m}$. This is equivalent to $0.2\text{ }\mu\text{L/second}$ for the 1 cm by 8 mm chip or 0.8 mL/hour per 1 cm^2 .

Second, we calculate the fluidic resistance of the liquid repellent structure. The hydraulic resistance⁴⁴ is determined by

$$R \approx \frac{12\mu L}{wh^3(1 - 0.630h/w)}$$

for a microfluidic channel with viscosity μ , height h , width w and length L where $h < w$. When $w < h$, one can switch the two variables. We assume a fixed fluid viscosity μ and height $h = 400\text{ }\mu\text{m}$ for all structures. The two variables are width w and length L . We assume that the fluid must travel from the inlet of the sample microfluidic channel to the outlet of the sample microfluidic channel without any connections between the sample microfluidic channel and the liquid repellent structure.

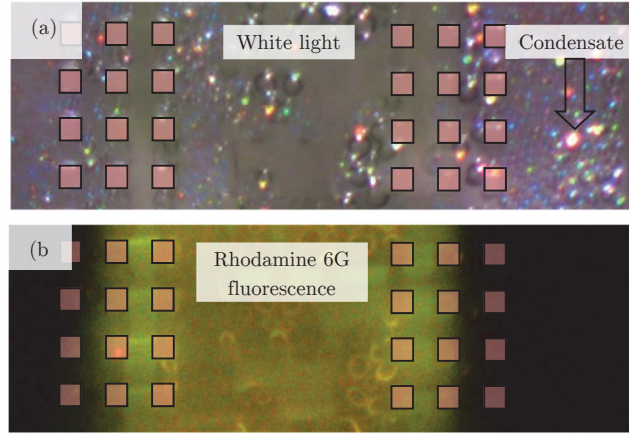


Figure 4.4. Experiment of fluorescence concentration using the liquid repellent structure on a chip with Rhodamine 6G contaminated water. A diagram of the liquid repellent structure is overlaid on the images (a,b). The Rhodamine 6G is visualized using a 514nm Argon laser. Rhodamine 6G containing contaminated water, pre-heated to 50°C, is flowing through the sample microfluidic channel. The liquid repellent structure separates the Rhodamine 6G contaminated water from the air cavity. Over time, condensate forms inside the air cavity, which we can see from the light scattering. There is clear separation of the Rhodamine 6G between the air cavity and sample channel.

An equivalent fluidic resistance circuit would be many cross-sections in series consisting of the sample microfluidic channel with width $w = 800 \mu\text{m}$ and length $L = 100 \mu\text{m}$ along with a side channel with width $w = 100 \mu\text{m}$ and length $L = 500 \mu\text{m}$, connecting from and to the microfluidic channel through the openings in the liquid repellent structure.

Therefore, the fluidic resistance of each parallel small structure is more than 2 orders of magnitude larger than the central fluidic channel. As such, one can expect to have about 100 small openings before the side openings have equivalent fluidic resistance to the sample microfluidic channel. If the openings are $100 \mu\text{m}$ wide, the sample microfluidic channel can be 1 cm long.

With these two parameters: a 75 mm high water tank and a 1 cm long sample microfluidic channel, we know the water pressure and hydrodynamic resistance. The fluidic flow rate is determined by:

$$\Delta P = R \times Q$$

where Q is the volumetric flow rate in the channel and R is the hydrodynamic resistance. Experimentally, the maximum average fluidic velocity is $550 \mu\text{m/second}$ at a radius of curvature at $40 \mu\text{m}$. This is equivalent to $0.2 \mu\text{L/second}$ for 1 cm by 8 mm chip or 0.8 mL/hour per 1 cm^2 .

With these additional calculations, the most practical design was chosen with depth at $400\ \mu\text{m}$, $1\ \text{cm}$ long microfluidic channel and air cavity, and $2 - 10\ \text{mm}$ total PDMS thickness. In the experiments, we characterized the liquid repellent structure by resolving the following questions: 1) Does the structure keep the liquid separated from the vapor, and 2) How good is the structure at concentrating samples?

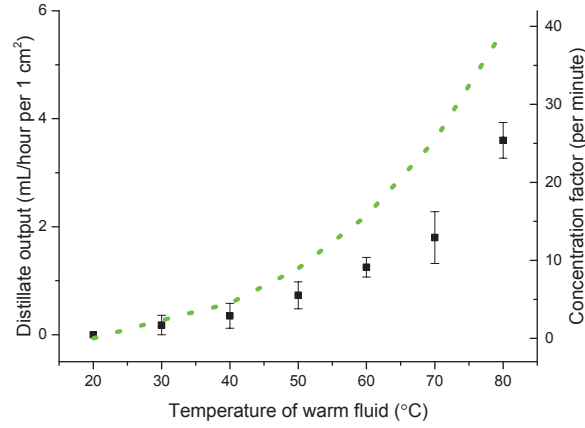


Figure 4.5. Comparison of experimental and simulation results of distillate output and concentration factor from the liquid repellent structure on a chip. Experiments were performed with the chip cooled to 20°C ; the body of water in the sample microfluidic channel was heated up to between 30°C to 80°C . Simulation results are shown in a dotted green line. Experimental results are plotted with error bars. The simulation output is higher than the experimental results. This factor comes about due to additional losses which were not considered in the simulation of the fluidic channels. For example, in actual experiments, there is additional heated fluid exiting the system as waste which is not all accounted for in the simulations.

4.3 Experimental Results

The liquid repellent structure on a chip is very adept at separating vapor and corresponding condensate from the sample in the microfluidic channel. To use the liquid repellent structure to concentrate samples, we modified the input sample temperature while keeping the chip cool. The chip was kept continuously at 20°C ; the body of water in the sample microfluidic channel was pre-heated. Figure 4.4 shows results with $50\ \mu\text{g/mL}$ Rhodamine 6G (Sigma Aldrich) contaminated water heated to 50°C , visualized with a $50\ \text{mW/cm}^2$ $514\ \text{nm}$ Argon ion laser. Rhodamine 6G containing contaminated water is flowing through the sample microfluidic channel. The liquid repellent structure separates the Rhodamine 6G contaminated water from the air cavity. Over time, condensate forms inside the air cavity, which we can see from the light scattering. There is clear separation of the Rhodamine 6G between the air cavity and sample channel as evidenced by the lack of fluorescence response in the region outside the

membrane. The vertical stripes in Figure 4.4b are an artefact due to the fluorescence filter.

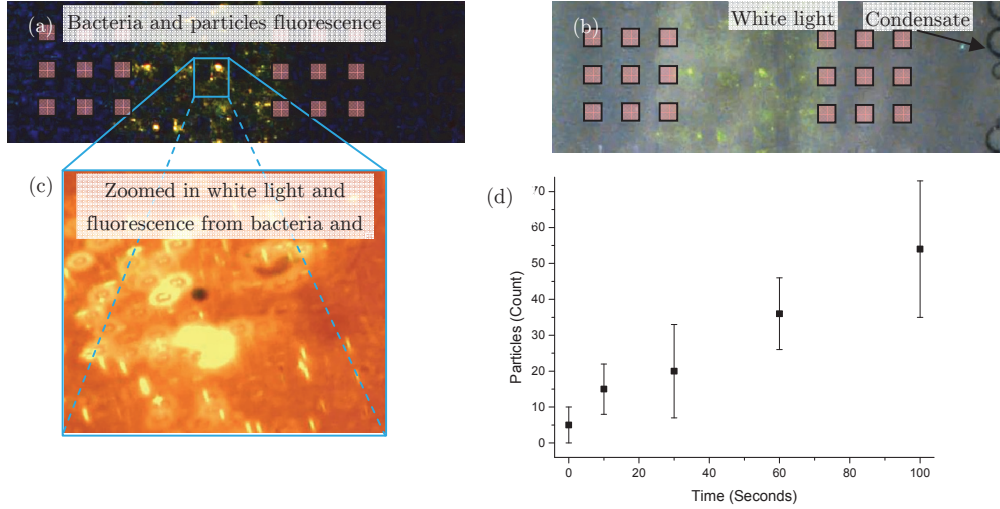


Figure 4.6. Experiment of particle concentration using the liquid repellent structure on a chip with SYTO9 labeled *E. coli*, green fluorescent 100nm and 1µm particles contaminated water. A diagram of the liquid repellent structure is overlaid on the images (a,b,c). The bacteria and particles are visualized using a 488 nm Argon laser. The contaminated water, pre-heated to 50°C, is inside the sample channel. The liquid repellent structure separates the contaminated water from the air cavity. There is clear separation of the bacteria and particles between the air cavity and sample channel. As we increase the magnification of the imaging system to get a better count of the number of bacteria and particles, most objects appear out-of-focus as the cavity depth is greater than the depth of focus. Therefore, we measure the total particle count by taking several images at different focal depths. We count the number of particles in the field of view as water evaporates over time in (d). There is a 10x concentration of the particles over 100 seconds, which is in agreement with simulation results.

To measure sample concentration capability with different pre-heating conditions, we measured the distillate output at different input temperatures. The chip was kept continuously at 20°C; the body of water in the sample microfluidic channel was pre-heated to between 30°C to 80°C. Due to the temperature difference and continuous flow of the pre-heated sample, continuous distillation occurs. At 30°C, we experimentally obtain 0.2 *mL/hour* per 1 *cm*²; at 80°C, we experimentally obtain 3.6 *mL/hour* per 1 *cm*². Simulations were performed with the same parameters as the experiment to quantify distillate output. At 30°C, we simulate a distillate output of 0.3 *mL/hour* per 1 *cm*²; at 80°C, we simulate a distillate output of 5.1 *mL/hour* per 1 *cm*².

A relationship between distillate output and concentration factor can be determined by the following formula:

$$C_{final} = C_{initial} \cdot \frac{V_{initial} + V_{distillate}}{V_{initial} + V_{waste}}$$

where $C_{initial}$ is the initial concentration of particles, C_{final} is the final concentration of particles, $V_{initial}$ is the initial volume inside the microfluidic channel, $V_{distillate}$ is the distillate output, and V_{waste} is the waste output from the central microfluidic channel.

As shown in Figure 4.5, there is general agreement on the curve although the simulation output is higher than the experimental results. This factor comes about due to additional losses which were not considered in the simulation of the fluidic channels. For example, in actual experiments $V_{waste} \neq 0$ and there is some heated fluid exiting the system in the outlet but in the simulations, we assume there is no exiting fluid and that $V_{waste} = 0$. Additionally, some energy is lost as the two bodies of water are quite far from each other and some water vapor may condense in the air cavity closer to the liquid repellent structure and farther away from the cavity walls.

We performed an experiment with fluorescent particles, as shown in Figure 4.6. The contaminated water, pre-heated to 50°C, contains $10^7/mL$ SYTO9 (Invitrogen) labeled E. coli K12 JM101 (Bioconcept), $10^7/mL$ yellow-green fluorescent 100 nm latex beads (Invitrogen) and $10^7/mL$ yellow-green fluorescent 1 μm latex beads (Invitrogen). The bacteria and particles are visualized using a 100 mW/cm² 488 nm Argon ion laser. The contaminated water is flowing through the sample channel. As before, the liquid repellent structure separates the contaminated water from the air cavity. The outlet is closed to prevent continuous flow. Over time, the particle concentration increases; the temperature in the sample microfluidic channel decreases until it is in equilibrium with the entire microfluidic chip. We see 10x concentration of the particles over 100 seconds.

4.4 Discussion

Experiments with evaporation-based concentration methods are limited by the ambient environment (i.e. humidity, room temperature, etc.)¹⁶. Control of the evaporating surface which determines the amount of evaporation, and the heat sink which removes the excess vapor, requires precise control of both the evaporating surface area and the thermal gradient. Although both concepts were demonstrated external to the microfluidic chip^{17,18,24}, we demonstrate the capability to control the two factors within the microfluidic chip to perform sample concentration. Experiments with open surface microchannel grooves²⁵ provide a very similar basis to compare against our results. With the hot body of water at 20°C, air velocity at $0.15 ms^{-1}$ and relative humidity at 50%, they are able to obtain 2% increase in particle concentration per 1 second with a 125 μm wide

and $80\text{ }\mu\text{m}$ deep channel. 50% relative humidity at 20°C is equivalent to saturated humidity at about 9°C . If we interpolate the data from our experiments, we are capable of experimentally obtaining 2% increase in sample concentration per 1 *second* by having the hot body of water at 28°C and the heat sink at 20°C . If one looks at the saturated vapor pressures for these two temperatures, the change in vapor pressure is very similar. Therefore, we obtain very similar results for sample concentration with an evaporation based microfluidic device in a much smaller footprint.

4.5 Conclusion

We have demonstrated using a liquid repellent structure to perform both distillation and evaporation based sample concentration in-plane inside a microfluidic chip. We demonstrate 3.6 mL/hour per 1 cm^2 distillate output using two bodies of water at 20°C and 80°C . Using the same structure, we demonstrate 10x concentration of fluorescent particles over 100 *seconds*. We anticipate the proposed microfluidic structure will enable novel applications in communicating microchannels within integrated lab-on-a-chip systems. The approach is lightweight, low cost and of low complexity.

Bibliography

- 1 P. Neuzil, S. Giselsbrecht, K. Lange, T.J. Huang and A. Manz, *Nature Reviews Drug Discovery*, 2012, **11**, 620-632.
- 2 A.C. Glavan, R.V. Martinez, E.J. Maxwell, A.B. Subramaniam, R.M.D. Nunes, S. Soh and G.M. Whitesides, *Lab on a Chip*, 2013, **13**, 2922-2930.
- 3 J.H. So and M.D. Dickey, *Lab on a Chip*, 2011, **11**, 905-911.
- 4 B. Mustin and B. Stoeber, *Lab on a Chip*, 2012, **12**, 4702-4708.
- 5 A.J. Mach, J.H. Kim, A. Arshi, S.C. Hur and D. Di Carlo, *Lab on a Chip*, 2011, **11**, 2827-2834.
- 6 D. Choudhury, X. Mo, C. Iliescu, L.L. Tan, W.H. Ton and H. Yu, *Biomeicrofluidics*, 2011, **5**, 022203.
- 7 R. Martinez-Duarte, *Electrophoresis*, 2012, **33**, 3110-3132.
- 8 M. Hitzbleck, L. Avrain, V. Smeken, R.D. Lovchik, P. Mertens and E. Delamarche, *Lab on a Chip*, 2012, **12**, 1972-1978.
- 9 K. N. Knust, D. Hlushkou, R.K. Anand, U. Tallarek and R. M., *Angewandte Chemie International Edition*, **52**, 8107-8110.
- 10 E. Berthier, J. Warrick, H. Yu and D.J. Beebe, *Lab on a Chip*, 2008, **8**, 860-864.
- 11 K.F. Lam, E. Cao, E. Sorensen and A. Gavriilidis, *Lab on a Chip*, 2011, **11**, 1311-1317.
- 12 K.F. Lam, E. Sorensen and A. Gavriilidis, *Chemical Engineering Research and Design*, 2013, **91**, 1941-1953.
- 13 K.F. Jensen, *Chemical Engineering Sciences*, 2001, **56**, 293-303.
- 14 V. Hessel, P. Angeli, A. Gavriilidis and H. Lowe, *Industrial and Engineering Chemistry Research*, 2005, **44**, 9750-9769.
- 15 A. Gunther and K.F. Jensen, *Lab on a Chip*, 2006, **6**, 1487-1503.
- 16 G.M. Walker and D.J. Beebe, *Lab on a Chip*, 2002, **2**, 57-61.
- 17 C.S. Effenhauser, H. Harttig and P. Kramer, *Biomedical Microdevices*, 2002, **4**, 27-32.
- 18 M. Zimmermann, S. Bentley, H. Schmid, P. Hunziker and E. Delamarche, *Lab on a Chip*, 2005, **5**, 1355-1359.
- 19 Y.H. Choi, S.S. Lee and K.H. Chung, *BioChip Journal*, 2010, **4**, 63-69.
- 20 J.Y. Zhang, J. Do, W.R. Premasiri, L.D. Ziegler and C.M. Klapperich, *Lab on a Chip*, 2010, **10**, 3265-3270.
- 21 Z.R. Xu, C.H. Zhong, Y.X. Guan, X.W. Chen, J.H. Wang and Z.L. Fang, *Lab on a Chip*, 2008, **8**, 1658-1663.
- 22 J.Y. Zhang, M. Mahalanabis, L. Liu, J. Chang, N.R. Pollock and C.M. Klapperich, *Diagnostics*, 2013, **3**, 155-169.
- 23 N.S. Lynn and D.S. Dandy, *Lab on a Chip*, 2009, **9**, 3422-3429.

- 24 X. Casadevall i Solvas, V. Turek, T. Prodromakis and J.B. Edel, *Lab on a Chip*, 2012, **12**, 4049-4054.
- 25 S. Kachel, Y. Zhou, P. Scharfer, C. Vrancic, W. Petrich and W. Schabel, *Lab on a Chip*, 2014, **14**, 771-778.
- 26 C.C. Wong, Y. Liu, K.Y. Wang and A.R.A. Rhaman, *Lab on a Chip*, 2013, **13**, 3663-3667.
- 27 F. de Angelis, F. Gentile, F. Mecarini, G. Das, M. Moretti, P. Candeloro, M.L. Coluccio, G. Cojoc, A. Accardo, C. Liberale, R.P. Zaccaria, G. Perozziello, L. Tirinato, A. Toma, G. Cuda, R. Cingolani and E. di Fabrizio, *Nature Photonics*, 2011, **5**, 682-687.
- 28 N.S. Lynn, C.S. Henry and D.S. Dandy, *Lab on a Chip*, 2009, **9**, 1780-1788.
- 29 D. Erickson, D. Sinton and D. Psaltis, *Nature Photonics*, 2011, **5**, 583-590.
- 30 K.S. Elvira, X. Casadevall i Solvas, R.C.R. Wootton and A.J. deMello, *Nature Chemistry*, 2013, **5**, 905-915.
- 31 J. Haber, M.N. Kashid, A. Renken and L. Kiwi-Minsker, *Industrial and Engineering Chemistry Research*, 2012, **51**, 1474-1489.
- 32 Y. Zhang, *International Symposium on Photonics and Optoelectronics*, 2012.
- 33 Y.F. Chen, L. Jiang, M. Mancuso, A. Jain, V. Oncescu and D. Erickson, *Nanoscale*, 2012, **4**, 4839-4857.
- 34 J. Melin, W. van der Wijngaart and G. Stemme, *Lab on a Chip*, 2005, **5**, 682-686.
- 35 D.D. Meng and C.J. Kim, *Lab on a Chip*, 2008, **8**, 958-968.
- 36 A.M. Skelley and J. Voldman, *Lab on a Chip*, 2008, **8**, 1733-1737.
- 37 W. Zheng, Z. Wang, W. Zhang and X. Jiang, *Lab on a Chip*, 2010, **10**, 2906-2910.
- 38 C. Liu, J.A. Thompson and H.H. Bau, *Lab on a Chip*, 2011, **11**, 1688-1693.
- 39 S. Harrer, S. Ahmed, A. Afzali-Ardakani, B. Luan, P.S. Waggoner, X. Shao, H. Peng, D.L. Goldfarb, G.J. Martyna, S.M. Rossenagel, L. Deligianni and G. Stolovitzky, *Langmuir*, 2010, **26**, 19191-19198.
- 40 C. Lochovsky, S. Yasotharan and A. Gunther, *Lab on a Chip*, 2012, **12**, 595-601.
- 41 J.M. Karlsson, M. Gazin, S. Laakso, T. Haraldsson, S. Malhotra-Kumar, M. Maki, H. Goossens and W. van der Wijngaart, *Lab on a Chip*, 2013, **13**, 4366-4373.
- 42 A. Oskooei, M. Abolhasani and A. Gunther, *Lab on a Chip*, 2013, **13**, 2519-2527.
- 43 M.S. Plesset, *Journal of Chemical Physics*, 1952, **20**, 790-793.

44 H. Bruss, *Theoretical microfluidics*, Oxford University Press, 2008.

Chapter 5

Solar Thermal Harvesting for Enhanced Photocatalytic Reactions

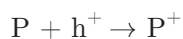
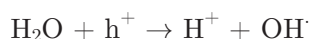
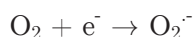
The Shockley-Queisser limit¹ predicts 30% maximum efficiency for single junction photovoltaic (PV) cells. The rest of the solar energy is lost as heat, reflection and transmission through the PV, and charge carriers recombination. In the case of photocatalysis, this maximum value is smaller since the charge carriers should be transferred to acceptor molecules rather than conductive electrodes. With this perspective, we realize that at least 70% of the solar energy is available to be converted into heat. This is specifically useful for photocatalysis, since heat can provide more kinetic energy to the reactants and increase the number of energetic collisions leading to the breakage of chemical bonds. Even in natural photosynthesis, at most 6%² of the solar spectrum is used to produce sugar and the rest of the absorbed photons are converted into heat in a process called transpiration. The role of this heating component is often overlooked; in this chapter, we demonstrate a coupled system of photothermal and photocatalytic decontamination of water by titania, the most widely used photocatalyst for various photo reactions. The enhancement over solely photocatalytic water decontamination is demonstrated to be 82% at 1X sun. Our findings suggest that the combination of photothermal solar energy capture with photocatalysis is a suitable strategy to utilize more of the solar spectrum and improve the overall performance.

5.1 Introduction

As the fossil fuel energy resources approach their limits, the quest for renewable alternatives is attracting more attention from the scientific and industrial communities³. Among these alternatives, the sun is the most promising source of energy⁴.

Solar energy is utilized in several ways which can be classified as direct and indirect. In direct utilization, the energy of the sun is not converted into other forms of energy such as electricity, but it directly drives a photochemical process such as water or air purification⁵⁻⁷. On the other hand, there are mechanisms to convert and store the solar energy to be consumed later. This energy storage can be electrical, as performed by photovoltaic panels⁸, or chemical⁹, as performed in solar reforming of liquid fuels¹⁰. Substantial studies are conducted to increase the efficiency of these processes. In case of single junction PV cells, the goal is to approach the 30% theoretical efficiency limit predicted by Shockley and Queisser¹ for a semiconductor with bandgap energy of 1.1 eV. The rest of the solar energy is wasted as heat, transmission/reflection, and recombination of charge carriers. For photocatalytic reactions such as water treatment or fuel reforming, there is no counterpart calculation that we are aware of. However, it can be claimed that this value should be smaller than 30%, since in these reactions, charge carriers should be transferred to acceptor molecules rather than conductive electrodes. The interacting molecules should be very close together so that the electron orbitals could overlap. Achieving this requirement is often very difficult when dealing with complex molecules. Therefore, at least 70% of the solar energy is available as heat which can be injected into the system to achieve faster reaction rates. It is worth noting that this discussion is valid for single band gap materials. If layered structures with concentrated sunlight are considered, this limit no longer holds. However, the price of such devices is very high at present and for many applications not economical.

Photocatalytic decomposition of organic pollutants in water has been investigated in many works since it is a low-cost and environmental friendly technology meeting the requirements of zero waste scheme in wastewater industry¹¹⁻¹⁵. In general, the dissociation of organic molecules can be summarized in the following chain reactions¹⁵:





In the above reactions e^- and h^+ are photo-generated charge carriers at the chemically active sites and P stands for the pollutant molecule. Several parameters such as catalyst loading, pH, temperature, dissolved oxygen, contaminants type and concentration, light intensity and wavelength affect this process's performance. Among these, temperature is the factor that we are going to deal with directly. It has been shown that the optimum temperature for pollutant dissociation over photocatalysts is in the range 20 to 80°C¹⁶. Above 80°C, the recombination of charge carriers becomes severe and below 20°C, the reaction's apparent activation energy increases. Therefore, as temperature increases, there is a trade-off between the charge carrier recombination and more favorable kinetics at reaction sites which can be realized from Arrhenius equation. The exact value of the optimum temperature depends on a number of factors such as type of photocatalyst, type and concentration of pollutants, etc. The existence of a favorable temperature range has been observed in other chemical photoreactions, for instance, ethylene oxidation¹⁷ where thermal enhancement is reported between 100 to 200°C.

Microfluidics offers new opportunities for chemists as the large surface to volume ratio is an advantage for catalytic reactions. In addition, if heat transfer is considered to speed up the reaction rate, going towards small scales is favorable, as more heat transfer area is available and thermal mass of the system decreases. Lower thermal mass means less required energy input and less initial warm-up time. If a photoreaction is considered, optimal design of the reactor using optofluidic techniques can lead to even higher efficiencies¹⁸. In light of these benefits, researchers have designed and studied optofluidics reactors for photocatalytic reactions. Lindstrom and Wootton¹⁹ achieved impressive loading of 66 gr of titania per reactant liter by coating the microreactor's walls with photocatalyst. They reported photodegradation rate of 10.6 % s⁻¹ for 0.1 mM solution of Methylene Blue (MB) at 12 µl min⁻¹ flow rate. Lei et al.²⁰ compared the performance of a planar optofluidics reactor with a bulk reactor and observed an enhancement of up to 100 times. In this chapter, we integrate a black absorbing layer to a planar reactor and convert the portion of the spectrum not used by the photocatalyst into heat. This enables us to put into test, the validity of above-mentioned discussion in practice. To our knowledge, this is the first time that sunlight is employed in a photocatalytic reactor as a shared source for both catalysis and heating.

5.2 Motivation

We have experimentally demonstrated titania based water treatment as the case study to demonstrate the benefits of incorporating solar thermal management in a photocatalytic reaction. After the pioneering work of Fujishima and Honda²¹, TiO_2 remains the most widely studied photocatalyst due to its photo stability, chemical inertness, and low price. On the other hand, there is a major problem with TiO_2 due to its large bandgap energy (~ 3.2 eV), meaning that it can only absorb in the UV region ($\lambda < 387$ nm). Figure 5.1 is based on solar spectra data from National Renewable Energy Lab and it illustrates that less than seven percent of the solar spectrum lies in the UV region (up to 400 nm) and the rest is not absorbed by TiO_2 ²². Huge efforts have been made to overcome this problem by bandgap engineering methods such as doping²³ or integration of other material like metallic nanoparticles in plasmonic photocatalysis²⁴. We offer a different approach to address this issue by converting into heat the rest of the 93 percent of the sunlight and drive the chemical reaction at elevated temperatures. Figure 5.2 displays the idea schematically.

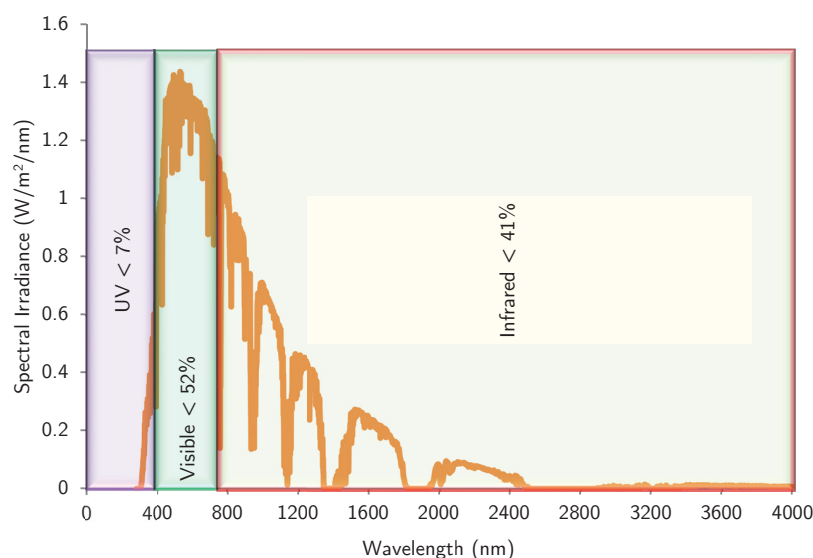


Figure 5.1. Spectral distribution of sunlight based on NREL data.

We conducted 2D axisymmetric thermal simulation using the COMSOL Multiphysics Software package in order to estimate the temperature values that we can reach in our microreactor. The model's geometry is exactly the same as the one used in the experiments. One set of simulations is done assuming air free convective cooling on all boundaries and another set is done assuming an insulated bottom surface and air free convection on the other ones. At the bottom of the reaction chamber a heat source of 700 W/m^2 is considered due to the 70%

absorption of the sunlight (1 kW/m^2) by the absorber layer. Figure 5.3 shows the results of these simulations indicating a maximum temperature of 50°C and 84°C for the non-insulated and insulated cases, respectively.

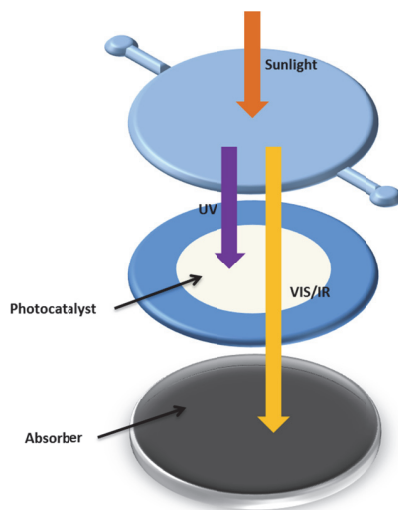


Figure 5.2. Schematic of solar thermal harvesting for photocatalysis

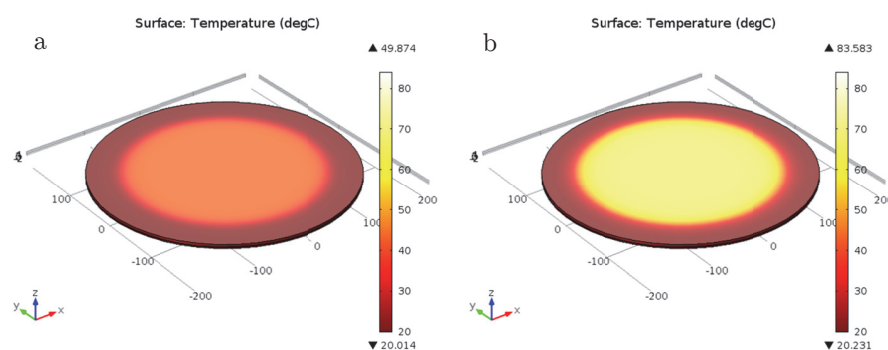


Figure 5.3. Temperature profile of a reactor with integrated absorber. a) Without insulator at the bottom. b) With insulation at the bottom.

5.3 Device Fabrication

Three different reactors with a capacity of $350 \mu\text{L}$ were fabricated. The first one is a photo reactor with a porous TiO_2 thin film at the bottom. The second one is a photo-thermal reactor with an additional carbon black absorber layer beneath the titania layer and the third one is a thermal reactor lacking the catalytic bed.

The reaction chamber is cylindrical with base diameter of 3 cm and height of 500 μm . This specific shape is selected to minimize the heat loss from the side

walls. An SU8 mold is first realized using UV lithography and then PDMS is used to replicate the shape of the reactor. The porous catalytic bed is made by the sol-gel method in two steps²⁰: TiO₂ colloid preparation followed by deposition of the porous thin film on the glass substrate. To prepare the colloidal solution, 0.4 gr of anatase titania nanopowder with average size of 25 nm (Sigma Aldrich) was added to 20 ml of DI water containing 16 ul of acetylacetone (Fluka) under magnetic spinning. Acetylacetone prevents aggregation of nanoparticles. After few minutes, 8 ul of Triton X-100 (Fluka) is added to improve the wetting properties of the colloid. Finally, 0.1 gr of polyethylene glycol, PEG, (Sigma Aldrich) was added and the solution was kept overnight under continuous stirring. PEG improves porosity of the final titania thin film.

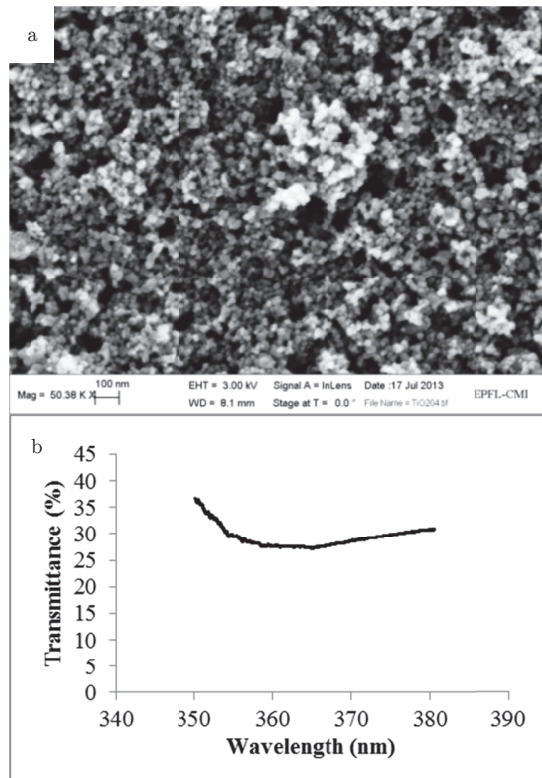


Figure 5.4. a) SEM image of the titania film showing its small pores. b) Transmittance spectra of the thin catalytic film in the UV region.

In the second stage, the upper area of a float glass wafer is wet etched by 10 μm in order to highlight the edges of reactor chamber's base. 50 μl of the colloid was applied to the center of the etched area and it was spread over the whole area by spin coating for one minute. Non-etched areas are cleaned with acetone. Finally, the calcination step at 500 $^{\circ}\text{C}$ is done for 90 minutes. This step is necessary to get rid of organic additives present in the thin film and also to get porous structures. Finally, a uniform and translucent titania film was visible on

top of the glass slide. The SEM image of this porous film is presented in Figure 5.4a. The transmittance of this thin film is measured in both the UV and visible regions using a spectrometer (Andor Technology). These measurements report transmittance of less than 30 percent between 360 to 380 nm (Figure 5.4b) and above 60 percent for wavelength larger than 430 nm.

The photocatalyst covered glass and PDMS chamber were plasma-bonded together. A 3 cm by 3cm glass slide, 500 μm thick, was also plasma-bonded to the top of the PDMS in order to increase its stiffness and prevent it from bending and touching the bottom of the reactor. A black absorber layer is made out of black PDMS which is obtained by mixing 40 nm carbon black nanoparticles with PDMS (1:15 ratio) and curing it at 70 $^{\circ}\text{C}$ overnight²⁵. The thickness of this layer is approximately 2 mm and it was plasma-bonded to the backside of bottom glass slide. The photothermal reactor's fabrication process flow and pictures of fabricated devices are demonstrated in Figure 5.5.

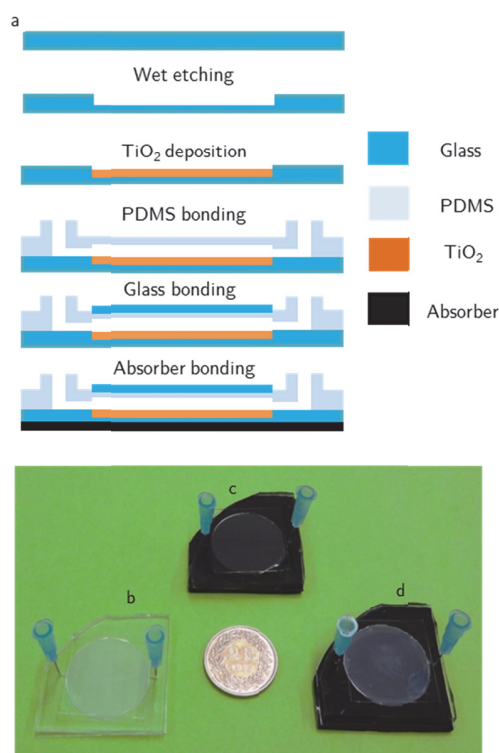


Figure 5.5. a) Fabrication procedure of a photo-thermal reactor. b) Fabricated photo reactor. c) Fabricated thermal reactor. d) Fabricated photo-thermal reactor.

5.4 Results and Discussion

The experiments were done with a 12 V, 80 W halogen light source with a tubular light guide which filters the light to match the solar spectrum in the UV and

visible regions. The distance between the optofluidic reactor and the tip of the light guide is adjusted by means of a power meter to match the 1X solar flux of 1 kW/m^2 . In addition, integration of the light guide prevents the heat generated by the lamp to reach the reactor, therefore, avoiding erroneous results. Comparison between the solar spectrum and the light source's spectrum is presented in Figure 5.6, both measured using an Ocean Optics HR4000-CG spectrometer. The solar measurement was done at 12 pm of a clear sunny day.

350 μl of $3\text{e-}5 \text{ M}$ solution of MB (Fisher Scientific) is injected into each reactor and put under radiation for 15 minutes. While running the experiment for the photothermal reactor, the reactor's bottom surface is put in touch with silica aerogel grains which are excellent insulators with thermal conductivities of 0.02 W/mK at atmospheric pressure and 45°C ²⁶. The liquid is collected in cuvettes afterwards for absorbance measurements using a precise spectrometer (Andor Technology). Absorbance can be related linearly to the concentration of MB in water according to the Beer–Lambert law since the initial concentration of MB is very small ($3\text{e-}5 \text{ M}$). Degradation percentage is calculated by monitoring absorbance change before and after exposure at 664 nm corresponding to the MB's peak absorbance¹⁹. The detailed degradation pathway of MB in aquatic solution is reported in previous works²⁷.

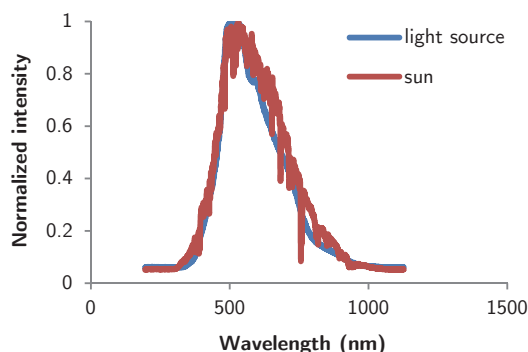


Figure 5.6. Comparison between solar and light source's spectra.

Absorbance curves for the three reactor types are shown in Figure 5.7 together with that of the pristine solution. Corresponding values at 664 nm for the initial solution, thermal, photo, and photothermal reactors are 95, 93, 73, and 55 percent, respectively. The absorption peak is also blue-shifted as we move from the initial solution towards the photothermal reactor. This is an indication of demethylated dyes formation inside the reactors²⁸. MB degradation amount is very small in the thermal reactor due to the lack of photocatalytic effect. The photo reactor shows 22 percent reduction in MB concentration and the photothermal

reactor 40 percent for the same conditions. This 82 % enhancement is the result of heating.

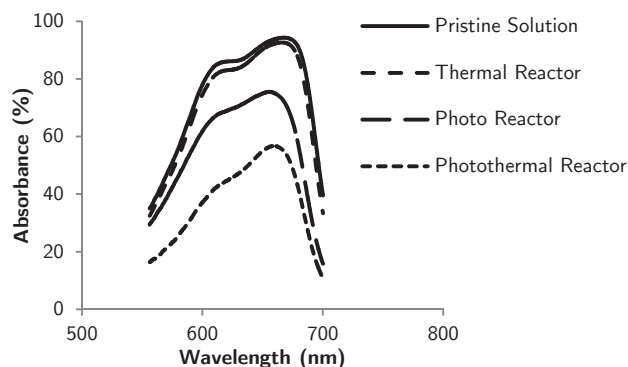


Figure 5.7. Absorbance curves for three different reactors compared with the initial solution

Control experiments have been done using the photo reactor on a hot plate at different temperatures. The closest results to the photothermal reactor are obtained at temperature of 42 °C measured by a thermocouple at hotplate's surface. Figure 5.8 depicts that the photothermal reactor degrades MB about 5 percent more than the photoreactor at this elevated temperature. Thus, the equilibrium temperature inside the photoreactor should be slightly above this value, i.e. around 45 °C. This temperature is limited by the transmittance properties of the titania thin film. In order to raise the temperature, a visible-near infrared (VIS-NIR) absorber can be used for fabrication of the reactor's top surface. This material should transmit UV light (below 400 nm) and use the longer wavelengths for heating of the chamber. Such a material can be realized by mixing PDMS with appropriate dyes and then characterizing its transmission/absorption properties²⁹.

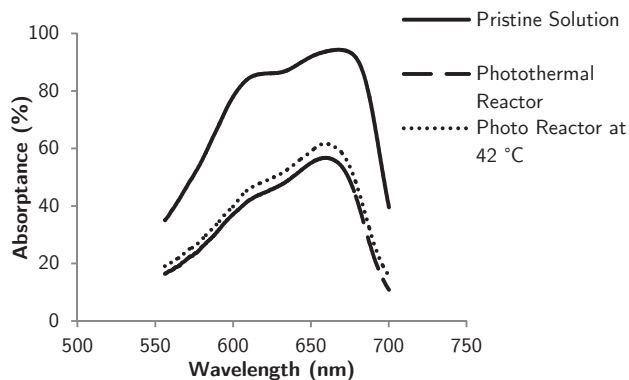


Figure 5.8. Results of the control experiment with photo reactor on a hot plate set at 42 °C and comparison with photothermal reactor's obtained values.

5.5 Conclusion

In order to observe the effect of solar thermal harvesting on photo reactions, water purification capabilities of thermal, photo, and photothermal reactors are investigated under similar working conditions. One sun is used as the light source and TiO_2 as the photocatalyst in a fixed bed configuration. The photothermal reactor showed the best performance with 82 percent augmentation over the unheated photo reactor. This can be explained by comparing titania's band gap energy and solar spectra: almost 93 percent of the sunlight is not used by titania. This means that this large portion of energy is absorbed by the absorber beneath catalytic bed in this reactor and turned into heat favoring reaction kinetics. To our knowledge, this is the first demonstration of the exploitation of solar energy as the shared source for both heating and catalytic purposes.

Bibliography

1. W. Shockley and H. J. Queisser, *J Appl Phys*, 1961, **32**, 510-&.
2. X. G. Zhu, S. P. Long and D. R. Ort, *Annu Rev Plant Biol*, 2010, **61**, 235-261.
3. M. S. Dresselhaus and I. L. Thomas, *Nature*, 2001, **414**, 332-337.
4. G. W. Crabtree and N. S. Lewis, *Phys Today*, 2007, **60**, 37-42.
5. D. F. Ollis, *Cr Acad Sci Ii C*, 2000, **3**, 405-411.
6. J. Zhao and X. D. Yang, *Build Environ*, 2003, **38**, 645-654.
7. J. H. Mo, Y. P. Zhang, Q. J. Xu, J. J. Lamson and R. Y. Zhao, *Atmos Environ*, 2009, **43**, 2229-2246.
8. A. D. Compaan, *Sol Energ Mat Sol C*, 2006, **90**, 2170-2180.
9. S. Linic, P. Christopher and D. B. Ingram, *Nat Mater*, 2011, **10**, 911-921.
10. M. Ni, D. Y. C. Leung and M. K. H. Leung, *Int J Hydrogen Energ*, 2007, **32**, 3238-3247.
11. U. I. Gaya and A. H. Abdullah, *J Photoch Photobio C*, 2008, **9**, 1-12.
12. K. Kabra, R. Chaudhary and R. L. Sawhney, *Ind Eng Chem Res*, 2004, **43**, 7683-7696.
13. T. E. Agustina, H. M. Ang and V. K. Vareek, *J Photoch Photobio C*, 2005, **6**, 264-273.
14. D. Bahnemann, *Sol Energy*, 2004, **77**, 445-459.
15. M. N. Chong, B. Jin, C. W. K. Chow and C. Saint, *Water Res*, 2010, **44**, 2997-3027.
16. S. Malato, P. Fernandez-Ibanez, M. I. Maldonado, J. Blanco and W. Gernjak, *Catal Today*, 2009, **147**, 1-59.
17. T. A. Westrich, K. A. Dahlberg, M. Kaviani and J. W. Schwank, *J Phys Chem C*, 2011, **115**, 16537-16543.
18. D. Erickson, D. Sinton and D. Psaltis, *Nat Photonics*, 2011, **5**, 583-590.
19. H. Lindstrom, R. Wootton and A. Iles, *Aiche J*, 2007, **53**, 695-702.
20. L. Lei, N. Wang, X. M. Zhang, Q. D. Tai, D. P. Tsai and H. L. W. Chan, *Biomicrofluidics*, 2010, **4**.
21. A. Fujishima and K. Honda, *Nature*, 1972, **238**, 37-+.
22. C. A. Gueymard, D. Myers and K. Emery, *Sol Energy*, 2002, **73**, 443-467.
23. A. M. Smith and S. M. Nie, *Accounts Chem Res*, 2010, **43**, 190-200.
24. X. M. Zhang, Y. L. Chen, R. S. Liu and D. P. Tsai, *Rep Prog Phys*, 2013, **76**.
25. T. Buma, M. Spisar and M. O'Donnell, *Appl Phys Lett*, 2001, **79**, 548-550.

26. M. Reim, W. Korner, J. Manara, S. Korder, M. Arduini-Schuster, H. P. Ebert and J. Fricke, *Sol Energy*, 2005, **79**, 131-139.
27. A. Houas, H. Lachheb, M. Ksibi, E. Elaloui, C. Guillard and J. M. Herrmann, *Appl Catal B-Environ*, 2001, **31**, 145-157.
28. C. Yogi, K. Kojima, N. Wada, H. Tokumoto, T. Takai, T. Mizoguchi and H. Tamiaki, *Thin Solid Films*, 2008, **516**, 5881-5884.
29. O. Hofmann, X. H. Wang, A. Cornwell, S. Beecher, A. Raja, D. D. C. Bradley, A. J. deMello and J. C. deMello, *Lab Chip*, 2006, **6**, 981-987.

Chapter 6

Vapor-fed microfluidic hydrogen generator

Water-splitting devices that operate with humid air feeds are an attractive alternative for hydrogen production as the required water input can be obtained directly from ambient air. This chapter presents a novel proof-of-concept microfluidic platform that makes use of polymeric ion-conductor (Nafion[®]) thin films to absorb water from air and enables the electrochemical water-splitting process. Modelling and experimental tools are used to demonstrate that these microstructured devices can achieve the delicate balance between water, gas, and ionic transport processes required for vapor-fed devices to operate continuously and at steady state, at current densities above 3 mA/cm². The results presented here show that factors such as the thickness of the Nafion films covering electrodes, convection of air streams, and water content of the ionomer can significantly affect the device performance. The insights presented by this work provide important guidelines for the material requirements and device designs that can enable practical electrochemical hydrogen generators that work directly with ambient air.

6.1 Introduction

A large increase in the share of renewable energy sources for power production is essential to significantly decrease the current levels of CO₂ emissions^{1, 2}. Large amounts of investment have been allocated to increase the capacities of solar and wind-based power generation. At the same time, power derived from these intermittent sources has brought significant challenges for their incorporation into our current electricity distribution infrastructure, where electricity generation generally needs to match the demand. Efficient means for power storage and redistribution are needed in order to allow a further penetration of renewable energy power production. Electrochemical approaches for power storage by devices such as batteries, flow-batteries, electrolyzers and fuel cells exhibit a significant advantage over other means of storage, namely their efficiency is not limited by the Carnot efficiency of heat engines, as it can reach levels above 70%. Water electrolyzers, in particular, can easily accommodate excess renewable electricity by converting it into hydrogen fuel, which can be stored and subsequently used to regenerate electricity in a fuel cell^{3, 4}.

Classical electrolysis systems operate under alkaline electrolytes which allow the use of inexpensive and earth-abundant catalysts that operate under basic conditions. These alkaline systems pose significant corrosion challenges for all system components as they require operation under strongly basic electrolytes. More recent approaches to water electrolysis implement membrane-electrode assemblies (MEAs) based on proton exchange polymer membranes (PEM) and noble metal catalysts to perform the water splitting process⁵⁻⁷. These systems have significant advantages as the ohmic losses through the polymer are minimized by the implementation of thin electrolyte layers, and they are fed with deionized water, alleviating most of the corrosion issues posed by alkaline electrolyzers. One alternative to using deionized water as the feed is to extract water directly from the vapor phase. Examples of vapor phase water splitting have been demonstrated using MEAs at low temperatures⁸ and photoelectrochemical material systems operated directly from air⁹. Performing water electrolysis from the vapor phase exhibits several advantages: lower water splitting potential, lack of bubble evolution at the catalysts surface, and simplified implementation of the electrolyzer by direct humid air-based operation^{9, 10}. On the down side, water splitting from humid air poses significant transport challenges, as the low concentration of water can limit the water-splitting rates in the device.

The operation of vapor-fed electrolyzers requires all of the ionic current between the reaction sites to be transported by a solid state ion conductor (i.e. proton or hydroxide ion-conductor). This solid electrolyte needs to satisfy a series of conditions: (i) the electrodes need to be in direct contact with the electrolyte; (ii)

the electrolyte needs to have high water solubility as water is consumed in the reaction; (iii) the diffusivity of dissolved H_2 and O_2 gases through the electrolyte needs to be high enough to allow for a product diffusive flux that equates the production rate at the electrodes surface; (iv) the concentration of gases in the electrolyte cannot reach saturation levels in order to avoid bubble nucleation which would cause delamination of the electrolyte, and (v) the water from the environment needs to diffuse with minimum resistance to avoid water depletion at the surface of the electrodes. Nafion thin-films are suitable for this task as they provide remarkable ionic conduction, fast water uptake, and good chemical stability¹¹⁻¹⁶. Based on Nafion's transport properties, the polymer films covering the electroactive sites must not be thicker than several micrometers to sustain current densities in the electrolyzer in the order of several mA/cm^2 (1 mA/cm^2 corresponds to $0.0187\text{ mmol/hr-cm}^2$ of H_2 at 100% faradaic efficiency)^{17-19,23}. Within this thickness range, the in-plane ionic resistance in the polymer can be very significant. One way to mitigate the high resistance is to limit the path length for ion migration between electrodes to short distances, in the order of 10-100's μm . To mitigate these constraints based on Nafion's transport properties, a proof-of-concept microfluidic water-splitting device was fabricated. Microfluidic devices are an attractive platform because their architecture can be easily tuned, their modularity allows for components to be easily exchanged, and the transport characteristics in these devices are well defined. Several studies have focused on the use of microfluidic platforms for fuel cell applications under liquid-electrolytes²⁰⁻²³, and only recently a microfluidic device was described for water electrolysis from highly acidic (1M sulphuric acid) electrolytes²⁴. To the best of our knowledge, this study presents the first report on microfluidic vapor-fed electrolyzers.

6.2 Methodology

6.2.1 Device design

The device presented in this work consists of a set of parallel electrodes covered with a thin layer of Nafion and a set of parallel channels that collect the product gases generated above each of the electrodes. Figure 6.1(a) shows a schematic representation of the cross-section of this parallel channel device. In order to maximize the areal coverage of the electrodes in the device, this architecture was arranged in a double-spiral geometry, allowing maximum coverage of the electrodes in the chip. The double spiral morphology also allowed for independent fluid streams to be collected from the hydrogen and oxygen production channels which prevented the back-diffusion of H_2 into the oxidation side. Figure 6.1(b) shows a photograph of the spiral channel structure where water streams with dissolved dyes are flowed through separated streams. It is important to point

out that this device architecture is fundamentally different from that of MEAs used in PEM electrolyzers. In MEAs, nanostructured catalysts layers are separated by a parallel ionomer membrane, typically $> 100 \mu\text{m}$ thick. Under this MEA arrangement, the ionic flux through the membrane is equal to the ionic generation rate in the catalyst layer. In the microfluidic device proposed above, the ionic current is carried through the cross section of an ionomer film of thickness below $1 \mu\text{m}$. In this configuration, the ionomer in the inter-electrode region experiences an ionic current density that is more than 125 times higher than that imposed at catalyst surface. This results in a high ionic resistance in the device, and imposes the requirement for short ionic path lengths between the electrodes to minimize the ohmic drop.

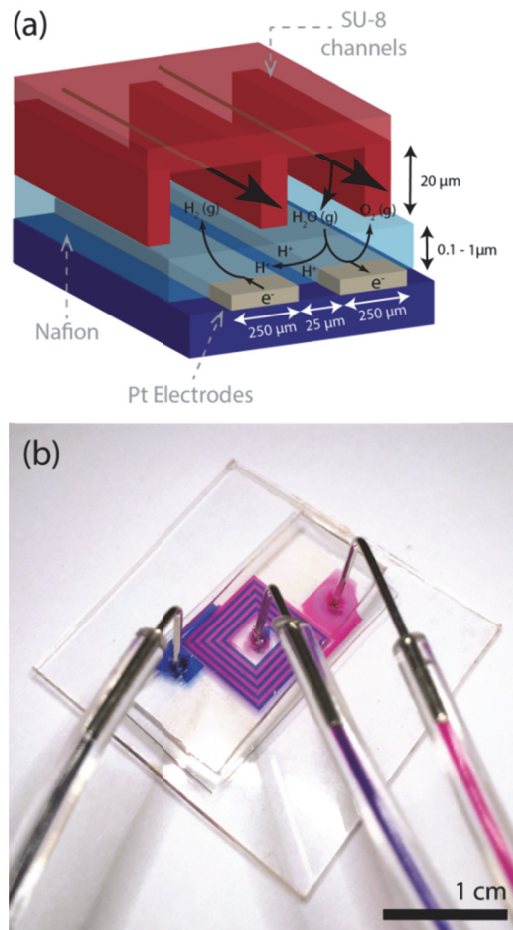


Figure 6.1. (a) Diagram of device geometry and (b) fluidic channels showing separated pathways for H_2 (blue) and O_2 (pink) evolution channels.

6.2.2 Model development

A steady-state laminar, isothermal 2D model of the microfluidic electrolyzer was developed following modelling methods of proton exchange membrane electroly-

sis previously established in the literature^{18, 25}. The model implemented in this study made use of a constant conductivity for the Nafion phase. Variations in the water content throughout the polymer film would lead to a non-uniform conductivity, which is not captured in the current model and can lead to differences between modelling results and experimental measurements²⁶. A better understanding of the internal polymer morphology and water uptake throughout the polymer film could lead to more precise models that better describe the experimental systems²⁷. The model incorporated the transport phenomena between the two electrodes, the polymeric electrolyte, and the two channels for reactants delivery and product removal, as depicted in Figure 6.1(a)²⁸. The ionomer was considered as an ohmic conductor and as a diffusive media. The conservation of charge and the species transport in the electrolyte were consequently given by two Laplace equations, assuming spatial constant conductivity and diffusivity in the electrolyte,

$$\Delta V = 0, \quad (1)$$

$$\Delta c_i = 0. \quad (2)$$

The incoming flux of oxygen, water, and hydrogen from the channel to the electrolyte in the direction normal to catalyst interface was given by,

$$\nabla c_i \cdot \hat{\mathbf{n}} = \frac{\text{Sh } D_i^b}{e D_i^m} (c_i - c_i^b), \quad (3)$$

where D_i^b and D_i^m were the diffusion coefficients of species i in the bulk of the air-fed channels and the electrolyte, respectively. $\hat{\mathbf{n}}$ was the inward ionomer surface normal, e the height of the channel, and Sh the Sherwood number.

The current densities for the hydrogen evolution and oxygen evolution reactions ($i_{\text{R,OER}}$ and $i_{\text{R,HER}}$) are modeled by using concentration-dependent Tafel approximations²⁹,

$$i_{\text{R,OER}} = i_{0,\text{OER}} \left(\frac{c_{\text{H}_2\text{O}}}{c_{\text{H}_2\text{O}}^b} \right) \exp \left(\frac{\alpha_a F (\Phi_s - \Phi_e - E_{\text{O}_2/\text{H}_2\text{O}})}{RT} \right), \quad (4)$$

$$i_{\text{R,HER}} = -i_{0,\text{HER}} a_{\text{H}^+} \exp \left(\frac{\alpha_c F (\Phi_e + E_{\text{H}^+/\text{H}_2})}{RT} \right), \quad (5)$$

where a_a and a_c are the charge transfer coefficients at the anode and at the cathode, respectively, and $E_{\text{O}_2/\text{H}_2\text{O}}$ and $E_{\text{H}^+/\text{H}_2}$ the Nernst potential of the anodic and cathodic reactions, respectively, with reference concentrations at 20°C and 1 atm. $i_{0,\text{OER}}$ and $i_{0,\text{HER}}$ are the exchange current densities for the oxygen evolution and hydrogen evolution reactions, F is Faraday's constant and T the oper-

ating temperature. The activity of protons in the electrolyte was fixed by the concentration of sulfonic groups, i.e. $a_{H^+} = 1$. The boundary conditions at the electrode/electrolyte interfaces are given by,

$$\nabla V \cdot \hat{n} = -\frac{i_{R,OER/HER}}{\sigma}, \quad (6)$$

$$\nabla c_{H_2O} \cdot \hat{n} = \frac{i_{R,OER}}{2 FD_{H_2O}^m}, \quad (7)$$

$$\nabla c_{O_2} \cdot \hat{n} = -\frac{i_{R,OER}}{4 FD_{O_2}^m}, \quad (8)$$

$$\nabla c_{H_2} \cdot \hat{n} = \frac{i_{R,HER}}{2 FD_{H_2}^m}. \quad (9)$$

The inlet saturation pressure of water vapor was calculated for a relative humidity of one with the correlation from Buck³⁰,

$$p_s(T) = 611.21 (1 + 3.46 \times 10^{-8} p) \exp\left(\frac{17.520 T}{240.97 + T}\right). \quad (10)$$

where p is the total pressure. All other external boundaries are considered as walls (no flux condition). The numerical values of the parameters are given in Table 6.1. The exchange current densities, anodic charge transfer coefficient and membrane conductivity were calculated to fit the experimental results.

Table 6.1– Numerical values of the model parameter used in the reference case.

Parameter	Value
Diffusion coefficients of water ³¹⁻³³	$D_{H_2O}^b = 0.24 \text{ cm}^2 \text{ s}^{-1}$ $D_{H_2O}^m = 7.2 \times 10^{-6} \text{ cm}^2 \text{ s}^{-1}$
Diffusion coefficients of oxygen ^{26, 34, 35}	$D_{O_2}^b = 0.18 \text{ cm}^2 \text{ s}^{-1}$ $D_{O_2}^m = 5.8 \times 10^{-7} \text{ cm}^2 \text{ s}^{-1}$
Diffusion coefficients of hydrogen ^{36, 37}	$D_{H_2}^b = 0.76 \text{ cm}^2 \text{ s}^{-1}$ $D_{H_2}^m = 1.6 \times 10^{-6} \text{ cm}^2 \text{ s}^{-1}$
Oxygen concentration in the channels	$c_{O_2}^b = 0.21 \times c^0 = 8.61 \text{ mol m}^{-3}$
Exchange current densities	$i_{0,HER} = i_{0,OER} = 3 \times 10^{-11} \text{ A cm}^{-2}$
Charge transfer coefficients ³⁸	$\alpha_a = 0.85; \alpha_c = 1$
Membrane conductivity	$\sigma = 4 \times 10^{-5} \text{ S cm}^{-1}$

6.2.3 Device Fabrication

The devices were fabricated in the Center of Micronanotechnology at the Swiss Institute of Technology in Lausanne (EPFL). Two separate chip components of the microfluidic devices were fabricated: (1) one chip containing the electrodes

and (2) one chip that contained the channel structures. The two chips were subsequently bonded after aligning the channels with the electrodes.

For the electrode fabrication, a lift-off technique was implemented. A 200 nm thermally grown SiO_2 wafer was used to photolithographically pattern the electrode structure in AZ1512 on LOR photoresists (250 μm wide electrodes separated by 25 μm , and with a total active length of 10.95 cm). Then, a Leybold Optics LAB 600H e-beam evaporator system was used to deposit 200 nm of Platinum (Pt) on top of a 20 nm Titanium (Ti) seeding layer, leading to flat electrode surfaces. To characterize the roughness of the surface atomic force microscopy measurements were carried using a Bruker Dimension FastScan System (Figure 6.2), which demonstrated a mean square root roughness of 2.2 nm for the metal film. The metal deposition was followed by lift-off in Microposit Remover 1165.

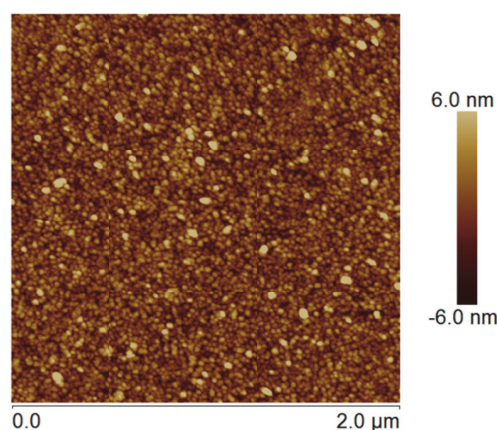
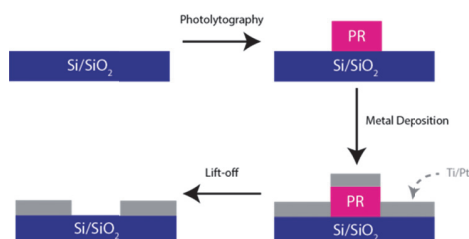


Figure 6.2. Atomic force microscopy image of the surface of Platinum electrocatalyst. By analyzing the obtained data, it was determined that the surface area of the catalyst was only 6.1% higher than its projected area. The root mean square roughness of the sample was determined to be 2.2 nm.

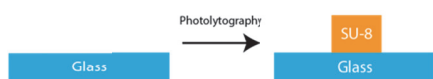
A different process was developed for the fabrication of a set of mixed Pt and Iridium oxide (IrO_x) electrodes. First, 200 nm of Pt and 20 nm of Ti were deposited by e-beam evaporation as described above. Then, the cathode structure was photolithographically patterned with AZ1512 photoresists. Ion beam etching (Veeco Nexus IBE350) was used to remove the metal films from areas outside the desired cathode structure, and the remaining photoresist was stripped off using oxygen plasma in a Tepla Gigabatch Plasma Stripper system. A second photolithography step was used to protect with AZ1512 the cathode structure prior to deposition of IrO_x . A 100 nm film of IrO_x was then deposited via reactive sputtering, using an Alliance-Concept DP 650 sputtering system, on top of a 150 nm film of chromium (Cr) which acted as a seeding layer and to increase

the electrical conductivity through the anode. A third lithography step was performed to pattern with AZ1512 the anode structure. Lastly, ion beam etching was used to remove the IrO_x and Cr films from the areas outside the desired anode structure. The remaining photoresists was again stripped off using oxygen plasma.

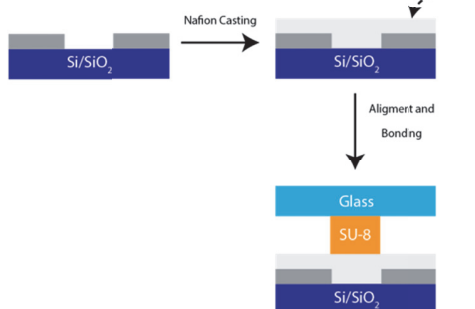
Microelectrode Fabrication:



Channels Fabrication:



Channels Fabrication:



Mixed Catalyst Microelectrode Fabrication:

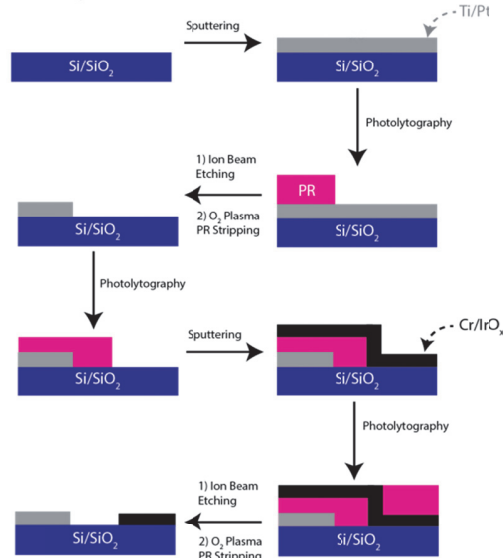


Figure 6.3. Process flow diagram for microfabrication of vapor-fed electrolyzers

After removing the excess photoresist with acetone, the chip containing the electrodes was exposed to oxygen plasma for 5 minutes, and Nafion films were spin casted from solutions (15% Nafion solution from ion-power) diluted in isopropanol (Sigma-Aldrich). The film thicknesses obtained at different spin coating speeds were characterized using a Filmetrics F20-UV spectroscopic reflectometer. For the channel fabrication, a 20 μm layer of SU-8 was photolithographically patterned on top of a glass wafer (the channels followed exactly the pattern of the electrodes). After the chip fabrication, both the wafers with electrodes and channels were diced using a Disco DAD321 automatic dicing saw, gas inlet and outlet ports were manually drilled in glass, the individual chips were aligned under a microscope, and bonded at 200 $^{\circ}\text{C}$ (above the glass transition temperatures of Nafion and SU-8). A process flow diagram for all the fabrication steps is presented in Figure 6.3.

6.2.4 Electrochemical Characterization

All the electrochemical measurements were performed using a Biologic VSP-300 potentiostat/galvanostat system. Potentioelectrochemical impedance spectrometry (PEIS) measurements were performed at frequencies between 500 Hz to 3 MHz, and 20 mV amplitude. Impedance results were analysed following electrochemical equivalent circuit models described elsewhere to extract ohmic resistances of the devices^{14, 39}. Measurements for equilibrated devices were performed by placing the electrode chips covered with Nafion films in a closed chamber equilibrated with deionized water. The devices were allowed to equilibrate for more than one hour, and measurements were performed when conductivity values reached steady state values. For flow experiments, a NewEra syringe pump was used to control flow rates, and gases were pulled from the outlet while the device inlets were connected to air or nitrogen (N₂) in a container equilibrated with water at ~100% relative humidity (RH).

6.2.5 Gas Composition Characterization

Assembled devices were operated by flowing humid air streams saturated with water through the channels at a flow rate of 3 mL/hr using a syringe pump for each of the channels (Syringe pumps obtained from New Era). The experiments were run for several hours and gases were collected using gas tight syringes. The sample gases were injected directly into a Bruker 456-GC system with N₂ as the carrier gas to determine the concentration of H₂ in each channel.

6.3 Results and Discussion

Throughout this study, several factors affecting the device performance were assessed, and their effects are presented below. Factors related to transport mechanisms included the effects of ionic, water and gas transport on device behaviour. Additional electrochemical factors such as the reaction kinetic limitations and effects of parasitic oxygen reduction inherent of operation under ambient air were also considered. The findings presented below demonstrate the required balance between the multiple electrochemical and transport processes for optimal air-based operation of water splitting devices.

6.3.1 Interplay between transport and electrochemical processes

One of the most crucial factors that define the device performance is the ability to provide low transport resistance for both ionic and gas species through the polymer film. In this sense, the thickness of the ionomer films is a crucial parameter and can define the device performance. Thicker films will result in lower ohmic resistances but at the same time will pose larger transport limitations for

gas and water diffusion between the electrodes and the flow streams. Modelling results clearly demonstrate that lower ohmic drops are expected as the film thickness increases (Figure 6.4 (a)). This implies that in devices with thicker Nafion films a larger portion of the applied potential could be used to drive the electrochemical reaction and consequently lead to higher production rates. On the other hand, higher transport resistance for water in thicker films would result in kinetic limitations at the surface of the electrodes as the water concentration decreases. The trade-off between these two effects determines the device current output (Figure 6.4 (b)).

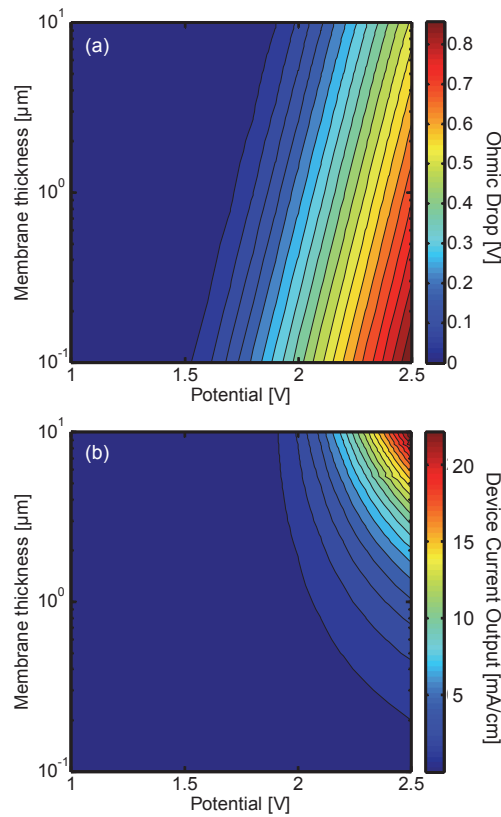


Figure 6.4. (a) Ohmic drop in the device as a function of membrane thickness and applied potential. The results show the expected decrease in ohmic losses in the device as the thickness of the ionomer increases. The effect of polymer thickness and applied potential on the device current output is presented in (b). As depicted by the result the maximum current levels are achieved for a thickness range where the ohmic losses are minimized.

The balance between the ohmic, mass transport, and reaction kinetics losses also results in inhomogeneities in the current distribution across the electrodes. Reaction kinetic and transport losses drive the system towards a uniform current distribution, while ionic resistances between the electrodes would favour higher current densities at the edges of the electrodes in order to minimize the ionic

migration path lengths²³. As shown in Figure 6.5, the current density distribution is uniform at low applied potentials, while anisotropies arise as the potential increases, especially above 2 V. At low applied potentials, the device exhibits low current densities which then lead to a low potential drop from ohmic resistance. As the applied potential increases, the current density in the device reaches levels where the ohmic drop is comparable to the catalyst overpotential. This in turn results in a non-uniform current density distribution, as higher levels of currents are pushed towards electrode areas with the lowest ohmic resistances, i.e. the electrode edges. These effects demonstrate the role of multiple transport and chemical processes that are intrinsically present in these complex devices, and the importance of balancing them in order to optimize the performance.

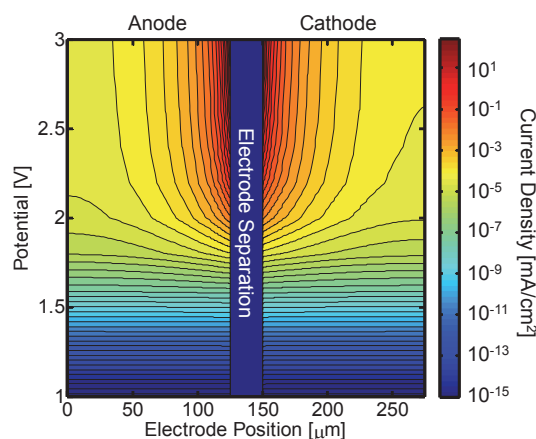


Figure 6.5. Current distribution across the electrodes separated by an ionomer layer. The ionomer thickness corresponds to 1 μm , and the anode and cathode center points correspond to electrode positions of 0 and 275 μm respectively. The nonuniformities observed in the current distribution are caused by the trade-off between the ohmic resistance and reaction kinetic resistance.

As demonstrated from modelling, the proton conduction through the Nafion film is a critical parameter that directly affects the device performance. Potentiostatic electrochemical impedance spectroscopy (PEIS) measurements were performed to characterize the ohmic resistance of devices with Nafion films of various thicknesses (between 300-800 nm), and results are presented in Figure 6.6. Within the device architecture used in this study, the derived resistances varied from 140 to 200 ohms, while the contact resistances accounted only for 17 ± 1 ohms for all the devices. The measured resistances in the devices are significant but manageable and demonstrate that devices with thicker electrolyte layers will perform better, as long as water and gas transport through the films does not become limiting. Also, it is important to point out that the measured resistances in these thin films were characterized for electrodes equilibrated in humid air under passive conditions (i.e. no flow was applied). These conditions served as a

benchmark for comparing devices with different ionomer thicknesses under a controlled set of conditions. Moreover, these devices are expected to show the highest level of performance when the ionomer is fully hydrated after equilibration with humid air. As current is passed through the device, the water concentration in the film over the anode will decrease, and this will lower the conductivity of the material, and increase the ohmic drop in the device.

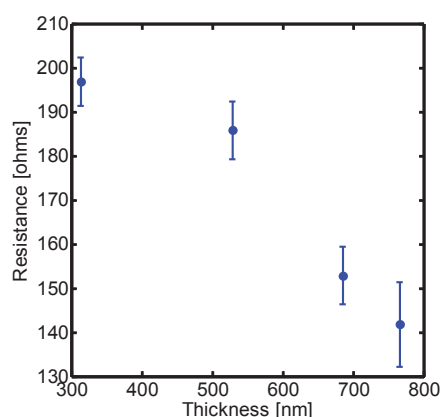


Figure 6.6. Device ohmic resistance decreasing as a function of ionomer thickness. The error bars denote standard deviation in the resistance measurements via potentiostatic electrochemical impedance.

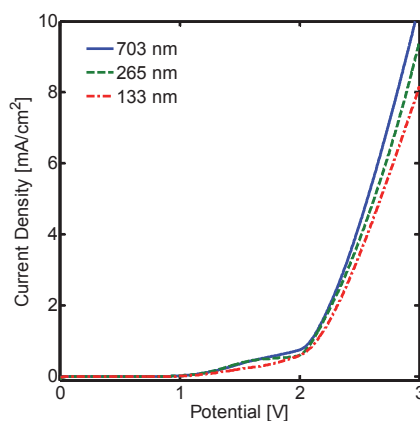


Figure 6.7. I-V characteristics of devices fabricated with different electrolyte thicknesses, showing performance improvements with thickness as a result of the lower ionic resistance in the device.

To better understand the overall performance of the devices, the I-V characteristics of the electrodes covered with Nafion were determined after equilibration with 100% RH air (Figure 6.7). The traces corresponding to different Nafion thicknesses show a typical behaviour for water electrolysis with Pt electrodes. The region below 2 V where the device exhibits low current levels (below 0.25 mA) is likely to be dominated by kinetic losses in the electrode surface, which

arise from catalyst overpotentials. In this region the ohmic drop associated with ionic transport in the electrolyte is expected to be small (<50 mV to 120 mV for films of 703 and 133 nm respectively), which is why the current levels are not affected significantly by the film thickness. As the applied potential and current increases, the potential requirement for ion transport also increases and starts to become significant. In this regime the film thickness starts to become an important parameter that affects the device performance, and increasing the thickness of the electrolyte allows the device to operate at higher current levels for a given potential.

6.3.2 Transient device behaviour

The electrochemical characterization presented above provides insights into critical design parameters of the microfluidic electrolyzers. Clearly, the devices presented here benefit from the use of thicker Nafion films which provide lower ionic resistances. Within the range of thicknesses investigated here, significant limitations to the diffusive transport of gases through the electrolyte film are not expected. If devices were to be operated at significantly higher current densities, the concentration of product gases in the electrode/electrolyte interface could reach levels above the gas solubility limit, nucleating bubbles and causing the electrolyte film to delaminate^{17, 18}. Moreover, the characterization described above corresponds to systems that have been equilibrated with humid air and the current levels achieved do not directly correlate to the ones for devices under continuous operation. As current is passed through the electrodes, local concentration gradients of water and gases in the Nafion film will evolve. In the case of the gases generated, the concentration build-up near the electrodes will result in additional overpotentials that need to be overcome. More importantly, the consumption of water inside the ionomer results in two adverse effects for the performance: (i) the decreased water concentration in the Nafion films will lower its conductivity and so increase the device ohmic resistance and (ii) the lower water concentration at the electrode interface will result in lower reaction rates at the catalyst. The second effect can be quite severe as the water splitting rate can be limited by the water diffusive flux into the electrodes. Figure 6.8 demonstrates the performance drop of devices operated at a constant 3 V applied potential. It can be clearly seen that within the first 5 minutes of operation, the current density in the devices drops sharply and it reaches lower steady values over time. Moreover, if the flowrates of feed gas are increased, the steady state current levels also increase. These flowrate effects are consistent with the transport limitations described above, as higher flowrates will increase the convective transport at the polymer/air interface and the water flux into the electrodes will increase. In the same way, the increase in convection will result in a faster flux of gases from the polymer films into the gas streams which in

turn will reduce the concentration overpotential at the electrodes. To understand the impact of the water content decrease in the Nafion film, PEIS measurements were performed after the device had achieved steady state (Figure 6.9) operation and the resistances in the devices were found to increase from ~ 200 ohms to at least 800 ohms in the case of flowrates of 15 mL/hr and above 6,000 ohms for the lowest flowrates of 0.5 mL/hr. These resistance levels will result in large ohmic drops in the device, >800 mV for devices operated at 1 mA with a feed flowrate of 15 mL/h.

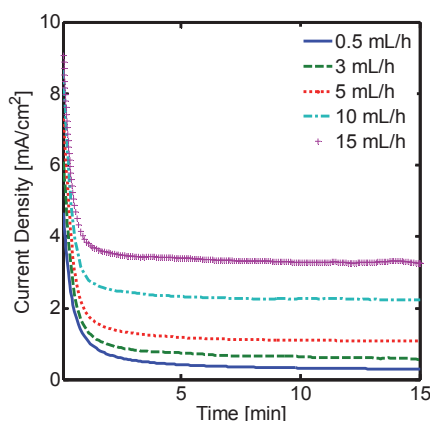


Figure 6.8. Current traces for a device with a 700 nm Nafion film operated at 3 V with different feed flowrates. The initial decay in performance suggests that transport limitations arise as the devices initially consumes water absorbed in the ionomer, and reaches different current levels at steady state. As the flowrate increases, these transport limitations ease, allowing the device to reach higher current densities.

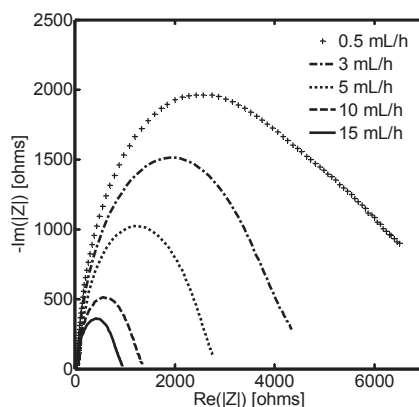


Figure 6.9. PEIS measurements on devices under different feed flowrates after 15 min of device operation at 3 V. The impedance spectra demonstrates an increase film resistance as the flowrate was reduced in the devices.

Although the initial performance of the devices decreases with time due to the transient effects described above, their performance at steady state is stable over

several hours. Figure 6.10 demonstrates the stable steady state behaviour of a device operated at 3 V with a total air flowrate of 3 mL/hr per channel. Moreover, the device used to perform the measurements presented below has been used for over a month with varying operating conditions and does not show signs of performance degradation. Both the electrode materials (Pt) and the ionomer (Nafion) show remarkable electrochemical stability, as is the case for this material in MEA's used in fuel cells and electrolyzers. This suggests that the devices described herein can be potentially operated over long periods of times.

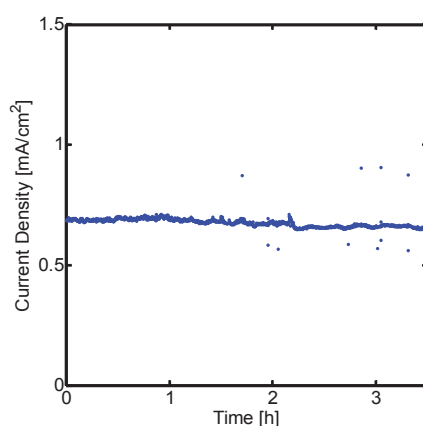


Figure 6.10. Long term behaviour of a device with a 700 nm Nafion film operated at steady state with an applied potential of 3 V across electrodes shows stable device operation over the course of several hours.

6.3.3 Gas transport across channels

Electrolysis devices need to limit the hydrogen crossover from the reduction to the oxidation channels in order to avoid product losses, especially by product recombination at the surface of the anode. It must be noted that downstream separation of the hydrogen gas is still required as its concentration in the product stream is expected to be low if the device is operated directly under humid air. Coupled mass transport and electrochemical models were developed to assess the degree of gas crossover through the Nafion film. Additionally, gas chromatography measurements were used to determine the extent of hydrogen back diffusion. In the devices described above, diffusion of H_2 across channels can happen through the Nafion thin-film that ionically connects the two electrodes. As the thickness of the films used lies below 1 μm , the H_2 crossover through the Nafion films is expected to be low. Modelling results demonstrate that the concentration of H_2 reaching the oxidation side corresponded to less than 1% of that produced in devices with Nafion thicknesses below 1 μm (Figure 6.11). These results suggest that the thickness of the film can be opti-

mized without affecting the gas crossover in the device. Experimental results of the device modelled here demonstrated low levels of crossover, as 97% of the H_2 in the system was collected in the reduction side, and 3% of it was collected in the oxygen side (Figure 6.12 presents the GC results). Cross-contamination at the inlet and outlets of the demonstration device, imperfections in the bonding between Nafion and the channel walls, as well as non-zero diffusion of H_2 through the SU-8 walls could result in the higher measured H_2 crossover when compared to the model estimations. It is important to point out that crossover of oxygen from the oxidation to the reduction channels can have similar detrimental effects due to recombination losses in the cathode. In the case of the devices presented in this study, the crossover of oxygen is expected to be lower than that measured for H_2 , as its permeability in Nafion is lower^{40, 41}.

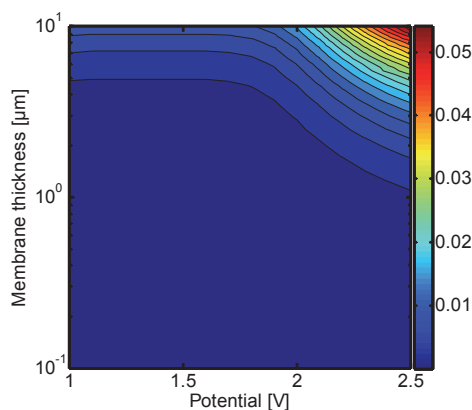


Figure 6.11. Hydrogen crossover flow between the cathode and the anode as a fraction of the hydrogen production rate at the cathode. The results show that the gas crossover across electrodes is expected to be low, in the order of 10^{-3} of the produced hydrogen.

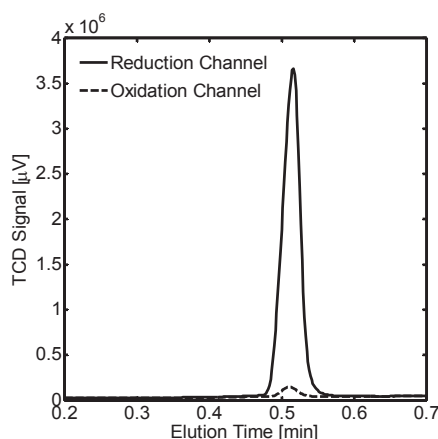


Figure 6.12. Gas chromatography traces for H_2 collected in the oxidation and reduction channel, showing small amounts of H_2 crossover between channels.

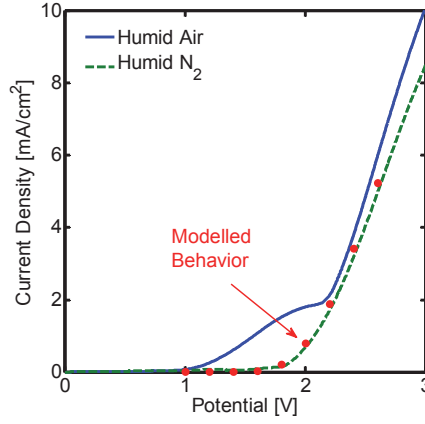


Figure 6.13. Electrochemical behaviour of a device operated with a feed flowrate of 15 mL/hr of air (solid line) or nitrogen (dashed line). The results demonstrate higher current densities in the presence of oxygen due to parasitic recombination reactions in the cathode. The current density values for the nitrogen-fed system compare well with modelling results, presented as the red dots in the graph.

It is important to point out that this study focused on the operation of devices with humid air, and the presence of O_2 in the feed can have several drawbacks in the performance of devices. When electrolysis devices are operated in the presence of air, the oxygen reduction reaction can compete with the hydrogen evolution reaction in the cathode, and the measured current output arises from both reactions. To assess the extent of this effect, current-voltage characteristics were measured for devices operated under humid air and humid N_2 (100% RH) as depicted in Figure 6.13. It can be noted that higher current densities are obtained when air (up to 19% higher at 3V) is present in the feed-stream. Similar effects have been reported elsewhere for the case of air-operated MEAs.⁸ Furthermore, the presence of oxygen in the H_2 stream can result in recombination losses, and a more complex downstream separation of the gases will be required to obtain pure H_2 fuel. The electrochemical model presented earlier follows the behaviour of the nitrogen fed device, further confirming the presence of additional parasitic reactions occurring in the electrodes when oxygen is present. Under humid N_2 , these parasitic electrode reactions are not present and the faradaic efficiency of the devices is expected to approach 100%. Given these conditions, the energy conversion efficiency at different current density levels can be estimated. The energy conversion efficiency (η) for the device operated under humid N_2 , assuming a 100% faradaic efficiency is calculated as⁸,

$$\eta = \frac{E_{H_2O,vap}^0}{E_{app}}$$

Where E_{app} is the applied potential and $E_{H_2O,vap}^0$ is the thermodynamic water splitting potential of water vapor Figure 6.14 presents a trace of the current density in the device as a function of efficiency, demonstrating that the device can operate at current densities above 2.5 mA/cm^2 with efficiencies higher than 50%.

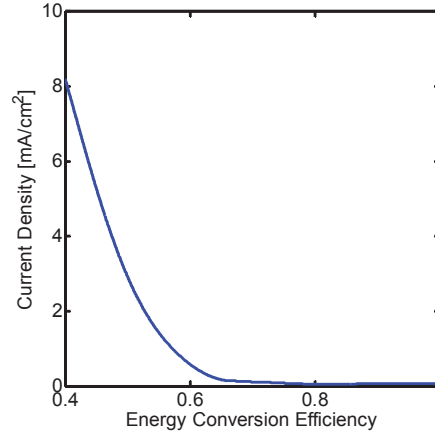


Figure 6.14. Current density versus energy conversion efficiency for a microelectrolyzer device consisting of a pair of Platinum electrodes and operated under humid N₂ streams at 100%RH.

6.3.4 Improving the reaction kinetics at the electrodes

The previous subsections discussed the interplay of multiple transport processes that play important roles in the performance of vapor operated electrolyzers, and highlighted directions for improvements in the device current outputs. While the devices described above used Pt as an electrocatalyst for both the oxygen and hydrogen evolution reactions, further gains can be attained by implementing catalysts with lower overpotentials. To demonstrate the performance improvements from the incorporation of catalysts with higher activity, a set of electrodes were fabricated with IrO_x as water oxidation catalyst and Pt for the proton reduction reaction. This catalyst combination is widely used in PEM electrolyzers as it allows MEAs to operate at lower potentials and with improved stability⁶. As demonstrated in Figure 6.15, significantly lower overpotentials can be achieved when IrO_x is used in the anodic reaction. Average current densities above 5 mA/cm^2 are observed at 2 V of applied potentials; compared to less than 2 mA/cm^2 in systems that used Pt for the oxygen evolution reaction. The recorded improvement is significant, and demonstrates that the incorporation of better catalysts leads to more efficient device operation.

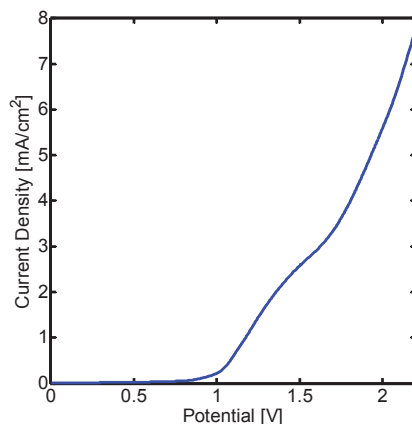


Figure 6.15. I-V characteristics of a set of Pt and IrO_x electrodes covered with a 700 nm film of Nafion. The use of IrO_x in the anodic reaction leads to a decrease in overpotential in the device.

6.4 Conclusions

The platform developed in this study demonstrates for the first time a room-temperature water-vapor microfluidic electrolyzer. This system allowed for a thorough electrochemical characterization of device architectures, and to gain insights on the effects of various design parameters on the performance of water-vapor electrolyzers. The findings of our study demonstrate the interplay of the multiple transport processes required for optimal device behaviour. In particular, ion-transport resistance in these devices can dominate their electrochemical behaviour; the measured resistance levels (>200 ohms) can account for a large portion of the overpotential required for the water splitting reaction (>200 mV at 1 mA current outputs). Moreover, under steady state operating conditions, ionic resistance in the device can increase significantly (by more than 400%) due to water consumption at the anode and concentration overpotentials may arise from the evolution of product gases near the electrodes. These effects can be partially mitigated by increasing convection at the gas/electrolyte interface and in this way increase the convective mass transfer, improving the efficiency of the device. It must be noted, that although Nafion films have desirable properties such as high proton conduction and electrochemical stability, its gas permeability is fairly low. This property is desirable for membranes in classic fuel cell and electrolyzer designs where gas crossover can affect the performance of devices, but for the vapor-fed water splitting devices described here, higher gas permeability and water uptake could ease the transport limitations. Also, contrary to catalyst layers in MEAs, this study implemented planar electrodes with active catalyst areas limited to the projected areas of the electrodes. Further studies should focus on nanostructuring the surface of electrocatalysts in order to significantly increase the device current output. The insights and design rules pre-

sented in this study can pave the way for the development of high current density electrolysis or solar-hydrogen reactors^{9, 17, 18, 42} that operate directly with ambient air.

Bibliography

1. S. Chu and A. Majumdar, *Nature*, 2012, **488**, 294-303.
2. N. S. Lewis and D. G. Nocera, *Proceedings of the National Academy of Sciences*, 2006, **103**, 15729-15735.
3. C. A. Rodriguez, M. A. Modestino, D. Psaltis and C. Moser, *Energy & Environmental Science*, 2014, **7**, 3828-3835.
4. B. A. Pinaud, J. D. Benck, L. C. Seitz, A. J. Forman, Z. Chen, T. G. Deutsch, B. D. James, K. N. Baum, G. N. Baum, S. Ardo, H. Wang, E. Miller and T. F. Jaramillo, *Energy & Environmental Science*, 2013, **6**, 1983-2002.
5. K. E. Ayers, E. B. Anderson, C. Capuano, B. Carter, L. Dalton, G. Hanlon, J. Manco and M. Niedzwiecki, *ECS Transactions*, 2010, **33**, 3-15.
6. M. Carmo, D. L. Fritz, J. Mergel and D. Stolten, *International Journal of Hydrogen Energy*, 2013, **38**, 4901-4934.
7. M. K. Debe, *ECS Transactions*, 2012, **45**, 47-68.
8. J. M. Spurgeon and N. S. Lewis, *Energy & Environmental Science*, 2011, **4**, 2993-2998.
9. J. Ronge, S. Deng, S. Pulinthanathu Sree, T. Bosserez, S. W. Verbruggen, N. Kumar Singh, J. Dendooven, M. B. J. Roeloffs, F. Taulelle, M. De Volder, C. Detavernier and J. A. Martens, *RSC Advances*, 2014, **4**, 29286-29290.
10. M. A. Modestino and S. Haussener, *Annual Review of Chemical and Biomolecular Engineering*, 2015, **6**, In Press.
11. K. A. Mauritz and R. B. Moore, *Chemical Reviews*, 2004, **104**, 4535-4585.
12. A. Kusoglu, M. A. Modestino, A. Hexemer, R. A. Segalman and A. Z. Weber, *ACS Macro Letters*, 2011, **1**, 33-36.
13. M. A. Modestino, A. Kusoglu, A. Hexemer, A. Z. Weber and R. A. Segalman, *Macromolecules*, 2012, **45**, 4681-4688.
14. M. A. Modestino, D. K. Paul, S. Dishari, S. A. Petrina, F. I. Allen, M. A. Hickner, K. Karan, R. A. Segalman and A. Z. Weber, *Macromolecules*, 2013, **46**, 867-873.
15. D. K. Paul, A. Fraser, J. Pearce and K. Karan, *ECS Transactions*, 2011, **41**, 1393-1406.
16. S. A. Eastman, S. Kim, K. A. Page, B. W. Rowe, S. Kang, C. L. Soles and K. G. Yager, *Macromolecules*, 2012, **45**, 7920-7930.
17. M. R. Singh, J. C. Stevens and A. Z. Weber, *Journal of The Electrochemical Society*, 2014, **161**, E3283-E3296.

18. C. Xiang, Y. Chen and N. S. Lewis, *Energy & Environmental Science*, 2013, **6**, 3713-3721.
19. A. Berger, R. A. Segalman and J. Newman, *Energy & Environmental Science*, 2014.
20. E. Kjeang, N. Djilali and D. Sinton, *J Power Sources*, 2009, **186**, 353-369.
21. E. R. Choban, L. J. Markoski, A. Wieckowski and P. J. A. Kenis, *Journal of Power Sources*, 2004, **128**, 54-60.
22. S. M. Mitrovski, L. C. C. Elliott and R. G. Nuzzo, *Langmuir*, 2004, **20**, 6974-6976.
23. J. Kuleshova, J. T. Hill-Cousins, P. R. Birkin, R. C. D. Brown, D. Pletcher and T. J. Underwood, *Electrochimica Acta*, 2011, **56**, 4322-4326.
24. M. A. Modestino, C. A. Diaz-Botia, S. Haussener, R. Gomez-Sjoberg, J. W. Ager and R. A. Segalman, *Physical Chemistry Chemical Physics*, 2013, **15**, 7050-7054.
25. P. K. Das, X. Li and Z.-S. Liu, *Journal of Electroanalytical Chemistry*, 2007, **604**, 72-90.
26. H. Ito, T. Maeda, A. Nakano and H. Takenaka, *International Journal of Hydrogen Energy*, 2011, **36**, 10527-10540.
27. M. Schalenbach, M. Carmo, D. L. Fritz, J. Mergel and D. Stolten, *International Journal of Hydrogen Energy*, 2013, **38**, 14921-14933.
28. J. Newman and K. Thomas-Alyea, *Electrochemical Systems*, Wiley & Sons, 2004.
29. A. J. Bard and L. R. Faulkner, *Electrochemical Methods, Fundamentals and Applications*, Wiley & Sons, 2000.
30. A. L. Buck, *Journal of Applied Meteorology*, 1981, **20**, 1527-1532.
31. Q. Zhao, P. Majsztrik and J. Benziger, *The journal of physical chemistry. B*, 2011, **115**, 2717-2727.
32. T. R. Marrero and E. A. Mason, *Journal of Physical and Chemical Reference Data*, 1972, **1**, 3-118.
33. J. Kestin, K. Knierim, E. A. Mason, B. Najafi, S. T. Ro and M. Waldman, *Journal of Physical and Chemical Reference Data*, 1984, **13**, 229-303.
34. A. T. Haug and R. E. White, *Journal of The Electrochemical Society*, 2000, **147**, 980-983.
35. V. A. Sethuraman, S. Khan, J. S. Jur, A. T. Haug and J. W. Weidner, *Electrochimica Acta*, 2009, **54**, 6850-6860.
36. T. Sakai, H. Takenaka and E. Torikai, *J. Electrochem. Soc.*, 1986, **133**, 1-5.

- 37. R. Nagahisa, D. Kuriya, K. Ogawa, Y. Takata and K. Ito, *ECS Transactions*, 2011, **41**, 1423-1430.
- 38. J. O. M. Bockris, A. Ammar and S. Huq, *J. Phys. Chem*, 1957, **61**, 879-886.
- 39. D. K. Paul, A. Fraser and K. Karan, *Electrochemistry Communications*, 2011, **13**, 774-777.
- 40. J. S. Chiou and D. R. Paul, *Industrial & Engineering Chemistry Research*, 1988, **27**, 2161-2164.
- 41. A. Z. Weber and J. Newman, *Journal of the Electrochemical Society*, 2004, **151**, 311-325.
- 42. S. Y. Reece, J. A. Hamel, K. Sung, T. D. Jarvi, A. J. Esswein, J. J. H. Pijpers and D. G. Nocera, *Science*, 2011, **334**, 645-648.

Chapter 7

Membrane-less electrolyzer for hydrogen production across the pH scale

The development of deployable water-splitting devices is hindered by the lack of stable ion conducting membranes that can operate across the pH scale, impose low ionic resistances and avoid product mixing. The membrane-less approach developed in this work breaks this paradigm and demonstrates for the first time an electrolyzer capable of operating with lower ionic resistance than benchmark membrane-based electrolyzers using virtually any electrolyte. Our method separates product gases by controlling the delicate balance between fluid mechanic forces in the device. The devices presented here are able to split water at current densities over 300 mA.cm^{-2} , with more than 42% power conversion efficiency, and crossover of hydrogen gas into the oxidation side as low as 0.4%, leading to a non-flammable and continuous hydrogen fuel stream. Furthermore, being able to use buffered electrolytes allows for the incorporation of earth-abundant catalysts that can only operate at moderate to high pH.

7.1 Introduction

Hydrogen gas is a clean alternative fuel which has the potential to redefine our fossil-fuel based infrastructure if its production cost reached levels competitive with conventional energy resources. As the only emission from hydrogen-based energy production is water, the adoption of this fuel can alleviate many environmental concerns. Furthermore, the use of hydrogen as a vehicle for energy storage can enable the large-scale deployment of renewable energy sources such as solar and wind which suffer from their intermittent availability. Currently, most of the hydrogen produced in the world comes from steam reforming of natural gas¹, a process that intrinsically releases at least 1 molecule of CO₂ for every 3 molecules of H₂ produced. A truly clean alternative is to use renewable energy sources, to drive water electrolysis systems and store the excess energy as H₂ fuel. State-of-the-art electrolysis systems are based on membrane electrode assemblies (MEAs) that take advantage of low ionic resistance through Nafion[®] membranes that separate the hydrogen and oxygen evolution sites²⁻⁴. Although membranes allow for production of nearly-pure gas streams and the operation of electrolyzers at high current densities, the strongly acidic nature of Nafion requires the incorporation of acid-stable catalysts that are based on noble metals, i.e. Pt and Ir⁵. The lack of stable and high-performing membranes that operate under basic and near-neutral conditions has precluded the incorporation of practical earth-abundant water splitting catalysts or photocatalytic materials into deployable devices⁶⁻¹⁴, as they have limited stability under acidic electrolytes. Research on anion-conducting membranes have led to promising alternatives for operation at high pH¹⁵⁻²¹, but their implementation in electrochemical devices lags behind Nafion. Even more complex issues arise for devices operated under near-neutral conditions^{22, 23}, where stable operation is possible only by the implementation of controlled convective flows together with ion-conduction by a supporting electrolyte²⁴. Membrane-less electrolysis can allow for the operation of devices at any pH, reduce the complexity by the elimination of separation membranes and decrease the ionic resistance thanks to the higher ion-mobility in liquid electrolytes²⁵. Membrane-less designs have been previously used in other electrochemical devices such as fuel cells²⁶⁻³³ and batteries^{34, 35}. However, there is a fundamental difference in water electrolysis where gaseous products (hydrogen and oxygen) evolve out of the liquid electrolyte. The consequent bubble formation at the electrodes is problematic as it enhances product mixing and slows down the reaction. This is a significant challenge that has precluded demonstrations of efficient membrane-less electrolyzers in the past. To mitigate gas crossover in a membrane-less scheme, fluid dynamic approaches can be implemented in order to control the position and trajectory of gas bubbles as they evolve from electrodes (Figure 7.1).

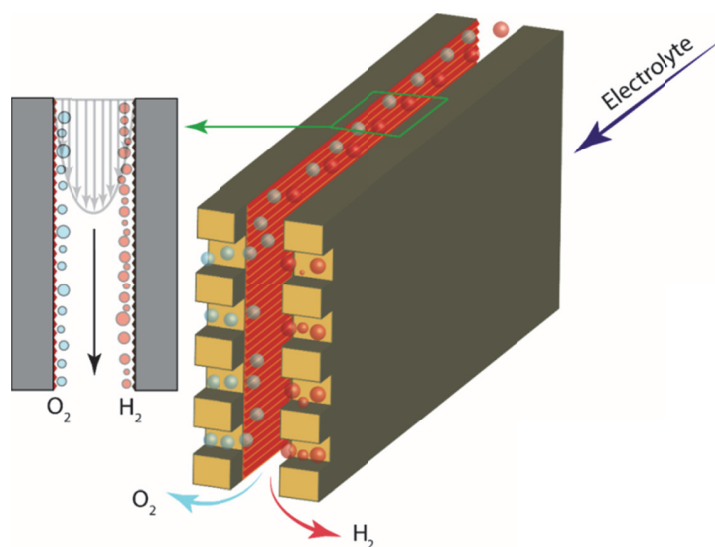


Figure 7.1. Schematic diagram of the membrane-less electrolysis: two parallel plates are coated with hydrogen and oxygen evolution catalysts, respectively and are separated by less than few hundreds of micrometers. The electrolyte flows between the catalyst plates and the evolved gases move close to the corresponding catalyst surface due to the Segré-Silberberg effect. Each of the product gas streams is collected in dedicated outlets. Stacks of these planes in horizontal can be used for higher throughput.

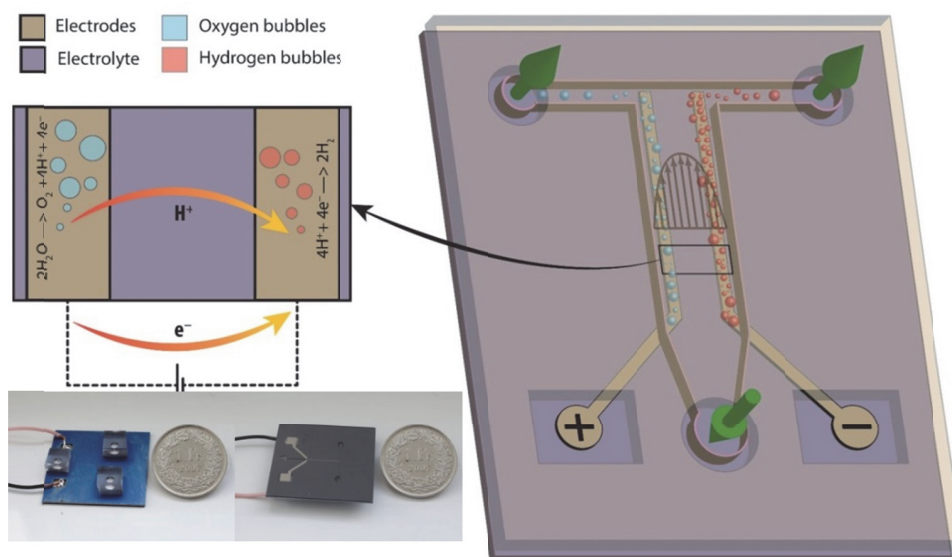


Figure 7.2. Schematic of the proof-of-concept electrolyzer design: hydrogen gas evolves at the cathode (negative electrode) and oxygen gas at the anode (positive electrode). The two gas streams do not experience any convective mixing because of the lift forces that push them towards the neighboring walls. The only mixing mechanism is diffusion of dissolved gases which is minimal at high flow rates. The inset corresponds to photographs of the fabricated device. Fluidic ports and electrical connections can be seen in the left, the electrodes and the T-junction in the right.

Previous studies on internal laminar flow of solid particles' suspensions³⁶⁻⁴⁰ have demonstrated that the particles line up at an off-center position which is velocity dependent, a phenomenon known as the Segré-Silberberg effect⁴¹. This effect is observed because the fluidic velocity gradient across the particles' body exerts a net inertial lift force on them towards the wall, which is counteracted by a force generated by the high pressure field that forms between the particles and the channel wall. The balance of these two forces determines the equilibrium position of the particles in the channel, which controls its trajectory. This phenomenon attracted enormous attention in the microfluidics community where precise control of the particles in microchannels is desirable. This effect combined with geometrically induced forces can be directly implemented in applications that require particle separation, focusing, sorting, or filtering⁴²⁻⁴⁴. Non-rigid entities such as bubbles and droplets, experience an additional lift force due to deformability which directs them away from the wall⁴⁵. This additional force causes the bubble's equilibrium position to be farther from the wall than for rigid spheres, and can only be overcome by increasing the flow rates in order to keep the bubbles away from the center of the channel.

In order to avoid gas crossover in the membrane-less electrolyzer developed here, we make use of the Segré-Silberberg effect on bubbles in the laminar flow regime. A T-junction is used to separate the gas streams at the downstream of a microchannel, after H₂ and O₂ gases are generated at electrodes placed in close proximity to the side walls. A schematic representation of the device is shown in Figure 7.2, with pictures of the fabricated device in the inset. In order to ensure a small ohmic potential drop, the inter-electrode distance in the device is kept low, at 105 μm . It is worth noting that this is the only dimension that needs to remain small in order to ensure a laminar flow that provides a steep velocity gradient for the Segré-Silberberg effect to take place. While satisfying this constraint, the electrode dimensions can be freely increased by several orders of magnitudes depending on the available technology, device design and desired application. This dimensionality constraint is equivalent to that in current state of the art electrolyzers which require a very thin MEA to provide low ionic resistivity between the oxygen and hydrogen evolving catalysts, while still allowing a large electrode area in the plane normal to the ion migration pathway. It must be noted that although this study found practical to use a microfluidic platform to explore the potential of the Segré-Silberberg effect on high-performing electrochemical water splitting devices, the principle proposed here can be scaled to devices where large-area parallel plate electrodes are implemented in order to reach high operating currents, as illustrated in Figure 7.1. In this configuration, the large-area side walls of narrow channels can be coated with appropriate catalysts to achieve higher throughput.

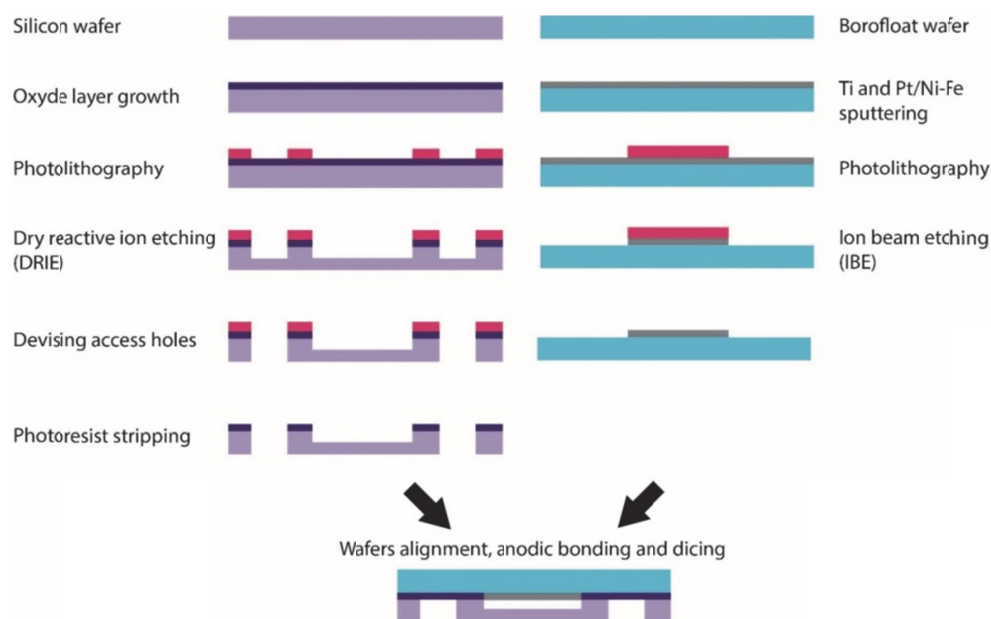


Figure 7.3. Fabrication procedure of the electrolyzer

7.2 Device fabrication

Electrodes are patterned on a Borofloat glass wafer. First, a 10 nm film of titanium is sputtered on top of the wafer to promote adhesion of 175 nm thick platinum or 150 nm thick nickel-iron top layer (81% Ni, 19% Fe). The shape of electrodes is patterned on top of platinum/Ni-Fe layer by photolithography and Ion Beam Etching (IBE) is used to etch the non-covered areas. Each electrode is 70 μm wide and 1 cm long with an edge to edge distance of 105 μm . The microchannels are etched in a photolithographically patterned silicon wafer using Deep Reactive Ion Etching (DRIE) technique. The wafer is rendered non-conductive by growing a 100 nm thick oxide layer using Low Pressure Chemical Vapor Deposition (LPCVD) before photolithography step. The depth as measured by a mechanical profilometer is 61 μm and the width of the main channel is 275 μm . The width of each branch in the T-junction is 100 μm . Fluidic and electric access holes are devised by a diamond scriber after this step. Four sets of electrodes and fluidic networks are patterned on each wafer. After plasma cleaning, the two wafers are aligned together in a Back Side Aligner (BSA) tool and bonded using standard anodic bonding technique. Distance between electrode's edge to the microchannel side wall is 15 μm . Finally, the four devices on the bonded platform are separated using a dicing machine. Small Polydimethylsiloxane (PDMS) pieces are plasma bonded on top of fluidic ports to provide a flexible bed for connections. Short wires are soldered to the electrodes ends in order

to facilitate electrical connections to the potentiostat. The fabrication process flow is shown in Figure 7.3.

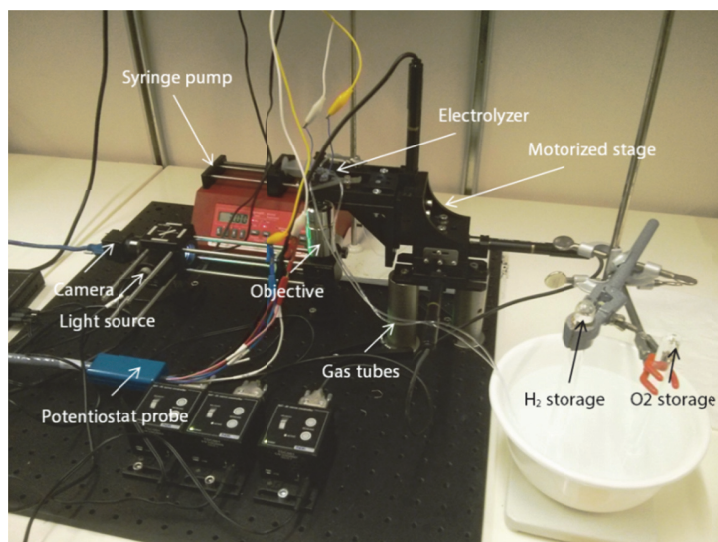


Figure 7.4. Experimental setup for electrochemical characterization and gas analysis

7.3 Experimental setup and measurements

The chip is mounted on a motorized stage and the electrolyte is provided into the chip using a syringe pump. Two tubes carry gas and electrolyte mixtures from the outlets into inverted glass tubes filled with water. The gases go up in the tubes and get trapped beneath their closed end. For volumetric measurement of the produced gases, the glass tubes are replaced by inverted 10 ml glass burettes with 20 μL graduation scale. To measure the crossover, 500 μA of current is provided to the electrodes using a potentiostat (BioLogic) for 90 minutes and then the collected gas in each tube is mixed with 10 mL of air and collected in gas tight syringes. The gases are then injected into a gas chromatographer (Bruker) for analysis. By definition, the gas crossover is the relative amount of O_2 in H_2 tube to the total amount of gas in H_2 tube. However, for practical reasons, the amount reported in this chapter is the relative amount of H_2 in O_2 tube to the total amount of H_2 in both tubes. Due to higher relative pressure of H_2 and its higher diffusion coefficient, this quantity is always larger than the classic definition and, therefore, it is a conservative measurement. A simple reflection microscope is set up next to the motorized stage which enables imaging of the chip's inside. All other electrochemical measurements are done in the same setup and the same potentiostat. Impedance spectroscopy is done in the frequency range of 10 kHz to 3 MHz. Scan rate and range for voltammetry measurements are 10 mV/s and 0 to 2.6 V, respectively. Figure 7.4 shows the experimental setup.

7.4 Results and discussions

The separation mechanism described above can be visually assessed by tracking the bubbles behavior inside the device. Snapshots of the T-junction are presented in Figure 7.5 for devices operating at different flow rates. As the flow rate increases, the size of the bubbles becomes smaller due to the larger drag force at the liquid-gas interface, while the increased inertial lift force keeps the oxygen and hydrogen bubble streams apart. These flow rate effects also fundamentally change the product mixing mechanism in the device. At low flow rates, convective mixing of bubbles migrating towards the center of the channel dominate the product crossover, while for high flow rates the diffusion of dissolved gases across the electrodes become dominant. This illustrates the important role of inertial lift force in the separation of the two gas streams at high velocities.

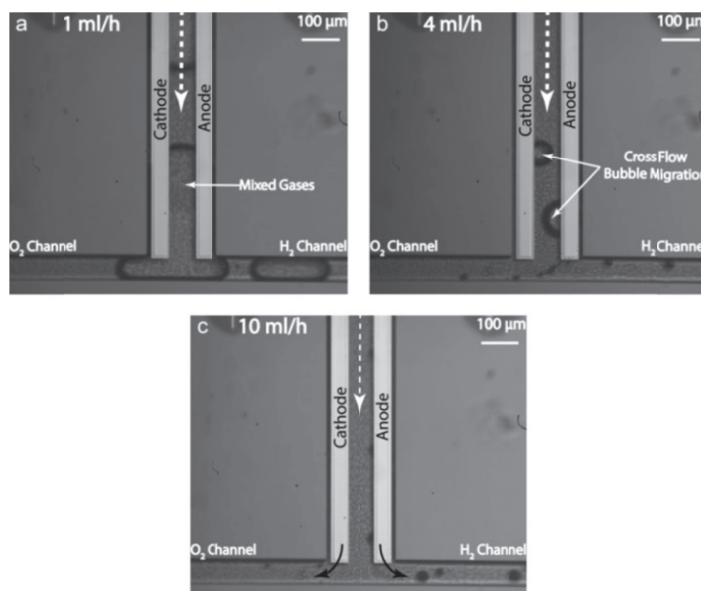


Figure 7.5. Images of the T-junction while the device is working at $143 \text{ mA} \cdot \text{cm}^{-2}$ and different flow rates. The two parallel bands are the cathode and the anode, each lying next to a side wall. a: At flow rates of 1 ml/h, the fluidic drag force is so small that the bubbles from the two electrodes grow, coalesce and move out of the device through the two outlets in a mixed form. b: At 4 ml/h, the size of the bubbles is reduced and some of them do not coalesce, although the flow speed is not enough for inertial migration to happen and keep the streams separated. c: At 10 ml/h, gas bubbles are not present in the center of the main channel and each gas stream flows into dedicated outlets. The inertial lift force is sufficient in this case to keep the bubbles close to the side walls.

Table 7.1. Measured pH values of various electrolytes utilized in the electrolyzer

Electrolyte	0.5 M H_2SO_4	1 M H_2SO_4	1.5 M H_2SO_4	2 M H_2SO_4	1 M K_2CO_3	1M Na_3PO_4 Buffer
pH	1.1	1	0.8	0.6	8.9	6.6

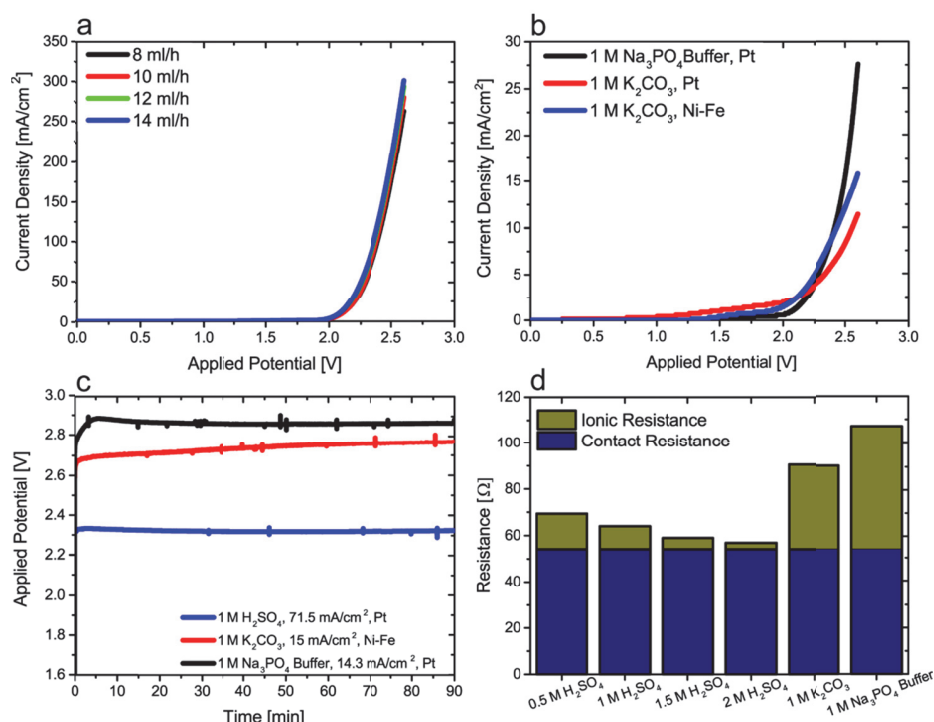


Figure 7.6. Electrochemical characterization of the microdevice. a: Current density as a function of operational voltage for 1 M sulfuric acid at different flow rates. b: J-V characteristics in 1 M Phosphate buffer and Potassium Carbonate with two different catalysts. The current density is smaller than that for acid electrolytes as platinum operates at higher efficiencies at low pH. Also, the results reveal that Ni-Fe outperforms Pt at high pH values. c: The cell voltage remains constant for more than 1.5 hours of operation in 1 M sulfuric acid, Phosphate buffer, and Potassium Carbonate for both Pt and Ni-Fe as catalyst. d: Ohmic resistance for different electrolytes obtained from impedance spectroscopy. Calculations show that the ohmic resistance in the device is mostly due to contact resistance (Section 7.5).

The membrane-less device demonstrated here shows stable operation at high current densities over the broad range of pH reported in Table 7.1. The electrochemical performance, as investigated by the device current-voltage characteristics, shows over $300 \text{ mA}/\text{cm}^2$ current density with an operating cell voltage of 2.6 V and 14 ml/h flow rate of 1 M sulfuric acid over platinum electrodes. This value can be further improved by integration of a better oxygen evolving catalyst such as iridium oxide and also nanostructuring of the flat electrodes. As presented in Figure 7.6 a, the effect of the flow rate on the current density is minimal in the range between 8 to 14 ml/h, since the fluidic drag force is high enough to detach bubbles while they are small, therefore, minimizing the mass transport limitations due to bubbles attached to the electrodes' surface. Additionally, the electrolyzer's behavior in basic and neutral pH electrolytes are shown in Figure 7.6 b for a flow rate of 12 ml/h. Operating under non-acidic electrolytes is attractive because it opens the possibility to incorporate earth

abundant catalysts. To this end, the performance of an electrolyzer with Nickel-Iron (81% Ni, 19% Fe) catalysts was also investigated and reported in Figure 7.6 b. Furthermore, the device works stably over the course of hours with different electrolytes and catalysts, as shown in Figure 7.6 c and Figure 7.7. This stable performance is even observed in a Phosphate buffer with pH of 6.6 after an initial equilibrium period of less than few minutes when ionic gradients at the surface of electrodes are expected to be formed. Lastly, it can be inferred from the potentiostatic electrochemical impedance spectroscopy (PEIS) measurements summarized in Figure 7.6 d that the losses in the system are mostly due to reaction kinetics, since ohmic losses stay well below 140 mV, with less than 22 mV arising from solution's ionic resistance at current densities up to $304 \text{ mA}\cdot\text{cm}^{-2}$. A plot of the PEIS measurements corresponding to one of the experiments is presented in Figure 7.8.

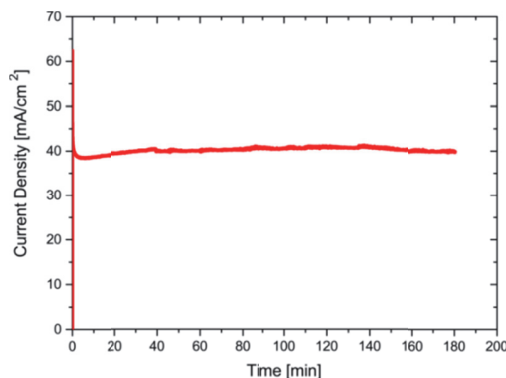


Figure 7.7. Potentiostatic measurement shows stable operation of the device over time with NiFe catalyst and 1M K_2CO_3 as electrolyte. Due to exponential dependence of current density on potential, this measurement highlights minor changes in the catalyst activity.

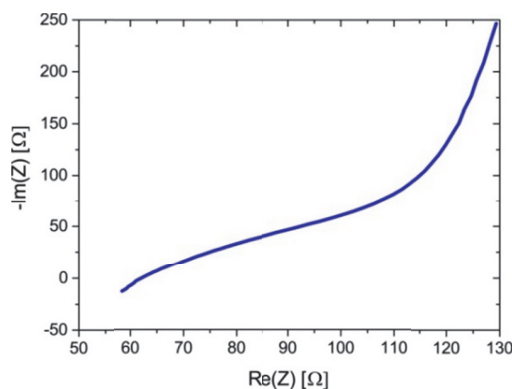


Figure 7.8. Nyquist plot of Electrochemical Impedance Spectroscopy (EIS) measurement for 1 M acidic electrolyte and flow rate of 12 ml/h.

It is worth noting that the conductivity of 1 M sulfuric acid is $0.4 \text{ S}\cdot\text{cm}^{-1}$ ⁴⁶ at 25 °C, whereas this parameter for Nafion measured in 1 M sulfuric acid at 25 °C is

reported to fall in the range between 0.08 to 0.16 S/cm⁴⁷. This difference shows that the membrane-less device would outperform in efficiency a Nafion-based analogue while still suppressing the gas crossover.

The biggest challenge with a membrane-less design is to avoid product mixing which lowers device's efficiency, product's purity and results into a potentially unsafe operation⁴⁸. Figure 7.9 a shows gas crossover measurements after running the device at 71.5 mA.cm⁻² with 1 M sulfuric acid for 90 minutes. The data are extracted from a series of chromatograms like the one in Figure 7.10. The green line shows the maximum allowable crossover to produce non-flammable gas streams, and at flow rates above 12 ml/h the cross contamination is well below this 4% cross contamination threshold. Additionally, volumetric measurements indicate collection efficiencies of up to 91% of H₂ and 93% of O₂ at the outlets of the device. The high collection efficiencies demonstrate minimal losses of the gases due to dissolution in the electrolyte and imperfections in the collection ports. This also indicates that if the electrolyte were to be recycled, the faradaic efficiency would only drop a few percentage points as a consequence of the recombination of the dissolved gases at the electrodes. At 12 ml/h and 71.5 mA.cm⁻², the ratio between convective flow of H₂ along the channel to its diffusive flow across the channel, predicted by the Peclet number, is higher than 4.7×10^3 . In addition, the ratio between the H₂ generation rate and the diffusive flow across the channel is 1.3×10^8 . These values show that the H₂ diffusion rate across the electrodes is negligible compared to generation and convective transport rate, indicating that the device is functioning in an appropriate set of operation parameters for purified fuel production, i.e. velocity and current density. The fact that the measured gas crossover is higher than these predicted values suggests that gas mixing in the devices predominantly happens through perturbations that cause convective transport of bubbles across the channel. These perturbations also lead to instabilities in the device electrochemical performance, especially at lower flow rates as observed in Figure 7.9 b. When devices operate at low flow rates, bubbles fill the inter-electrode space, increasing the ionic resistance in the device and resulting in fluctuations in the applied potential required to maintain a constant current density. At higher flow rates, the migration of bubbles across the channels is reduced and the ionic resistance between the two electrodes remains constant, resulting in stable operation. It should be noted that requiring high flow rates for gas separation increases the energy required for pumping the fluids. However, the pumping power requirement is estimated to be only 5% of the generated power when the device is operated at 71.5 mA.cm⁻² and 12 ml/h (Section 7.5). These low levels of pumping power can be further reduced by optimizing the channel dimensions in the device.

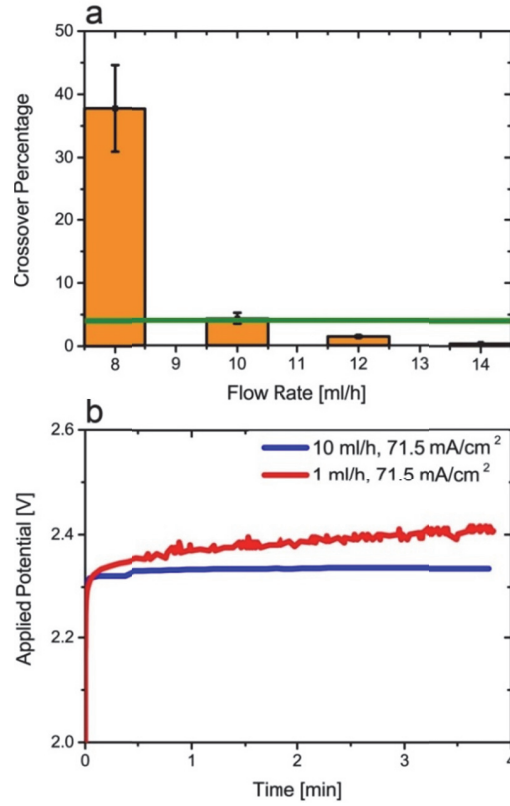


Figure 7.9. a: Gas crossover as a function of flow rate at 71.5 mA/cm^2 . As the flow rate increases the mixing mechanism changes from convection of bubbles to diffusion of dissolved gases. Larger drag force reduces the size of bubbles while the inertial lift force keeps the two bubble streams apart at the same time. b: At low flow rates, the cell voltage fluctuates in order to keep the current density constant. This is due to the changing ionic resistance as the gases displace the electrolyte in the center of the channel.

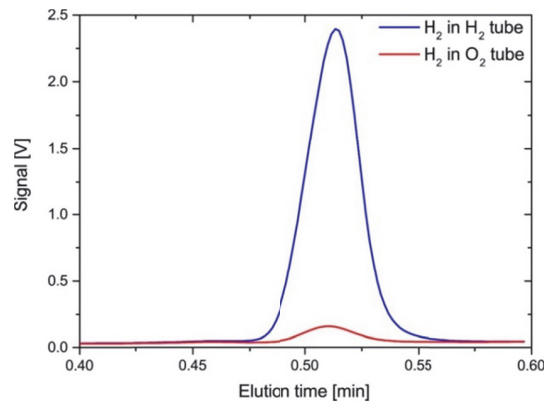


Figure 7.10. Chromatogram of the stored gases for 10 ml/h flow rate and 71.5 mA/cm^2

7.5 Calculations

For calculation of solution resistance, the following formula is utilized:

$$R = \frac{L}{\kappa A}$$

Where κ is the specific conductivity of 1 M sulfuric acid at 25 °C, L is the distance between furthest edges of the electrodes (245 μm) and A is the area where ionic transport happens (61 μm by 1 cm).

The pressure drop can be found for a rectangular channel with aspect ratio – width to height – less than one and Reynolds number less than 1000 within 0.26% accuracy using the following formula:

$$\Delta p = QR$$

Where Q is the volumetric flow rate and $R = \frac{a\mu L}{WH^3}$, is the fluidic resistance. a is a dimensionless parameter depending on the width (W) to height (H) ratio of the channel⁴⁹, W/H :

$$a = 12 \left[1 - \frac{192H}{\pi^5 W} \tanh\left(\frac{\pi W}{2H}\right) \right]^{-1}$$

In the fabricated electrolyzer, aspect ratio is 0.22 and Reynolds number is 19.8 for 12 ml/h flow rate. Therefore, the pressure drop equals 7.4 kPa at this flow rate assuming viscosity and density for water at 20 °C i.e. 1 mPa.s and 1000 kg/m³. It is worth noting that this value is for single phase flow and may differ slightly from the pressure drop for bubbly flow. Assuming a pump efficiency of 75%, the input power, P_i delivered to the pump will be 0.033 mW. In other words, pumping power is 2.5 or 5% of the produced hydrogen power if the device runs at 143 or 71.5 mA/cm², respectively. The overall efficiency, η , at 12 ml/h is:

$$\eta = \frac{1.23V I - P_i}{V_{cell} I}$$

Where I is the electric current passing through the device and V_{cell} is the operational cell voltage. For instance, the efficiency is 51% for 71.5 mA/cm² of current and 12 ml/h of flow rate.

Peclet number:

$$Pe = \frac{UL}{D}$$

Where U is the average fluidic velocity, L is the characteristic length over which the diffusion occurs, and D is diffusion coefficient for Hydrogen. This number is the lowest possible ratio of convective to diffusive transport in the device since

most of the gases are carried away in the gas phase and not in the dissolved form.

Ratio between H_2 generation rate to diffusive transport across the channel:

$$\frac{J_{gen}}{J_{diff}} = \frac{\frac{I}{zF}}{\frac{DC}{L} L_c H_c} = \frac{LI}{zFDC L_c H_c}$$

Where I is the current, z is the valency number of ions, F is the Faraday constant, L_c and H_c are the length and height of the channel, respectively.

For comparison with the volumetric gas measurements, ideal gas law is used to calculate the volume of the gases produced, assuming all of the current is spent on generating gaseous products, i.e. H_2 and O_2 . With 0.5 mA current, the rate of hydrogen gas generation should be 2.59 nM/s or 18.65 μmol in two hours run of volumetric measurement. Using this value together with the standard conditions of 101.325 kPa and 293.15 K into ideal gas equation of state, $PV = nRT$, leads to a volume of 449 μL for Hydrogen gas. Ideally, the volume of Oxygen should be 224.5 μL . The experimental values obtained here show up to 410 μL of H_2 and 210 μL of O_2 with reading resolution of 10 μL . These amounts show collection efficiencies above 90%.

7.6 Conclusions

The membrane-less electrolyzer demonstrated here has the ability to produce non-flammable hydrogen streams, continuously and stably across the pH scale. Comparing the device ohmic resistance with that for Nafion-based devices, it is clear that this device has the potential to surpass the performance of similar water splitting apparatus that rely on ion conductive membranes for separation. Although a single electrode pair, such as the one in this proof of concept study, can only produce a limited amount of fuel, scaling it out can be achieved on multi-stack panels for enhanced throughput⁵⁰ or the implementation of large area electrodes. As the only dimension to be kept small is the inter-electrode distance, follow up studies are underway to develop high throughput devices where high surface area planar electrodes are used as the side walls of narrow electrolyte channels. Additionally, it is worth noting that this electrolyzer platform may be used in reverse as a fuel cell with two streams of the electrolyte, each saturated with H_2 or O_2 , allowing for the production of electricity⁵¹. The design simplicity of this membrane-less electrolyzer can facilitate mass production, especially by employing high resolution 3D printers or injection moulding techniques.

Bibliography

1. R. M. Navarro, M. A. Pena and J. L. G. Fierro, *Chem Rev*, 2007, **107**, 3952-3991.
2. M. K. Debe, *Nature*, 2012, **486**, 43-51.
3. K. E. Ayers, E. B. Anderson, C. Capuano, B. Carter, L. Dalton, G. Hanlon, J. Manco and M. Niedzwiecki, *ECS Transactions*, 2010, **33**, 3-15.
4. S. Holdcroft, *Chemistry of Materials*, 2013.
5. C. C. L. McCrory, S. Jung, J. C. Peters and T. F. Jaramillo, *Journal of the American Chemical Society*, 2013, **135**, 16977-16987.
6. D. G. Nocera, *Accounts of Chemical Research*, 2012, **45**, 767-776.
7. T. A. Faunce, W. Lubitz, A. W. Rutherford, D. MacFarlane, G. F. Moore, P. Yang, D. G. Nocera, T. A. Moore, D. H. Gregory, S. Fukuzumi, K. B. Yoon, F. A. Armstrong, M. R. Wasielewski and S. Styring, *Energy & Environmental Science*, 2013, **6**, 695-698.
8. N. S. Lewis and D. G. Nocera, *Proceedings of the National Academy of Sciences*, 2006, **103**, 15729-15735.
9. M. G. Walter, E. L. Warren, J. R. McKone, S. W. Boettcher, Q. Mi, E. A. Santori and N. S. Lewis, *Chemical reviews*, 2010, **110**, 6446-6473.
10. S. Y. Reece, J. A. Hamel, K. Sung, T. D. Jarvi, A. J. Esswein, J. J. H. Pijpers and D. G. Nocera, *Science*, 2011, **334**, 645-648.
11. P. W. Du and R. Eisenberg, *Energ Environ Sci*, 2012, **5**, 6012-6021.
12. Q. S. Yin, J. M. Tan, C. Besson, Y. V. Geletii, D. G. Musaev, A. E. Kuznetsov, Z. Luo, K. I. Hardcastle and C. L. Hill, *Science*, 2010, **328**, 342-345.
13. C. R. Cox, J. Z. Lee, D. G. Nocera and T. Buonassisi, *Proceedings of the National Academy of Sciences*, 2014, **111**, 14057-14061.
14. J. Luo, J.-H. Im, M. T. Mayer, M. Schreier, M. K. Nazeeruddin, N.-G. Park, S. D. Tilley, H. J. Fan and M. Grätzel, *Science*, 2014, **345**, 1593-1596.
15. G. Sudre, S. Inceoglu, P. Cotanda and N. P. Balsara, *Macromolecules*, 2013.
16. P. Cotanda, G. Sudre, M. A. Modestino, X. C. Chen and N. P. Balsara, *Macromolecules*, 2014.
17. G. Merle, M. Wessling and K. Nijmeijer, *Journal of Membrane Science*, 2011, **377**, 1-35.
18. G. Couture, A. Alaaeddine, F. Boschet and B. Ameduri, *Progress in Polymer Science*, 2011, **36**, 1521-1557.
19. C. Jangu and T. E. Long, *Polymer*, 2014, **55**, 3298-3304.

20. K. J. T. Noonan, K. M. Hugar, H. A. Kostalik, E. B. Lobkovsky, H. D. Abruña and G. W. Coates, *Journal of the American Chemical Society*, 2012, **134**, 18161-18164.
21. Y. Ye, K. K. Stokes, F. L. Beyer and Y. A. Elabd, *Journal of Membrane Science*, 2013, **443**, 93-99.
22. E. A. Hernandez-Pagan, N. M. Vargas-Barbosa, T. Wang, Y. Zhao, E. S. Smotkin and T. E. Mallouk, *Energy & Environmental Science*, 2012, **5**, 7582-7589.
23. J. Jin, K. Walczak, M. R. Singh, C. Karp, N. S. Lewis and C. Xiang, *Energ Environ Sci*, 2014, **7**, 3371-3380.
24. M. A. Modestino, K. A. Walczak, A. Berger, C. M. Evans, S. Haussener, C. Koval, J. S. Newman, J. W. Ager and R. A. Segalman, *Energy & Environmental Science*, 2014, **7**, 297-301.
25. J. Newman, *Journal of the Electrochemical Society*, 2013, **160**, F309-F311.
26. R. Ferrigno, A. D. Stroock, T. D. Clark, M. Mayer and G. M. Whitesides, *J Am Chem Soc*, 2002, **124**, 12930-12931.
27. E. R. Choban, L. J. Markoski, A. Wieckowski and P. J. A. Kenis, *Journal of Power Sources*, 2004, **128**, 54-60.
28. R. S. Jayashree, L. Gancs, E. R. Choban, A. Primak, D. Natarajan, L. J. Markoski and P. J. A. Kenis, *J Am Chem Soc*, 2005, **127**, 16758-16759.
29. F. R. Brushett, W. P. Zhou, R. S. Jayashree and P. J. A. Kenis, *Journal of The Electrochemical Society*, 2009, **156**, B565-B571.
30. N. Da Mota, D. A. Finkelstein, J. D. Kirtland, C. A. Rodriguez, A. D. Stroock and H. D. Abruna, *J Am Chem Soc*, 2012, **134**, 6076-6079.
31. E. Kjeang, R. Michel, D. A. Harrington, N. Djilali and D. Sinton, *Journal of the American Chemical Society*, 2008, **130**, 4000-4006.
32. E. Kjeang, B. T. Proctor, A. G. Brolo, D. A. Harrington, N. Djilali and D. Sinton, *Electrochim Acta*, 2007, **52**, 4942-4946.
33. J. L. Cohen, D. A. Westly, A. Pechenik and H. D. Abruna, *J Power Sources*, 2005, **139**, 96-105.
34. W. A. Braff, M. Z. Bazant and C. R. Buie, *Nature Communications*, 2013, **4**.
35. Y. Yang, J. Loomis, H. Ghasemi, S. W. Lee, Y. J. Wang, Y. Cui and G. Chen, *Nano Letters*, 2014.
36. G. Segre and A. Silberberg, *J Fluid Mech*, 1962, **14**, 115-135.
37. G. Segre and A. Silberberg, *J Fluid Mech*, 1962, **14**, 136-157.
38. J. A. Schonberg and E. J. Hinch, *J Fluid Mech*, 1989, **203**, 517-524.
39. J. B. McLaughlin, *J Fluid Mech*, 1991, **224**, 261-274.
40. J. B. McLaughlin, *J Fluid Mech*, 1993, **246**, 249-265.

41. G. Segre and A. Silberberg, *Nature*, 1961, **189**, 209-&.
42. A. A. S. Bhagat, S. S. Kuntaegowdanahalli and I. Papautsky, *Phys Fluids*, 2008, **20**.
43. D. Di Carlo, *Lab Chip*, 2009, **9**, 3038-3046.
44. S. S. Kuntaegowdanahalli, A. A. S. Bhagat, G. Kumar and I. Papautsky, *Lab Chip*, 2009, **9**, 2973-2980.
45. H. Amini, W. Lee and D. Di Carlo, *Lab on a Chip*, 2014, **14**, 2739-2761.
46. H. E. Darling, *Journal of Chemical & Engineering Data*, 1964, **9**, 421-426.
47. S. Slade, S. A. Campbell, T. R. Ralph and F. C. Walsh, *Journal of The Electrochemical Society*, 2002, **149**, A1556-A1564.
48. A. Berger, R. A. Segalman and J. Newman, *Energ Environ Sci*, 2014, **7**, 1468-1476.
49. M. J. Fuerstman, A. Lai, M. E. Thurlow, S. S. Shevkoplyas, H. A. Stone and G. M. Whitesides, *Lab Chip*, 2007, **7**, 1479-1489.
50. K. S. Elvira, X. C. I. Solvas, R. C. R. Wootton and A. J. deMello, *Nat Chem*, 2013, **5**, 905-915.
51. J. L. Cohen, D. J. Volpe, D. A. Westly, A. Pechenik and H. D. Abruna, *Langmuir*, 2005, **21**, 3544-3550.

Chapter 8

Membrane-less micro fuel cell based on two-phase flow

Most microfluidic fuel cells use highly soluble fuels and oxidants in streams of liquid electrolytes to overcome the mass transport limitations that result from the low solubility of gaseous reactants such as hydrogen and oxygen. In this work, we address these limitations by implementing controlled two-phase flows of these gases in a set of microchannels electrolytically connected through a narrow gap. Annular flows of the gases reshape the concentration boundary layer over the surface of electrodes and increase the mass-transport limited current density in the system. Our results show that the power density of a two-phase system with hydrogen and oxygen streams is an order of magnitude higher than that of single phase system consisting of liquid electrolytes saturated with the same reactants. The reactor design described here can be employed to boost the performance of MFCs and put them in a more competitive position compared to conventional fuel cells.

8.1 Introduction

Close to two centuries have passed since the first reports of hydrogen fuel cells¹. These interesting early power generators did not reach practical use until recently due to various technical, social, political, and economic reasons. Driven by environmental factors, hydrogen fuel-cell vehicles have regained attention, and are commercially available today^{2, 3}. Portable electronics is another sector with high potential for fuel cells, given the possibility of achieving higher power densities than batteries. Implementation in this sector requires the development of light weight and compact fuel-cells. Micro fuel cells are a class of power sources that can address these requirements⁴⁻⁹. Additionally, their compatibility with semiconductor manufacturing processes makes micro fuel cells a promising power source for consumer electronics.

An interesting group of micro fuel cells are microfluidic fuel cells (MFCs) that allow for the implementation of laminar co-flow of an oxidant and a fuel stream parallel to each other. In this configuration, mixing can only happen through diffusion at their interface between the streams¹⁰⁻¹⁴. If the flow is fast enough, i.e. high Péclet number regime, this diffusion is negligible and does not affect the performance; even without implementing separation membranes. Developing fuel cells without membranes would reduce the cost, size and weight of the device. It can also lead to a better performance compared to conventional fuel cells as liquid electrolytes have higher ionic conductivity than solid-state ones. Despite these advantages, membrane-less devices face significant hurdles since the fuel and oxidant need to be dissolved into liquid electrolytes. Promising clean fuels such as hydrogen have very low solubility in liquid electrolytes ($< 0.8 \text{ mol m}^{-3}$ at standard conditions), which introduces significant mass transport limitations and restricts the peak power density to less than 1 mW/cm^2 ^{15, 16}. In order to address this problem, alternative chemicals with high solubility in liquid electrolytes can be implemented. Kjeang et al. demonstrated that by flowing aqueous vanadium redox species through porous electrodes, power densities as high as 131 mW/cm^2 can be achieved. The two streams pass through highly porous electrodes with numerous catalytic active sites and enter a microchannel where they flowed parallel to each other and exit the chip downstream¹⁷. An improved cell design has been shown to provide power densities as high as 330 mW cm^{-2} ¹⁸. Da Mota et al. used borohydride and cerium ammonium nitrate as fuel and oxidant in a cell where the electrodes were deposited on plates with herringbone structures to induce chaotic mixing close to the electrodes surfaces and improve mass transport. In order to prevent the fuel and oxidant crossover, they integrated a $10 \text{ }\mu\text{m}$ porous separator into the device and achieved a peak power of 250 mW cm^{-2} ¹⁹. Despite these promising demonstrations, use of high energy-density and economically viable fuels such as hydrogen in these devices can po-

tentially promote their deployment. In this study, we revisit hydrogen as a fuel and devise an approach that mitigates the mass transport limitations that has restricted the development of high power density hydrogen MFCs. In order to go beyond the saturation limit of gases in liquid electrolytes, two-phase flows will need to be considered. Implementing two-phase flows, requires the conception of a mechanisms to introduce and maintain separate H_2 and O_2 gas streams with minimal level of mixing. Furthermore, these gaseous streams will need to be encapsulated in a continuous ionically conductive phase, i.e. liquid electrolyte. Under this configuration, gas crossover would only occur via diffusion, and as far as the stream velocity is high, mixing between the two gas streams would be negligible. In the following sections, we describe a method that satisfies all of these conditions and allowed for the demonstration of a proof-of-concept device that delivers one order of magnitude higher power density compared to its single phase counterpart. Such a method can be implemented in other electrochemical systems where mass transfer is a major performance barrier.

8.2 Working principle

It is known that droplets and bubbles confined to microchannels adapt their morphology to minimize their surface energy. This property has been used to trap or guide these deformable entities into cavities or rails at the walls of microchannels²⁰⁻²⁴. Making use of this principle, two streams of H_2 and O_2 gas inside electrolyte are confined to two separated microchannels connected by a shallow ionic bridge. The elongated bubbles are surrounded by the liquid electrolyte which fills in the shallow mid channel as well. The top wall of each gas channel is covered by a thin platinum electrode where the gases can diffuse to their surface through the very thin liquid film wetting the hydrophilic channels walls. In this way, the bubbles act as reservoirs of fuel and oxidant feeding the thin liquid layer that separates the gas streams from the electrodes. Furthermore, the protons can move freely in this layer and reach the cathode through the shallow gap. A three dimensional illustration of this structure is provided in Figure 8.1. It is worth noting that a similar channel profile has been previously used in an MFC with formic acid as fuel and potassium permanganate as oxidant in order to reduce the cross-diffusion area between oxidant and fuel streams²⁵.

8.3 Analytical and Numerical Model

To gain insights into the expected mass-transport enhancement from a two-phase configuration over single phase one, a simple analytical model has been developed for the former and a 3D numerical model in COMSOL for the latter. In both cases, only mass transport limitations have been taken into account, as

they are expected to be the dominant source of losses at maximum current density which is dictated by the maximum mass flux of reactants towards the surface of the electrodes.

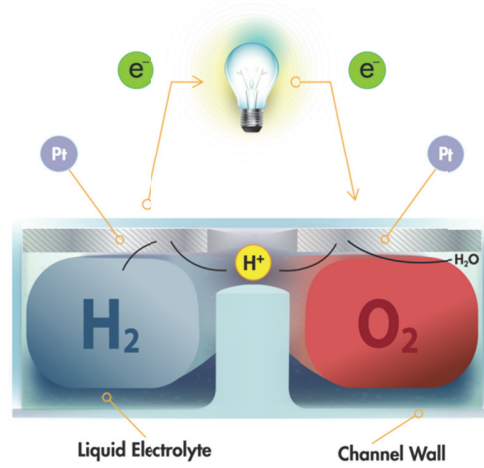


Figure 8.1. Schematic representation of the two-phase flow concept in a membraneless fuel cell.

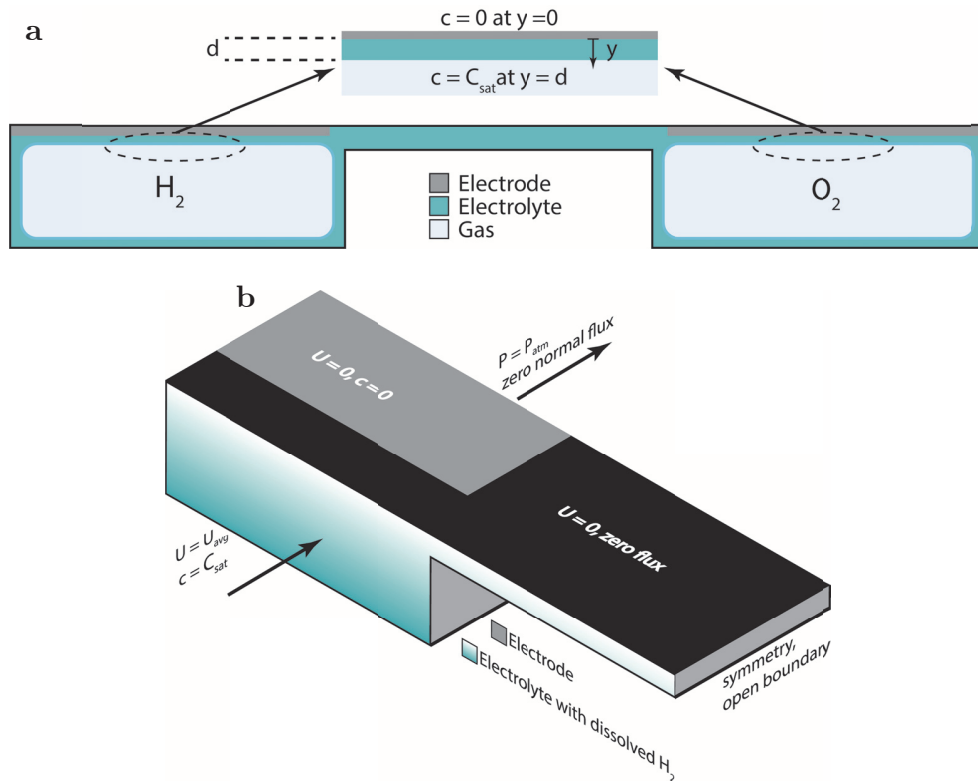


Figure 8.2. a) Schematic of the cell cross section for the two-phase configuration and the boundary conditions for the diffusion equation. Approximate determination of the liquid film thickness is provided in the supporting information. b) 3D schematic of the modeled geometry with applied boundary conditions. U_{avg} is the average velocity and P_{atm} the atmospheric pressure.

For the two-phase case, the mass transport inside the thin liquid electrolyte film is assumed to be one dimensional and diffusion dominated. Under these conditions, the mass transport of gases can be described by,

$$\frac{\partial c}{\partial t} = D \frac{\partial^2 c}{\partial y^2}$$

Where c , t , D , and y are the concentration of species, time, diffusion coefficient, and spatial coordinate in the cross flow direction, respectively. At steady state, the solution to this equation, subject to a zero concentration of reactant at the surface of the electrode (Figure 8.2a), is linear and in the form of $c(y) = \frac{C_{\text{sat}}}{d} y$, where d corresponds to the thickness of liquid film and C_{sat} to the equilibrium concentration of species at the gas/liquid interface. Assuming a uniform Fickian diffusion over the electrode's area, the average flux of species for the two-phase case can be estimated to be $D \frac{C_{\text{sat}}}{d}$. Assuming equal average velocities for the gas and liquid phases in the annular flow (i.e. homogeneous conditions) the liquid film thickness, d , can be calculated. The homogeneity condition for elongated bubbles in rectangular channels has been observed before²⁶. Based on this assumption, the ratio of gas flow rate to the total flow rate equals the ratio of the portion of cross section occupied by the gas to the total channel cross section:

$$\frac{A_{\text{gas}}}{A_{\text{total}}} = \frac{Q_{\text{gas}}}{Q_{\text{total}}} \rightarrow \frac{(135 - 2d)(50 - 2d)}{135 \times 50} = \alpha$$

In above equation, α equals to 0.89, 0.94, and 0.97 for 4, 8, and 16 ml/h of gas flow rates, respectively. The liquid electrolyte in the half cell is 0.5 ml/h. Simplifying above equation leads to a hyperbolic equation based on d which has the solutions reported for each flow rate in Table 8.1.

The values for D and C_{sat} for H_2 are used in the calculations since it is the transport limited reactant. In other words, the product of DC_{sat}/n for hydrogen in water at 25°C is $1.75 \times 10^{-9} \text{ mol m}^{-1} \text{ s}^{-1}$ versus $2.6 \times 10^{-9} \text{ mol m}^{-1} \text{ s}^{-1}$ for oxygen, where n is the number of moles for each reactant in the overall reaction, i.e. $2\text{H}_2 + \text{O}_2 \rightarrow \text{H}_2\text{O}$.

The 3D model is developed for half of the cell subject to a zero concentration of reactant at the surface of the electrode as depicted in Figure 8.2b. The problem is solved in COMSOL by coupling laminar flow and transport of dilute species modules. The average mass flux over the electrode is calculated from the results and given in Table 8.1 for comparison with experimental results. The general trend shows that a short circuit density enhancement between 500 to 1100% is expected depending on the flow rates used.

8.4 Experimental section

8.4.1 Device architecture and fabrication

The fluidic channels were dry etched into a double sided silicon wafer with one micron of wet oxide layer on both sides acting as mask for the etching process. The process involves two photolithography steps on the front side and one on the backside for fluidic ports and electrical connection holes. At the end of the process, the initial oxide layer was removed in an HF bath and a new 170 nm dry oxide layer was grown to render the surface hydrophilic and electrically insulating. There are six fluidic ports on the device: two for introducing the liquid electrolyte, two for gas injection, and the last two as the outlet. The 170 nm thick Pt electrodes are patterned on a Pyrex wafer using photolithography and ion beam etching. A 10 nm Ti seed layer was deposited prior to Pt sputtering to promote adhesion. The two wafers were then cleaned, aligned, and bonded anodically. The detailed procedure is shown in Figure 8.3.

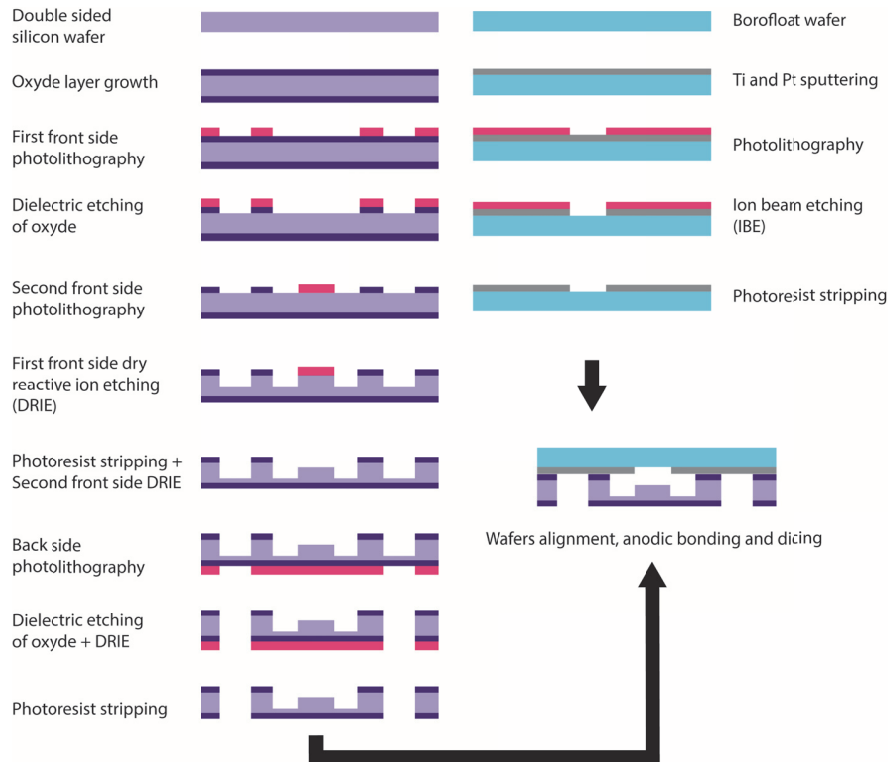


Figure 8.3 The fabrication procedure of the micro fuel cells: microchannels on the silicon wafer (left side) and electrodes on the Borofloat wafer (right side). The two wafers are aligned and anodically bonded together in the last step.

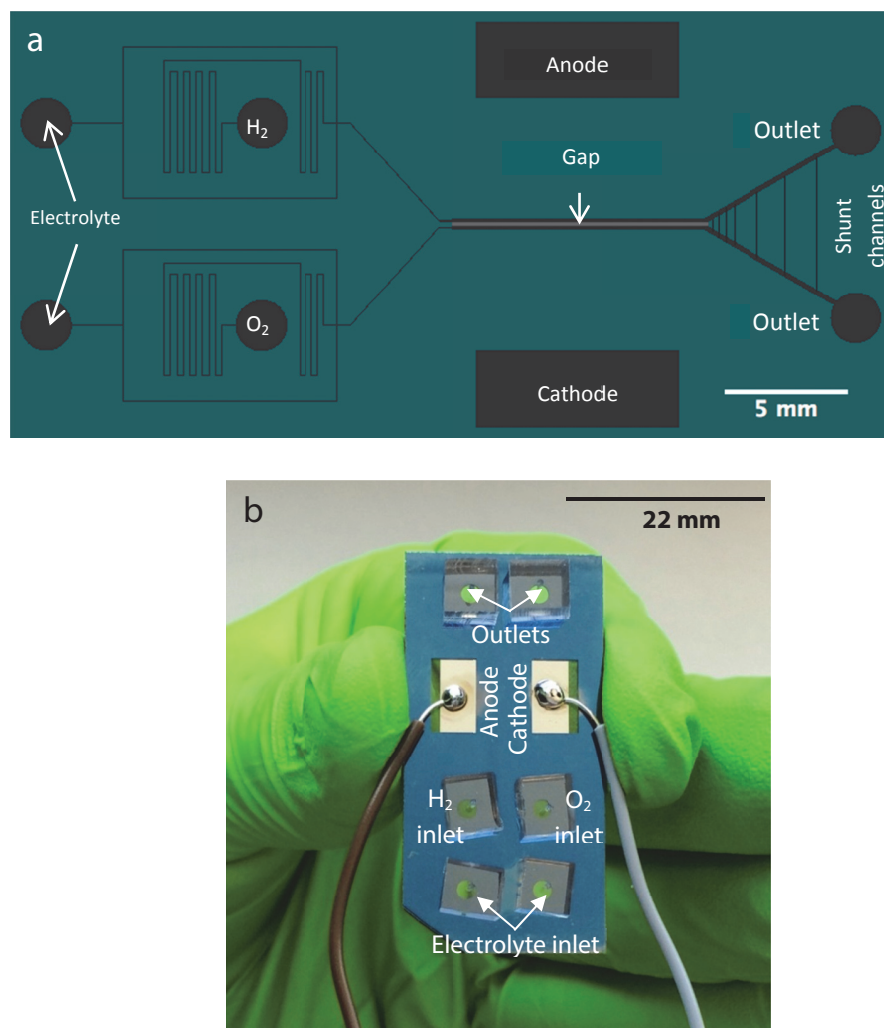


Figure 8.4. a) Top view of the fluidic microchannels layout in a micro fuel cell. b) Photograph of a representative MFC. PDMS pieces provide a flexible bed for introduction of electrolyte, fuel and oxidant streams. Anode and cathode connections to the potentiostat are established through conductive wires soldered to the Pt electrodes.

The widths and depths of the two deep channels are 135 and 50 μm respectively and the width and depth of the connecting gap is 130 and 10 μm , respectively. The elongated gas bubbles contained in the liquid phase are generated in a cross junction upstream before entering the main channel. The length of all channels is 1 cm out of which 5 mm are covered with the platinum electrodes and the rest are used as a transparent window for visual inspection. The layout of the fluidic channels is shown in Figure 8.4a. The main channels end up into a Y shaped bifurcation separating the oxidant and fuel flows downstream. Several narrow shunt channels were introduced to balance the pressure between the two outlet channels²⁷. This ensures no clogging by bubbles at the outlets as can be

seen from Figure 8.7b. The platinum electrodes are 5 mm long and 120 μm wide and the gap between the two is 160 μm . This accounts for an active electrode area over the channels of 0.006 cm^2 .

There are six cells on each pair of wafers (Figure 8.5) which are diced and used individually for measurements. After dicing, PDMS pieces with punched holes are bonded on top of fluidic ports to provide a flexible bed for tubing and electrical wires are soldered to the open area of Pt electrodes in order to connect the device to a potentiostat for characterization as depicted in Figure 8.4b.

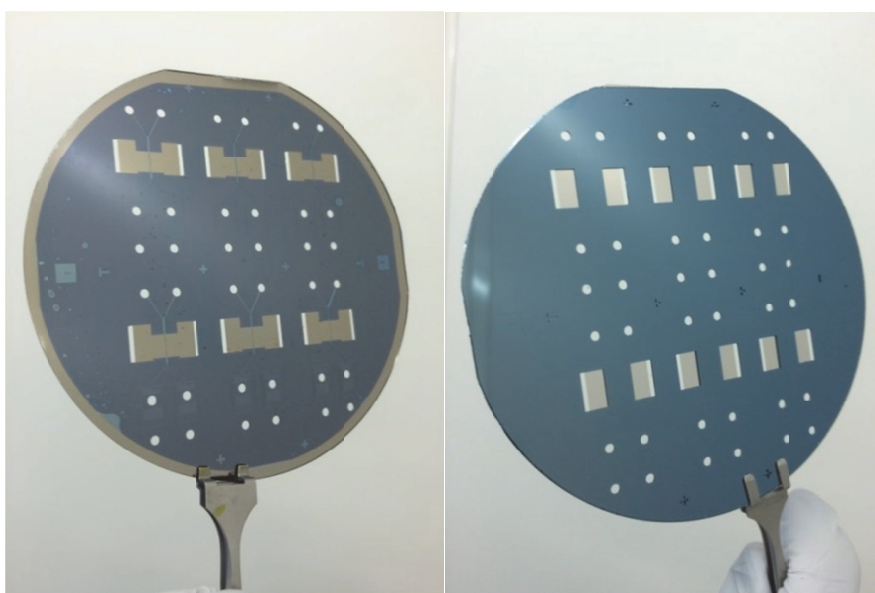


Figure 8.5. Front side view (left) and back side view (right) of the final bonded wafers. There are six cells on each set of wafers which are diced and tested individually.

8.4.2 Experimental set-up and characterization

The two electrolyte inlets are connected to two plastic syringes from Becton Dickinson filled with 1 M sulfuric acid and mounted on a dual syringe pump (Cronus Sigma 2000). The two gas inlets are connected to two gas tight syringes from SGE Analytical Science, each filled with pure hydrogen and oxygen and mounted on a similar pump. The outlets are drained into a beaker using tubes of the same size. For the single phase measurements, the gas inlet tubes are blocked by a clipper and the electrolytes in each syringe is saturated with hydrogen and oxygen prior to the measurements by bubbling each gas through 1 M sulfuric acid solutions placed in separate containers for 15 minutes. Prior to this saturation process, the electrolyte was bubbled with N_2 to eliminate traces of O_2 from ambient air.

In the case of two-phase measurements, the operation of the devices is visualized using an optical microscope in reflection mode. A fast camera (Photron's FASTCAM Mini UX100) is used for capturing videos at high frequencies.

The electrochemical characterization is performed using a VSP-300 Biologic Potentiostat. The measurements are done at three different flow rates for both single phase and two-phase cases. In order to have a fair comparison, the total flow rate for the two gases in the two-phase system is set equal to the total flow rate for the liquid electrolyte in the single phase case. In the two-phase case, the liquid electrolyte's flow rate is kept constant at the small value of 1 ml h^{-1} to provide ion conduction between the two electrodes. Unlike the single phase case, this stream is not saturated with any of the gases before flowing into the chip.

8.5 Results and discussion

As explained above, the main purpose of this study is to mitigate the mass transport limitations in MFCs, which arise from the low solubility of hydrogen and oxygen in liquid electrolytes. In order to achieve this, a two-phase flow MFC with two annular flows of each gas, i.e. H_2 and O_2 , in a liquid electrolyte was developed. Under this configuration, mass transport models suggests that the maximum power density can be enhanced by up to a factor of 11 for a fuel/oxidant flow rate of 16 ml hr^{-1} , when going from single phase to two-phase operation. To provide insights on the mass transport limitations for a one phase device, the mass flux maps together with the concentration boundary layers over the electrode are depicted in Figure 8.6. Furthermore, the average values of flux are reported in Table 8.1 for comparison with the analytical values obtained for the two-phase case. Figure 8.6a to 4c show that the mass flux is highly non-uniform when we move along the electrodes and drops quite rapidly in the first few hundreds of microns. This clearly demonstrates that the single phase device suffers significantly from the lack of reactants at the vicinity of the electrode's surface, and the average mass flux drops drastically as a function of electrode distance (Figure 8.6e and f). This is in contrast with the two-phase case where the mass flux is expected to remain approximately uniform throughout the length of the electrode, making the two-phase device intrinsically scalable.

To experimentally demonstrate the potential of the proposed MFC architecture, devices were fabricated and characterized under various operating conditions. The top view of the device during operation is shown in Figure 8.7, both at the inlet and outlet of the cell. These images show that the elongated bubbles are confined to their corresponding channels and do not enter the narrow gap in between. This is due to the fact that entering this region will increase the surface energy of the gas bubbles and, therefore, is thermodynamically unfavorable.

Figure 8.7 demonstrates that the flow inside the channels is approaching an annular profile. Within this flow profile, gas transport towards the electrodes can be enhanced as molecules only need to diffuse through a thin layer of electrolyte covering the electrodes; at the same time the ionic resistance can be high, as ions are restricted to migrate through this thin film of electrolyte. The potentiostatic electrochemical impedance spectroscopy (PEIS) measurements show only a $\sim 28 \Omega$ difference between the resistivity of the two device configurations. This is likely caused by the in-plane electrode architecture of the cells where most of the current is expected to pass through the inner edges of the electrodes, and the ionic conductivity of the device is defined by the shallow gap connecting the two channels. Since this gap is the same for both the single and two-phase cases, the conductivity values are not expected to differ significantly. The negligible difference between the cells resistivity, $\sim 3 \Omega$, operating at different gas flow rates in the two-phase case is another indication that most of the current passes through the electrodes closest edges. At larger gas flow rates, the electrolyte film thickness is smaller and, therefore, the ionic conductivity is expected to be smaller. At low currents and overpotentials, the reaction is expected to take place mostly at the inner edges of the electrodes because the losses will be dominated by the electrolyte resistance. As the current increases, its distribution over the surface of electrodes becomes more uniform since the overpotential losses increase and become comparable to the ohmic losses. These asymmetries in the current density distribution would lead to an ionic resistance that is highly dependent on the overall operating current.

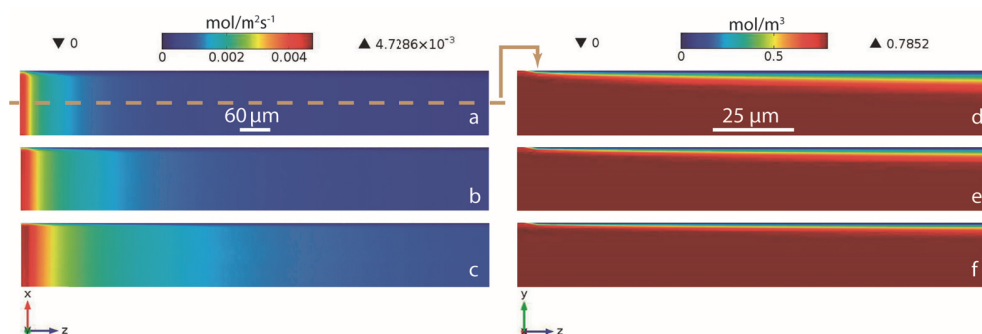


Figure 8.6. Mass flux maps over the initial electrode area for fuel/oxidant flow rates of (a) 4 ml h^{-1} , (b) 8 ml h^{-1} , and (c) 16 ml h^{-1} . The concentration boundary layers formed right beneath the electrode in a plane passing through its middle are provided for the same flow rates on the right (d to f).

Figure 8.7b also shows that a significant portion of reactants exit the device without participating in the reaction. This low fuel consumption per cycle is a shortcoming for all MFCs, but the advantage in our two-phase system is that the fuel recycling can be done in a practical way. In the single phase MFCs, the

area around the streams interface at the end of the channel contains both fuel and oxidant, making it difficult to separate them precisely and reintroduce them into the device. On the contrary, it can be seen from Figure 8.7b that this separation is actively done in the present device and, therefore, recycling in this device is possible.

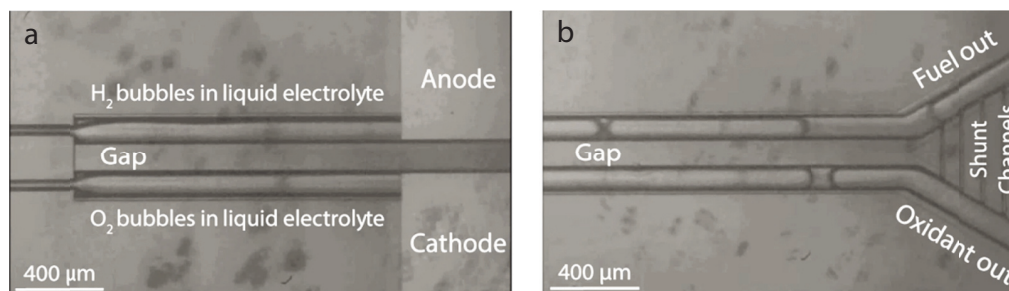


Figure 8.7. Top view of the device during operation under a total 16 ml h^{-1} gas flow (8 ml h^{-1} for each gas stream) and 1 ml h^{-1} of electrolyte flow: (a) beginning of the cell, and (b) end of the cell. Thermodynamically, the gases minimize their surface energy by being confined to the each of the channels above the electrodes and do not enter the shallow gap in between. The electrolyte fills in the gap and surrounds the gases, providing ionic conduction between the anode and cathode. Shunt channels in (b) provide pressure balance between the two outlet branches and prevent any potential bubble clogging.

The polarization and power density curves of the fuel cell are provided in Figure 8.8a and Figure 8.8b, respectively. Open circuit voltages are all close to 1 V , suggesting that the fuel crossover in all cases is similar and negligible. The results for the single phase case correlate well with values obtained elsewhere¹⁶. The current and power densities of the two-phase case are one order of magnitude higher than that for the single phase, suggesting that mass transport limitations have been alleviated by the introduction of controlled two-phase streams.

Figure 8.9 compares the peak power density and short circuit current density values for the two-phase and single phase cases at every tested flow rate. The experimental values are comparable with those obtained from the mass-transport model described in Section 8.3, indicating that mass-transport losses limit the performance of these fuel-cell devices.

Table 8.1 summarizes the average flux values, their ratios, and the ratio between the short circuit currents at each flow rate for both single phase and two-phase conditions. It can be seen that for higher flow rates, the simulation data overpredict the enhancement, suggesting that other limiting processes start to play a significant role.

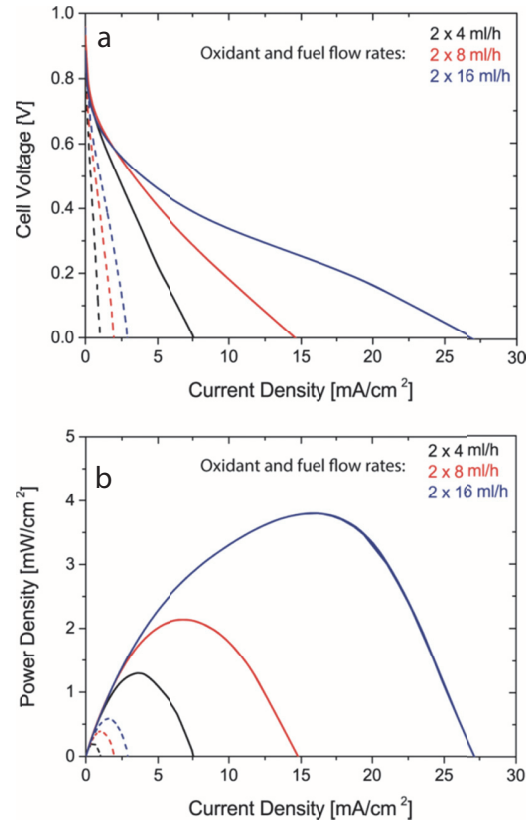


Figure 8.8. (a) Polarization and (b) power density profiles of all devices at three different flow rates. Solid lines and dashed lines correspond to the two-phase and single phase device respectively. Higher power densities are demonstrated for the two-phase device, suggesting an increased mass-transfer of gases to the electrodes. Expanded plots for the single phase devices are provided in SI.

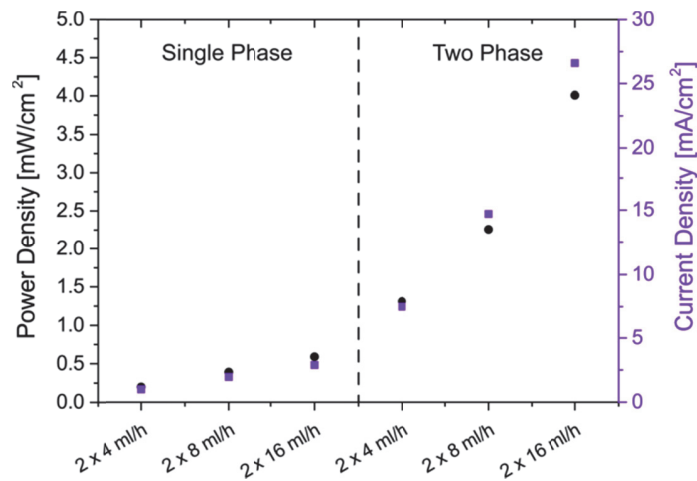


Figure 8.9. Comparison of peak power densities and short circuit currents at different flow rates under single and two-phase configurations.

Table 8.1. Average flux value ratios from modelling and comparison with short circuit current ratios from experiment

Flow rate [ml hr ⁻¹]	Two-phase			Single phase		Average flux ratios (modeling)	$\frac{J_{sc}^{2 \text{ phase}}}{J_{sc}^{1 \text{ phase}}}$ (experimental)
	d [μm]	Average flux [mol m ⁻² s ⁻¹]	J _{sc} [mA cm ⁻²] (Figure 8.9)	Average flux [mol m ⁻² s ⁻¹]	J _{sc} [mA cm ⁻²] (Figure 8.9)		
4	2.02	1.74x10 ⁻³	7.5	2.94x10 ⁻⁴	1	5.9	7.5
8	1.06	3.31x10 ⁻³	14.7	4.19x10 ⁻⁴	1.96	7.9	7.5
16	0.54	6.50x10 ⁻³	26.6	5.89x10 ⁻⁴	2.9	11	9.2

8.6 Conclusion

This study demonstrates that the mass transport limitations of single phase MFCs operating with hydrogen and oxygen saturated electrolytes can be relaxed by introducing H₂ and O₂ annular flows in electrolytes. By allowing gas streams to minimize their surface energy in confined microfluidic channels, we demonstrate that gas mixing can be prevented. The results show that the two-phase system delivers one order of magnitude better performance compared to its single phase counterpart. The method introduced here, opens up a pathway to revisit the utilization of gaseous hydrogen in high power density MFCs which was hindered by its low solubility in liquid electrolytes. Such a technique can be used in other electrochemical systems to boost their performance by relaxing potential mass transfer limitations. The power densities obtained in this work can be further improved by using micro/nanostructured electrodes. These electrodes induce mixing in the concentration boundary layer while providing higher active area for reactions to take place.

Bibliography

1. J. M. Andujar and F. Segura, *Renew Sust Energ Rev*, 2009, **13**, 2309-2322.
2. Powering the future, http://www.toyota-global.com/innovation/environmental_technology/fuelcell_vehicle/.
3. A. Simons and C. Bauer, *Appl Energ*, 2015, **157**, 884-896.
4. T. S. Zhao, *Micro fuel cells : principles and applications*, Academic Press, Amsterdam ; Boston, 2009.
5. J. D. Morse, *International Journal of Energy Research*, 2007, **31**, 576-602.
6. M. A. Modestino, D. Fernandez Rivas, S. M. H. Hashemi, J. G. E. Gardeniers and D. Psaltis, *Energy & Environmental Science*, 2016.
7. H. Ren, H. S. Lee and J. Chae, *Microfluid Nanofluid*, 2012, **13**, 353-381.
8. H. Y. Wang, A. Bernarda, C. Y. Huang, D. J. Lee and J. S. Chang, *Bioresource Technol*, 2011, **102**, 235-243.
9. D. S. Falcao, V. B. Oliveira, C. M. Rangel and A. M. F. R. Pinto, *Renew Sust Energ Rev*, 2014, **34**, 58-70.
10. M. A. Goulet and E. Kjeang, *J Power Sources*, 2014, **260**, 186-196.
11. E. Kjeang, N. Djilali and D. Sinton, *J Power Sources*, 2009, **186**, 353-369.
12. M. N. Nasharudin, S. K. Kamarudin, U. A. Hasran and M. S. Masdar, *International Journal of Hydrogen Energy*, 2014, **39**, 1039-1055.
13. S. A. M. Shaegh, N. T. Nguyen and S. H. Chan, *International Journal of Hydrogen Energy*, 2011, **36**, 5675-5694.
14. M. Safdar, J. Janis and S. Sanchez, *Lab Chip*, 2016, **16**, 2754-2758.
15. J. L. Cohen, D. J. Volpe, D. A. Westly, A. Pechenik and H. D. Abruna, *Langmuir*, 2005, **21**, 3544-3550.
16. J. L. Cohen, D. A. Westly, A. Pechenik and H. D. Abruna, *J Power Sources*, 2005, **139**, 96-105.
17. E. Kjeang, R. Michel, D. A. Harrington, N. Djilali and D. Sinton, *Journal of the American Chemical Society*, 2008, **130**, 4000-4006.
18. J. W. Lee, M. A. Goulet and E. Kjeang, *Lab Chip*, 2013, **13**, 2504-2507.
19. N. D. Mota, D. A. Finkelstein, J. D. Kirtland, C. A. Rodriguez, A. D. Stroock and H. D. Abruña, *Journal of the American Chemical Society*, 2012, **134**, 6076-6079.
20. P. Abbyad, R. Dangla, A. Alexandrou and C. N. Baroud, *Lab Chip*, 2011, **11**, 813-821.
21. E. Fradet, C. McDougall, P. Abbyad, R. Dangla, D. McGloin and C. N. Baroud, *Lab Chip*, 2011, **11**, 4228-4234.

22. M. Nagel, P. T. Brun and F. Gallaire, *Phys Fluids*, 2014, **26**.
23. R. Dangla, S. Lee and C. N. Baroud, *Phys Rev Lett*, 2011, **107**.
24. P. Gruner, B. Riechers, B. Semin, J. Lim, A. Johnston, K. Short and J. C. Baret, *Nat Commun*, 2016, **7**.
25. P. O. Lopez-Montesinos, N. Yossakda, A. Schmidt, F. R. Brushett, W. E. Pelton and P. J. A. Kenis, *J Power Sources*, 2011, **196**, 4638-4645.
26. M. J. Fuerstman, A. Lai, M. E. Thurlow, S. S. Shevkoplyas, H. A. Stone and G. M. Whitesides, *Lab Chip*, 2007, **7**, 1479-1489.
27. A. R. Abate, J. J. Agresti and D. A. Weitz, *Appl Phys Lett*, 2010, **96**.

Chapter 9

Conclusion and outlook

B*ased on the results presented in this dissertation, a strategy for thorough understanding of flow based electrochemical reactors is discussed. The potential macroeconomic impact of implementing such reactors is researched and other redox reactions that can benefit from this development are identified. Following to these discussions, recent efforts to answer the fundamental scientific questions together with the envisioned pathways for their scale up is presented.*

9.1 Introduction

Within the framework of this dissertation, several proof-of-concept devices in the field of electrochemical energy conversion have been realized. In design and implementation of all these devices, performance, design simplicity, and cost were key concerns. This study was in perfect timing with the efforts of materials and chemistry communities whose focus is on development of stable, inexpensive, and efficient components for these reactors. In this chapter, future research and development lines are discussed and some initial results are presented.

9.2 Multiphase Flow Electrochemical Reactors (MFERs):

Electrochemical processes account for a significant fraction of the electricity consumption in the world (i.e. more than 6% in the United States)^{1, 2}. Among them, water-based processes such as the chloro-alkali process accounts for approximately half of that energy requirement, and more than 55% of specialty chemicals require at least one of the products from this process – sodium hydroxide, chlorine or hydrogen. This industrial process requires very significant energy inputs which account for a predominant fraction of the cost of their products^{2, 3}. Furthermore, as the world moves towards the implementation of intermittent renewable generation sources, electrochemical energy conversion devices such as water electrolyzers are expected to be used as energy storage mechanisms⁴⁻⁸. Currently, the electrochemical production of hydrogen is not economically competitive with alternative production from fossil fuels: due to the high cost of the electricity input required⁹⁻¹¹. Figure 9.1 provides an estimate on the potential electrical power saving by moving from a membrane based reactor towards an MFER. In preparation of this figure, it is assumed that only the solid membrane is replaced by a liquid electrolyte with almost four times higher conductivity. Such an enhancement is achievable by moving from Nafion membranes to 1 M sulfuric acid. In this case, the reduction in power consumption for a given hydrogen generation rate is 20%. This implies more than one percent decrease in yearly electricity consumption of a country such as the US, i.e. 49 TWh². To put it into perspective, this amount exceeds the yearly production of 5 Leibstadt nuclear power plants in Switzerland. It must be noted that in this analysis, the fluidic losses and decrease in conductivity due to the presence of bubbles inside the electrolyte are not accounted for. These two sources of energy losses are important and the insights provided by future investigations will help to minimize them in order to achieve the maximum possible benefits from MFERs.

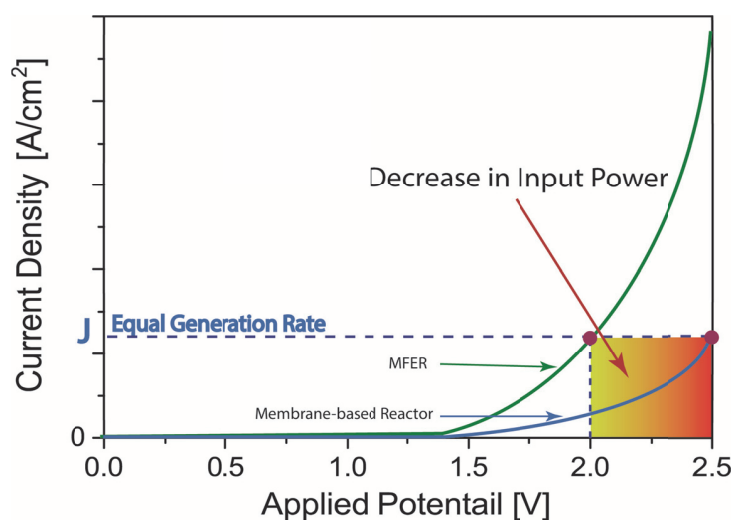


Figure 9.1. The power saving potentials of liquid electrolyte, flow based reactors versus solid electrolyte reactors. The curves are approximate and not based on real data.

Flow based electrochemical reactors reported in this dissertation are a class of devices that rely in flowing electrolytes to perform the ionic conduction and product/reactant separation tasks that are commonly carried by ion-conducting membranes. To facilitate their implementation, unveiling fundamental aspects of MFERs under practical operating conditions is necessary: high current densities ($>500 \text{ mA cm}^{-2}$), flow rates that provide control over the bubble trajectory (laminar flow regimes: $10 < \text{Re} < 100$), and optimized interelectrode distances for energy efficiency ($<500 \mu\text{m}$). Proceeding in this direction and with reference to Figure 9.3, understanding the fluid dynamics of multiphase flows to capture the impact of controlled quantities, such as cell geometry and fluidic properties on the monitored quantities, such as bubbles sizes and their equilibrium positions is crucial. This process is performed exploiting numerical simulations and experimental case studies in a complimentary way. In a second step, electrochemical measurements are performed to monitor quantities, such as species concentration gradients and bubble induced ionic resistances, when exposed to variations in electrochemical control quantities. In a parallel and interactive effort, governing laws of electrochemistry will be introduced into the multiphase flow solver of the first step, taking advantage of experimental data for verification. These interactions are illustrated in Figure 9.2. Finally, the built-up knowledge will represent the basis for the optimization of figures of merits in the right box of Figure 9.3.

The processes taking place inside an MFER can be divided into three categories which serve as thrusts for fulfillment of the research goals. These thrusts are depicted in Figure 9.4.

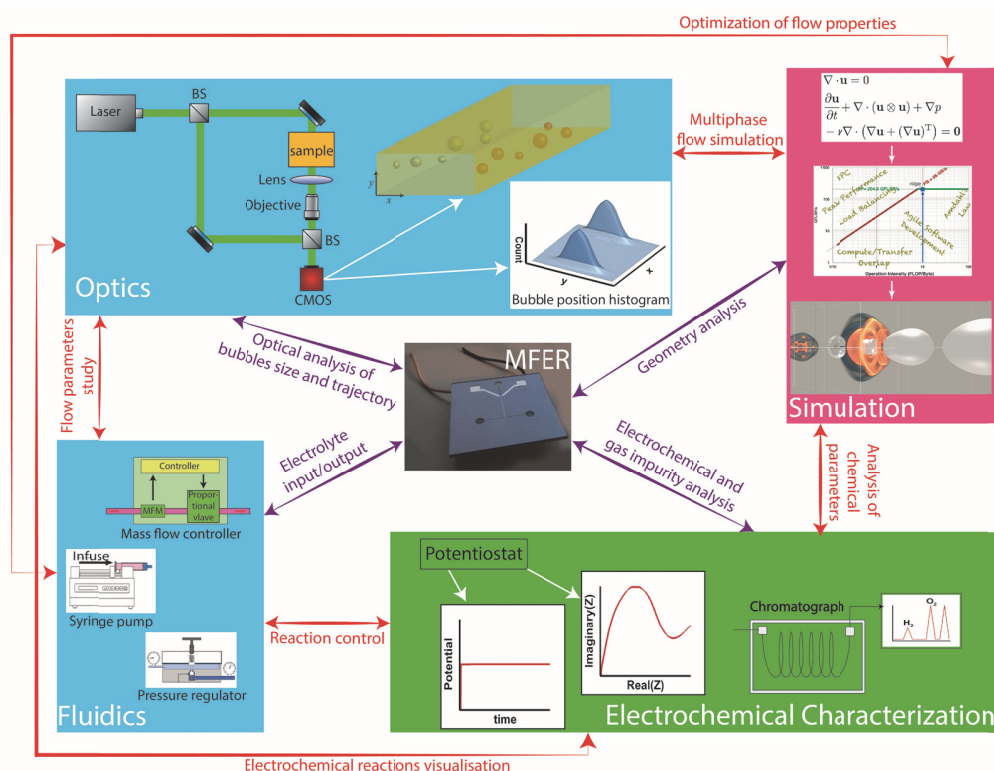


Figure 9.2. Schematic diagram of the multi-disciplinary interactions proposed in Section 9.2.

Controlled Quantities

- Cell Geometry:
 - Interelectrode Distance
 - Length
 - Height...
- Fluidic Properties:
 - Flowrate
 - Viscosities
 - Surface Tensions
 - Densities
- Electrochemical Parameters:
 - Current Density
 - Ionic Conductivity...

Monitored Quantities

- Bubble Sizes
- Equilibrium Positions
- Fluidic Pressure Drops
- Gas Volume Fraction
- Dissolution Percentage
- Concentration Gradients
- Bubble Induced Ionic Resistance...

Figures of Merit

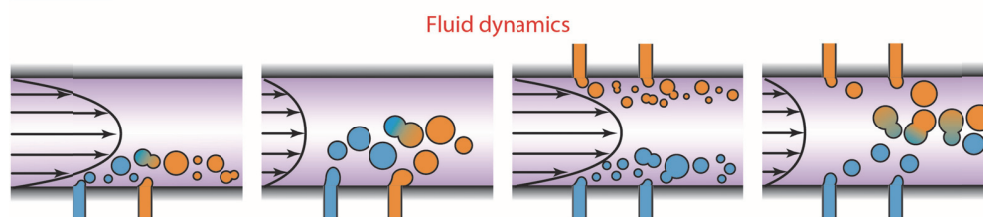
- Efficiency
- Products' Purity
- Throughput

Figure 9.3 The possible combinations of relevant quantities needed to fully understand the problem is excessively large, and is further complicated by the presence of multiple coupled parameters. A simulation package verified by a minimum number of experiments can save resources significantly when moving towards the design of efficient and scalable devices.

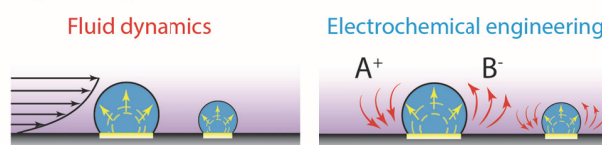
Thrust 1: Understand the dynamics of flowing bubbles in confined channel geometries.

In order to understand the bubble dynamics and their behavior under forces induced by laminar flow, the problem can be simplified by decoupling electrochemistry and physics of multiphase flow. In this scope, gas bubbles are inserted into the flowing electrolyte. Experimentally, they are injected from side channel(s) into the electrolyte flowing in the main channel (Figure 9.4). The bubbles can be introduced from single to multiple channels on one or both sides of the main channel to capture a complete range of possible scenarios: mono-sized bubbles injected from one side as the most primitive case to multi-sized bubbles from both sides as the most complex scenario. Numerically, the bubbles are initially placed according to the aforementioned scenarios into a periodic channel of the same geometry and advanced in time. Fluidic and cell geometry parameters in Figure 9.3 will be varied to observe their impact on relevant quantities of the middle box.

Thrust 1: Bubbles in flow



Thrust 2: Bubbles growing from electrodes



Thrust 3: Ultimate MFERs

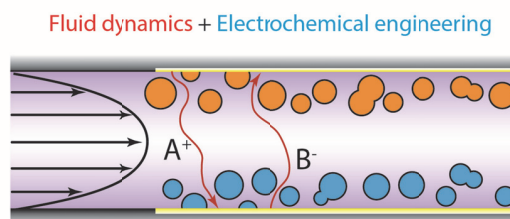


Figure 9.4. Schematic representation of proposed thrusts: The first thrust explores the physics of bubbly flows. Thrust 2 is expanded around the investigation of bubble growth on the surface of discrete electrode pair(s). Thrust 3 motivates the implementation of the knowledge gained in the previous thrusts for the development of the ultimate MFER.

Thrust 2: Understand the fluid dynamics and mass transport factors that drive the bubble growth and detachment processes at the surface of gas-evolving electrodes

The first step in multiphase electrochemical production processes involves the nucleation and growth of bubbles at the surface of electrodes. This step is critical for the performance of MFERs, as the residence time of bubbles pinned to the surface of catalytic sites dictates the diffusion induced crossover of gases. The growth rate, density, and distribution of nucleation sites affects ionic concentrations and, therefore, local current densities. Moreover, the percentage of the area of the electrode that is covered by the bubbles at steady state conditions defines the size of effective area which contributes to the overall reaction, affecting the overall cell overpotential. In order to better control the number of phenomena involved, growing bubbles at discrete points along the flow channels are considered. This helps to control the size range of produced bubbles and their interactions with each other in order to develop an understanding step by step and gradually increase the degrees of complexity. Important variables are electrochemical and fluidic parameters and quantities of interest include bubbles sizes, ionic concentrations, and gas dissolution percentage (Figure 9.3).

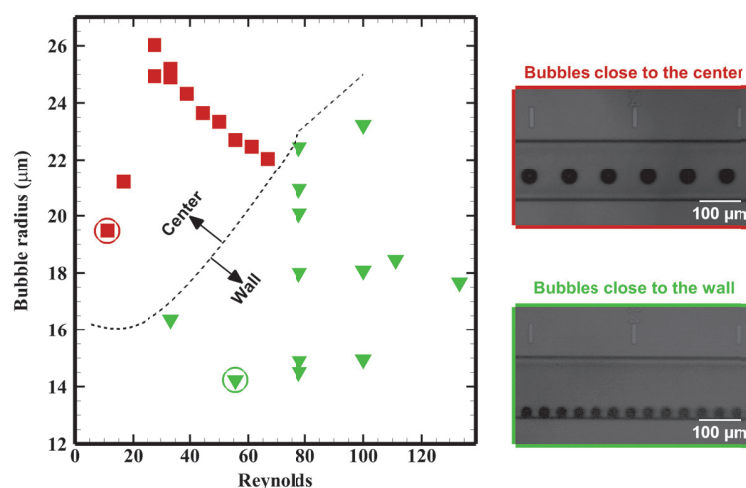


Figure 9.5. Bi-stable bubble position for different radius and Reynolds number: the micrographs on the right present experimental results obtained in LO, EPFL, and corresponds to the circled points in the graph on the left. Courtesy of Pooria Hadikhani.

Thrust 3: Characterize practical MFERs and moving towards their optimization

In practice, the reaction takes place on the entire surface of continuous electrodes lying along the MFER channels. The bubbles evolve at different sizes and interact with each other. They induce secondary flows and coalesce to form larger entities. Moreover, their volume fraction inside the electrolyte has an adverse effect on ionic conductivity of the electrolyte. In such a scenario, the invaluable insight and knowledge gained from the simplified systems discussed

above facilitate a complete understanding of the final device. This understanding can then be used to select the best possible combinations of controllable quantities in order to observe the most desirable sets of monitored quantities in Figure 9.3 and act as a basis for moving towards an ultimate MFER with the best possible figures of merit.

Thrust 1 is being pursued at EPFL by a new PhD student. Figure 9.5 reflects part of results obtained from his studies.

9.3 Alternative electrochemical reactions

Throughout this dissertation, water splitting has been used as a model system to evaluate performance of the reported devices. However, it must be noted that the functioning principles of these reactors can be also adopted for other electrochemical reactions. Two of these reactions are briefly described in the following subsections.

9.3.1 Chloralkali process

The chloralkali process is the industrial method of producing chlorine and sodium hydroxide by electrolysis of brine or NaCl solution. Similar to the water splitting reaction, this process involves two redox half reactions at the anode and cathode:

Anodic reaction: $2\text{Cl}^- \rightarrow \text{Cl}_2 + 2\text{e}^-$

Cathodic reaction: $2\text{H}_2\text{O} + 2\text{e}^- \rightarrow \text{H}_2 + 2\text{OH}^-$

An ion conductive membrane lying between the anode and cathode, allows for the sodium ions (Na^+) to pass through and combine with the hydroxide ions (OH^-) to produce caustic soda (NaOH). Therefore, the overall reaction takes the following form :



Hydrogen is also a byproduct of this reaction which can be valorized as a clean fuel if the brine electrolysis is performed with green electricity.

There are two main aspects of this reaction which makes it attractive for membrane-less concepts proposed in this study:

1) Unlike hydrogen which is mostly produced through steam reforming of natural gas on industrial scale, brine electrolysis is the main industrial method for production of chlorine. This makes it easier to introduce the membrane-less technology into the market.

2) Ion conductive membranes such as Nafion used in current state of the art chloralkali cells, work efficiently for very small cations such as proton. They impose a much larger overpotential to the cell for larger cations such as Na^+ in this reaction.

9.3.2 Carbon dioxide reduction

Electrochemical reduction of CO_2 to CO and hydrocarbon fuels such as methane is a recent topic of interest in electrochemistry society due to the environmental concerns of global warming. The current problems associated with this reaction which can be addressed at the device level are the mass transport limitation of carbon dioxide as a reactant and large operating cell potentials. A concept similar to the one for two-phase flow microfluidic fuel cell can be adopted to relax these problems.

9.4 Throughput enhancement

Although the devices presented in this study can be integrated into devices such as micro flame ionization detectors¹²⁻¹⁴ without strict scaling requirements, when it comes to microreactors, the most common criticism is their low throughput. This is even more crucial in the field of energy where the quantity of energy carrier is of prime importance. There are two ways of increasing the throughput when microfluidic technology is utilized: scaling out and scaling up¹⁵. These strategies have been discussed in Chapter 2 and here, the efforts to fabricate a larger membrane-less electrolysis cell is briefly discussed. One such a way is the areal scale up of electrodes as discussed in Chapter 7. The optimal implementation of this device is possible after shedding light on the working principles of MFERs presented in Section 9.2. A second scaled up device under development is a stagnant cell with gas diffusion electrodes containing biphilic structures¹⁶. It is worth noting that the electrochemistry community is undertaking alternative methods¹⁷⁻¹⁹ to further develop the membrane-less concept.

Bibliography

1. M. Grotheer, R. Alkire, R. Varjian, V. Srinivasan and J. Weidner, *Interface*, 2006, **15**, 52-54.
2. G. G. Botte, *The Electrochemical Society Interface*, 2014, **23**, 49-55.
3. S. Jenkins, *Chemical Engineering*, 2015, **122**, 32.
4. S. Chu and A. Majumdar, *Nature*, 2012, **488**, 294-303.
5. N. S. Lewis and D. G. Nocera, *Proceedings of the National Academy of Sciences*, 2006, **103**, 15729-15735.
6. T. A. Faunce, W. Lubitz, A. W. Rutherford, D. MacFarlane, G. F. Moore, P. Yang, D. G. Nocera, T. A. Moore, D. H. Gregory, S. Fukuzumi, K. B. Yoon, F. A. Armstrong, M. R. Wasielewski and S. Styring, *Energy & Environmental Science*, 2013, **6**, 695-698.
7. M. Paidar, V. Fateev and K. Bouzek, *Electrochimica Acta*, 2016, **209**, 737-756.
8. K. Zeng and D. Zhang, *Progress in Energy and Combustion Science*, 2010, **36**, 307-326.
9. J. Genovese, K. Harg, M. Paster and J. Turner, *Independent Review published for the US. Department of Energy Hydrogen Program, National Renewable Energy Laboratory, NREL/BK-6A1-46676*, 2009.
10. R. L. LeRoy, *International Journal of Hydrogen Energy*, 1983, **8**, 401-417.
11. K. E. Ayers, E. B. Anderson, C. Capuano, B. Carter, L. Dalton, G. Hanlon, J. Manco and M. Niedzwiecki, *ECS Transactions*, 2010, **33**, 3-15.
12. C. Lenz, H. Neubert, S. Ziesche, J. Förster, C. Koch, W. Kuipers, M. Deilmann and D. Jurkow, *Procedia Engineering*, 2016, **168**, 1378-1381.
13. W. J. Kuipers and J. Muller, *J Micromech Microeng*, 2008, **18**.
14. S. Zimmermann, P. Krippner, A. Vogel and J. Muller, *Sensor Actuat B-Chem*, 2002, **83**, 285-289.
15. K. S. Elvira, X. C. I. Solvas, R. C. R. Wootton and A. J. deMello, *Nature Chemistry*, 2013, **5**, 905-915.
16. A. Fazeli, M. Mortazavi and S. Moghaddam, *Appl Therm Eng*, 2015, **78**, 380-386.
17. J. Hartvigsen, J. Smith and F. Dogan, *Meeting Abstracts*, 2015, **MA2015-03**, 701.
18. G. D. O'Neil, C. D. Christian, D. E. Brown and D. V. Esposito, *Journal of the Electrochemical Society*, 2016, **163**, F3012-F3019.
19. M. I. Gillespie, F. van der Merwe and R. J. Kriel, *Journal of Power Sources*, 2015, **293**, 228-235.

Curriculum Vitae

S. Mohammad H. Hashemi

Rue de l'Industrie 9
1020 Renens, Switzerland
+41 789639538, smhhaashemi@gmail.com



EDUCATION

Ecole Polytechnique Fédérale de Lausanne (EPFL), Lausanne, Switzerland

PhD Candidate in Microtechnology: September 2012 – April 2017

University of Tehran, Tehran, Iran

M.Sc. Student in Mechanical Engineering, Minor in Energy Conversion, 2008 – 2011

University of Tehran, Tehran, Iran

B.Sc. Student in Mechanical Engineering, Graduated with Honors, 2004 – 2008

PROFESSIONAL EXPERIENCE

Doctoral Assistant (September 2012 - present)

Optics Laboratory (LO), EPFL, Lausanne, Switzerland

Lab Instructor (September 2011 - June 2012)

Heat Transfer and Thermodynamics Labs, University of Tehran, Tehran, Iran

R&D Engineer, (February to August 2011)

Niroo Research Center, Tehran, Iran

Internship Trainee (June to September 2008)

Mah Machine Company, Tehran, Iran

TECHNICAL SKILLS

- **Micro- and nanofabrication:** photolithography, e-beam lithography, soft lithography, and etching (DRIE, IBE, Wet Etching).
- **Thin film deposition:** PVD (sputtering, e-beam evaporation) and CVD (LPCVD, PECVD, UHVCVD).
- **Characterization:** SEM, fluorescence and wide field microscopy, spectroscopy, gas chromatography (GC).
- **Electrochemistry:** electrochemical design and characterization of electrolyzers, fuel cells, and photocatalytic reactors.
- **Metrology:** mechanical profilometry.
- **Packaging:** plasma, anodic and polymer adhesive bonding.

- **Software:** MATLAB, FORTRAN, C++, Solid Works, COMSOL, L-Edit, ANSYS FLUENT, Adobe Illustrator, Origin.

LANGUAGES

English: C2 Level of European Language Portfolio
 French: B1/B2 Level of European Language Portfolio
 Persian: Native
 Arabic: Intermediate

PUBLICATIONS

Journal Papers

- 1) Hashemi SMH, Neuenschwander M, Hadikhani P, Modestino MA, and Psaltis D, **Membrane-less micro fuel cell based on two-phase flow**, *Journal of Power Sources*, 2017.
- 2) Zielinski MS, Choi JW, La Grange T, Modestino M, Hashemi SMH, Pu Y, Birkhold S, Hubbell JA, Psaltis D, **Hollow Mesoporous Plasmonic Nanoshells for Enhanced Solar Vapor Generation**, *Nano letters*, 2016.
- 3) Modestino MA, Rivas DF, Hashemi SMH, Gardeniers JG, Psaltis D, **The potential for microfluidics in electrochemical energy systems**, *Energy & Environmental Science*, 2016.
- 4) Modestino MA, Hashemi SMH, Haussener S, **Mass transport aspects of electrochemical solar-hydrogen generation**, *Energy & Environmental Science*, 2016. “Invited Review”
- 5) Modestino MA, Dumortier M, Hashemi SMH, Haussener S, Moser C, Psaltis D, **Vapor-fed microfluidic hydrogen generator**, *Lab on a Chip*, 2015.
- 6) Hashemi SMH, Modestino MA, Psaltis D, **A membrane-less electrolyzer for hydrogen production across the pH scale**, *Energy & Environmental Science*, 2015. “Featured Cover Article, among 2015 top chemistry stories by Scientific American”
- 7) Choi JW, Hashemi SMH, Erickson D, Psaltis D, **A micropillar array for sample concentration via in-plane evaporation**, *Biomicrofluidics*, 2014.
- 8) Hashemi SMH, Choi JW, Psaltis D, **Solar thermal harvesting for enhanced photocatalytic reactions**, *Physical Chemistry Chemical Physics*, 2014.

- 9) Hashemi SMH, Fazeli SA, Zirakzadeh H, Ashjaee M, **Study of heat transfer enhancement in a nanofluid-cooled miniature heat sink**, *International Communications in Heat and Mass Transfer*, 2012.
- 10) Fazeli SA, Hashemi SMH, Zirakzadeh H, Ashjaee M, **Experimental and numerical investigation of heat transfer in a miniature heat sink utilizing silica nanofluid**, *Superlattices and Microstructures*, 2012.
- 11) Hashemi SMH, Fazeli SA, Shokouhmand H, **Fully developed non-Darcian forced convection slip-flow in a micro-annulus filled with a porous medium: analytical solution**, *Energy Conversion and Management*, 2011.

Conference Contributions

- 1) Zielinski MS, Choi JW, La Grange T, Modestino M, Hashemi SMH, Pu Y, Birkhold S, Hubbell JA, Psaltis D, **Efficient solar-vapor generation in hollow mesoporous plasmonic nanoshells**, CLEO-PR, OECC and PGC 2017, August 2017, Singapore.
- 2) Hashemi SMH, Neuenschwander M, Hadikhani P, Modestino MA, and Psaltis D, **Two-phase flow microfluidic fuel cell**, Flow17 Conference, July 2017, Paris, France.
- 3) Hashemi SMH, Neuenschwander M, Hadikhani P, Modestino MA, and Psaltis D, **Membrane-less microfluidic fuel cell with multiphase streams**, MicroTAS 2016, October 2016, Dublin, Ireland.
- 4) Modestino MA, Hashemi SMH, Psaltis D, **Splitting Water from Vapor Feeds: Towards Air-Based Solar-Hydrogen Generators**, 229th Electrochemical Society Meeting, May-June 2016, San Diego, CA, USA.
- 5) Hashemi SMH, Modestino MA, Psaltis D, **Towards High Efficiency Membrane-less Electrolysis**, MRS Spring Meeting, March-April 2016, Phoenix, AZ, USA.
- 6) Hashemi SMH, Modestino MA, Psaltis D, **Towards cost effective membrane-less electrolyzers**, ModVal13, March 2016, Lausanne, Switzerland.
- 7) Modestino MA, Hashemi SMH, Moser C, Psaltis D, **Next-generation microstructured water-splitting devices**, AIChE 2015 Meeting, November 2015, Salt Lake City, UT, USA.
- 8) Hashemi SMH, Modestino MA, Psaltis D, **Unconventional water splitting platforms**, 228th Electrochemical Society Meeting, October 2015, Phoenix, AZ, USA.
- 9) Hashemi SMH, Modestino MA, Psaltis D, **Novel Platforms for H₂ Generation**, 5th EFCF, Lucerne, Switzerland, July 2015

10) Hashemi SMH, Choi JW, Psaltis D, **Effect of Solar Thermal Energy on Photoreactions' Rate**, CLEO: Applications and Technology, June 2014, San Jose, California United States.

Patents

1) Hashemi SMH, Choi JW, Modestino MA, Psaltis D, **Membrane-less Electrolyzer**, PCT/IB2015/058050, Filed Oct. 19, 2015

2) Modestino MA, Hashemi SMH, Moser C, Psaltis D, **Device and System Having Water Microelectrolyzer Cells and Method of Using the Same**, US 15/082,357, Filed Mar. 28, 2016

AWARDS AND HONORS

- *Admitted to the best university of Iran through competitive nationwide entrance exam (Concours):* Ranked 276th among 396000 participants (2004)
- *FOE (Faculty of Engineering) Award:* Ranked 1st among 96 undergraduates studying in the School of Mechanical Engineering (2004 and 2008 academic years)
- *FOE (Faculty of Engineering) Award:* Ranked 3rd among 96 undergraduates studying in the School of Mechanical Engineering (2004 to 2008)
- *Awarded Scholarship of University of Tehran (Graduate Program):* Accepted without participating in the national entrance examination as an exceptional student (2008)

